Energietechnik

Sima Farazi

Numerical Modeling and Simulation of Oxy-Fuel Combustion Processes

SHAKER VERLAG

Numerical Modeling and Simulation of Oxy-Fuel Combustion Processes

Numerische Modellierung und Simulation von Oxy-Fuel Verbrennungsprozessen

Von der Fakultät für Maschinenwesen der Rheinisch-Westfälischen Technischen Hochschule Aachen zur Erlangung des akademischen Grades einer Doktorin der Ingenieurwissenschaften genehmigte Dissertation

vorgelegt von

Sima Farazi

Berichter: Univ.-Prof. Dr.-Ing. Heinz Günter Pitsch
Univ.-Prof. Dr.-Ing. Reinhold Kneer

Tag der mündlichen Prüfung: 16. September 2019

Berichte aus der Energietechnik

Sima Farazi

Numerical Modeling and Simulation of Oxy-Fuel Combustion Processes

Shaker Verlag
Düren 2019

Bibliographic information published by the Deutsche Nationalbibliothek
The Deutsche Nationalbibliothek lists this publication in the Deutsche Nationalbibliografie; detailed bibliographic data are available in the Internet at http://dnb.d-nb.de.

Zugl.: D 82 (Diss. RWTH Aachen University, 2019)

Printed in Germany.

ISBN 978-3-8440-7032-3
ISSN 0945-0726

Shaker Verlag GmbH • Am Langen Graben 15a • 52353 Düren
Phone: 0049/2421/99011-0 • Telefax: 0049/2421/99011-9
Internet: www.shaker.de • e-mail: info@shaker.de

Acknowledgments

This work would have not been possible without the encouragement, assistance, and help of several people. I would like to express my sincere appreciations to all of them.

I would like to express special appreciation to **Prof. Heinz Pitsch** for giving me the opportunity to work on this subject. I am very thankful for his support, advices, and supervision during my work at the Institute for Combustion Technology (ITV). I am very thankful to **Prof. Herbert Olivier** for heading my Ph.D committee and **Prof. Reinhold Kneer** for being second referee in the committee and for all his kind advices and support regarding my thesis. I kindly acknowledge the financial support from Deutsche Forschungsgemeinschaft (DFG) through SFB/TRR 129 project. I would like to thank all my wonderful project partners in the SFB/TRR 129.

In ITV, I got the chance to get to know many nice colleagues. I would like to thank them all for being wonderful colleague to me and I will remember them all with fondness. I would like to appreciate the support and guidance of **Dr. Antonio Attili**, which substantially accelerated my research through his valuable experiences and useful discussions. I am also very thankful to **Prof. Seongwon Kang** and **Tobias Falkenstein** for their generous help and comments regarding application and development of our in-house code. I had the best office mates; **Jörn Hinrich**, **Marco Davidovic**, and **Fabian Fröde**, I thank them all for being very supportive, generous to share knowledge, and always available to discuss any specific topic. I would also like to thank **Mathis Bode** for his kind support regarding IT issues and ITV computing cluster. I am very thankful to **Sonja Huppertz** and **Eva Schieren** for their help and support in all administrative issues. My special thanks go to **Dr. Agnes Jöcher**, **Martina Baroncelli**, and **Rupali Tripathi** not only for being very supportive colleague but also for the wonderful friendship.

I particularly thank **Dr. Amin Kiani**, **Dr. Mohammad Rahimi**, and **Davood Baratian** for being wonderful friends to me and for the pleasant time in our hiking and adventure trips. My heartily appreciations go to **Amin** for his love, support, and encouragements.

This dissertation is dedicated to my beloved parents **Soheila Ehteshami pour** and **Esmaeel Farazi** who taught me the most important lessons.

Abstract

Coal ignition and combustion under conventional and oxy-fuel conditions are numerically investigated to understand the interactions between chemical and transport processes and to support model development.

Char burnout of coal particles is studied in highly resolved numerical simulations including a detailed description of the particle surface and the gas phase chemistry. At the solid-gas interface, heat and mass fluxes due to surface reactions involving carbon oxidation and gasification are considered. The model is validated with experimental results for char burnout in a flat flame burner. A comprehensive set of fully resolved reactive 2-D simulations has been performed by varying particle size, relative velocity, diluent, and oxygen composition in the surrounding gas. The simulation results are discussed regarding the CO_2 and N_2 content of the atmosphere highlighting the effects of oxy-fuel combustion. Increasing particle Reynolds number reduces gas temperature and results in a faster oxygen supply, which consequently yields a higher particle burning rate up to the point where the resulting temperature reduction leads to a lower burning rate. Combustion reduces the drag force of the reacting particle and thus a modified drag coefficient as a function of the dimensionless Stefan flow velocity is provided.

In addition, ignition of coal particles is studied by using a fully coupled Euler-Lagrange approach. Devolatilization of coal particles is modeled with the chemical percolation devolatilization (CPD) method coupled with a detailed gas chemistry. Numerical simulations showed that an increase of ignition delay time in oxy-atmosphere compared to the air case is related to the depletion of radicals that react with the abundant CO_2 of the oxy-atmosphere. Considering different particle streams showed that an increase in particle number density delays the onset of ignition and forms a more continuous and narrower flame front. Particle heating and ignition induce velocity variations in the gas phase. In the denser stream, velocity variations become significant and compromise the validity of a constant velocity assumption that is usually made in computing ignition delay time from the observed ignition location. It is also found that high particle slip velocities lead to a locally low volatile concentration and low temperature, which consequently increase ignition delay time.

Zusammenfassung

In dieser Arbeit werden die Zünd- und Verbrennungsprozesse von Kohlenstaub unter konventionellen und Oxyfuel-Bedingungen numerisch untersucht, um die Wechselwirkungen zwischen chemischen Reaktionen und Transportprozessen zu verstehen und damit die Modellentwicklung zu unterstützen.

Die Verbrennung einzelner Kohlepartikel wird in hochauflösenden numerischen Simulationen abgebildet, welche eine detaillierte Beschreibung der Partikeloberflächen und der Gasphasenchemie beinhalten. Das Modell wird mit experimentellen Ergebnissen für den Kohleausbrand in einem Flachflammenbrenner validiert. Ein umfassender Satz von vollständig aufgelösten reaktiven 2-D Simulationen wurde durch die Variation der Partikelgröße, der Relativgeschwindigkeit, des Verdünnungsmittels und der Sauerstoffzusammensetzung im umgebenden Gas durchgeführt. Die Simulationsergebnisse werden im Hinblick auf den CO_2- und N_2-Gehalt der Atmosphäre diskutiert. Eine zunehmende Partikel-Reynoldszahl reduziert die Gastemperatur und führt zu einer schnelleren Sauerstoffbereitstellung, woraus anfänglich eine höhere Partikelverbrennungsrate resultiert. An dem Punkt, an dem der Temperatursenkungseffekt überwiegt, nimmt die Partikelverbrennungsrate wieder ab. Es wird auch festgestellt, dass die Verbrennung die Widerstandskraft des reagierenden Teilchens reduziert. Ein modifizierter Widerstandsbeiwert wird in Abhängigkeit von der Stefan-Strömungsgeschwindigkeit bereitgestellt.

Darüber hinaus wird die Zündung von Kohlepartikeln mit einem vollständig gekoppelten Euler-Lagrange-Ansatz untersucht. Die Gasifizierung der Kohlepartikel wird mit der Chemical Percolation Devolatilization Methode (CPD) in Verbindung mit detaillierter Gasphasenchemie modelliert. Numerische Simulationen zeigten, dass eine in der Oxy-Atmosphäre vorliegende Verlängerung der Zündverzugszeit mit einem Verbrauch von Radikalen zusammenhängt. Der Verbrauch von Radikalen ist auf Reaktionen der Radikale mit dem CO_2 der Oxy-Atmosphäre zurückzuführen. Die Betrachtung verschiedener Partikelströme zeigt, dass eine zunehmende Partikelanzahldichte den Zündbeginn verzögert und eine kontinuierlichere und schmalere Flammenfront bildet. Es wird auch festgestellt, dass hohe Partikelschlupfgeschwindigkeiten zu einer lokal niedrigen Konzentration der Devolatisierungsprodukte und niedrigen Temperatur führen und somit die Zündverzugszeit erhöhen.

Publications

Peer reviewed papers

Farazi, S., Hinrichs, J., Davidovic, M., Falkenstein, T., Bode, M., Kang, S., Attili, A., Pitsch, H., Numerical investigation of coal particle stream ignition in oxy-atmosphere, Fuel 241 (2019) 477-487.

Farazi, S., Attili, A., Kang, S., Pitsch, H., Numerical study of coal particle ignition in air and oxy-atmosphere, Accepted, Proceedings of the Combustion Institute 37 (2019) 2867-2874.

Farazi, S., Sadr, M., Kang, S., Schiemann, M., Vorobiev, N., Scherer, V., Pitsch, H., Resolved simulation of single char particle combustion in a laminar flow field, Fuel 201 (2017) 15-28.

Farazi, S., Sayadi, T., Pitsch, H., Numerical analysis of the drag force acting on the reactive single char particle under oxy-fuel condition, Proceedings of the China National Symposium on Combustion (2016).

Sayadi, T., **Farazi, S.**, Kang, S., Pitsch, H., Transient multiple particle simulations of char particle combustion, Fuel 199 (2017) 289-298.

Oral presentations

Farazi, S., Attili, A., Heuer, S., Schiemann, M., Scherer, V., Pitsch, H., Modeling and simulation of porosity in coal combustion under oxy-fuel condition, 2nd International workshop on oxy-fuel combustion (Germany 2018).

Farazi, S., Schiemann, M., Vorobiev, N., Scherer, V., Kang, S., Pitsch, H., A new variable transport coefficient single-film model for char combustion, 8th European Combustion Meeting (Croatia 2017).

Farazi, S., Pitsch, H., Fully resolved simulation of single and group particle combustion in an oxy-fuel atmosphere, 1st International workshop on oxy-fuel combustion (Germany 2016).

Contents

1 Introduction

Increasing carbon dioxide (CO_2) emissions in the atmosphere and its relation to global warming have become a great concern for the future of life on earth. Fossil-fuel-fired power plants, especially those burning coal, are among the main CO_2 emitters. Although the use of renewable energy sources is continuously growing, in the foreseeable future, fossil fuels are still the major energy source due to their abundance and low price. Among fossil fuels, coal is one of the cheapest and the most available fuel. To reduce CO_2 emissions from coal fired power plants, carbon capture and storage (CCS) techniques can be applied. Oxy-fuel combustion is one of the most promising approaches for CCS to sequestrate and reduce CO_2 emissions from coal combustion.

In oxy-fuel combustion, coal burns with oxygen instead of air. The CO_2 can then be captured in purer form from the flue gas. To achieve reasonable combustion temperatures, the CO_2 is typically partially recirculated and mixed with the combustion oxygen. Oxy-fired furnaces, therefore, operate in a CO_2 environment, which has different properties than the more conventional N_2 environment [1]. Table 1.1 compares some of gas properties of N_2 and CO_2. A higher proportion of carbon dioxide than nitrogen in the oxidizer gas leads to different thermal properties, heat transfer, and therefore, combustion in other temperature ranges. In addition, due to the reactivity of the CO_2, the surface reactions of the coal particles in the oxy-fuel atmosphere can become significantly different from conventional coal combustion. As a result, designing an optimized coal fired furnace under oxy-fuel condition requires further investigation and the understanding of the underlying physical processes. A

Property	N_2	CO_2	Ratio CO_2/N_2
Thermal conductivity [10^{-3} W/(m K)]	74.67	81.69	1.09
Molar heat capacity [kJ/(kmol K)]	33.6	56.1	1.67
Density [kg/m^3]	0.29	0.45	1.55
Oxygen diffusion [10^{-4} m^2/s]	3.07	2.37	0.77
Molecular weight [kg/kmol]	28	44	1.57

Table 1.1: Gas properties for N_2 and CO_2 at 1173 K [1].

comprehensive review of several experimental and numerical studies that have been made to investigate oxy-fuel combustion of pulverized coal can be found in Chen et al. [2]. In developing oxy-fuel technology, computational modeling of coal combustion under oxy-fuel condition is indispensable and becomes the main focus of the current study.

Modeling of coal combustion is challenging due to the multi-phase and the multi-scale nature of the problem. Figure 1.1 schematically shows the relevant scales in a coal fired burner. While an industrialized coal burner has dimensions of a few meters, it contains millions of the pulverized coal particles with diameters in the range of a few micrometers. Besides being multi-phase and multi-scale, coal combustion happens through complex processes such as devolatilization and char burnout. Coal particles undergo devolatilization when heat transfer from the hot gas phase causes thermal decomposition and results in the release of volatile gases from particles to the surrounding gas phase. The released volatile gases diffuse into the surrounding gas phase,

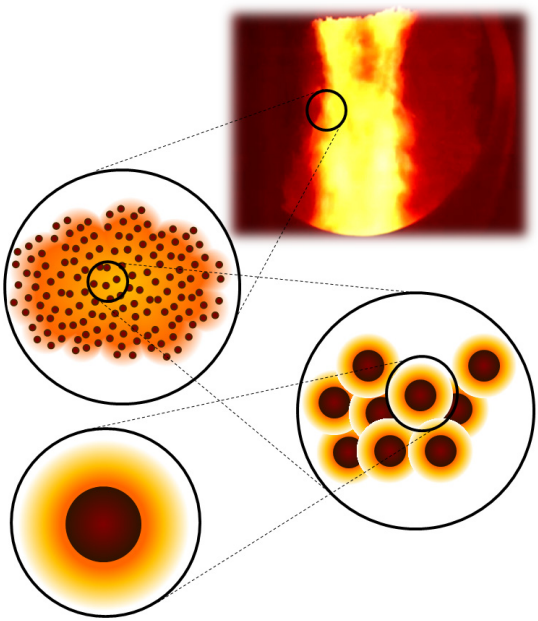

Figure 1.1: Schematic view of relevant scales in the coal combustion.

undergo homogeneous reactions, and form a volatile flame. At the end of the devolatilization phase, when the volatile flame extinguishes, oxygen can access the particle surface and char burnout begins. Char refers to the remained matter from coal particle after devolatilization, and it mainly contains carbon. Char burnout involves heterogenous reactions at the surface of the particles. Both devolatilization and char burnout processes involve mass, momentum, and energy transfer between particles and the surrounding gas. So far, there were many theoretical and numerical works on the individual phenomena of the coal combustion. However, complex interactions between individual phenomena, such as interactions between particle dynamics and combustion, which are very important for predictive simulations have not been investigated in detail and therefore, become the main objective of the current study.

Mass, momentum, and energy transfers between a coal particle and its surrounding gas can be either particle-resolved or modeled by an Euler-Lagrange approach as shown schematically in Fig. 1.2. In the particle-resolved approach, the particle-gas interface and the boundary layer are chemically and spatially resolved. The particle-resolved approach requires computational cells with a size Δx much smaller than the particle diameter D_p. In the Euler-Lagrange approach, particles are tracked as Lagrangian points and the exchange of the mass, momentum, and energy between the gas phase and particles correspond to source terms in the conservation equations. The Euler-Lagrange models are typically used for practical applications on the large scale. In the Euler-Lagrange approach, computational cells are allowed to be much bigger than the particle diameter. In the current study, the particle-resolved approach is employed to investigate char burnout in the second chapter, while devolatilization and ignition of coal particles are modeled applying the Euler-Lagrange approach in the third chapter. The results in the second chapter

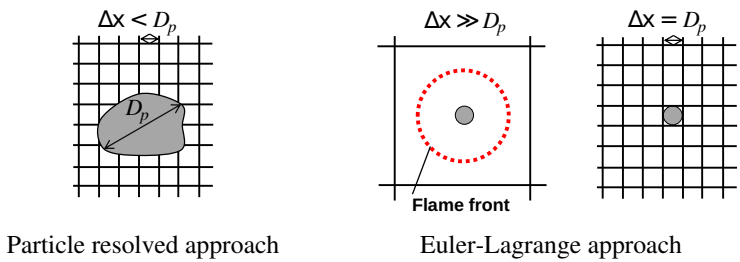

Figure 1.2: Schematics of the particle-resolved and Euler-Lagrange approaches.

of the current thesis have been published by Farazi et al. [3] and Farazi et al. [4], while the results in the third chapter of the current thesis have been published by Farazi et al. [5] and Farazi et al. [6].

In the second chapter, results from numerical simulations are discussed that were performed to investigate combustion of char particles considering both air and oxy-fuel atmospheres. Char possesses a porous structure and its main compound is carbon. Resolved simulations of char particle combustion have been used to understand the interaction of chemical and transport processes and develop accurate models for application in large scale simulations using the point particle assumption. Several resolved simulations of char particle combustion have been described in the literature.

Maffei et al. [7] studied coal particle temperature and burnout time during combustion in air and oxy-fuel atmospheres by performing experiments and numerical simulation. Hecht et al. [8, 9] simulated quiescent char combustion in N_2 and CO_2 diluents using a 1-D steady state model in SKIPPY (Surface Kinetics in Porous Particles). SKIPPY solves mass, momentum, and energy conservation for a reacting porous spherical particle and its reactive boundary layer. They studied the impact of CO_2 and steam gasification reactions on coal char combustion under oxy-fuel condition varying the O_2 concentration. Applying the same model, Shaddix et al. [10] performed numerical assessment of the CO_2/CO production ratio correlation presented by Tognotti [11]. Furthermore, Hecht et al. [12] quantified errors associated with the two simplified common coal char combustion sub-models: the single film model originally proposed by Nusselt [13] and the double film model proposed by Burke and Schumann [14]. Their study was based on the 1-D steady state model, and thus, did not capture the char combustion history or interactions between flow and chemistry. Kestel et al. [15] and Richter et al. [16] performed steady 2-D simulations of char particle combustion in the flow of air and oxy-atmosphere, respectively. Richter et al. [16] compared 2-D simulations of spherical 200 μm particles to measurements carried out by Bejarano and Levendis [17]. They have investigated the influence of the relative Reynolds number, Re_{rel} of the char particle on its combustion behavior and observed that increasing Re_{rel} leads to higher carbon consumption rates. Although their model resolved the particle boundary layer spatially, chemistry was described based on a global mechanism. Furthermore, due to the steady state assumption in their model, the evolution of char combustion was not considered. Cho et al. [18] have successfully applied a 1-D model to study the evolution of liquid droplets and carbon particle combustion. Based on this transient-resolved model, further

investigations on char combustion characteristics have been performed in Lee et al. [19, 20]. Furthermore, Lee et al. [21] extended this transient-resolved model to a 2-D simulation and showed that finite Damköhler number effects can only be evident when detailed transport and chemical kinetics are included. Their study included char oxidation only in air atmosphere. In the current study, a method similar to that of Lee et al. [21] is applied.

The applied method is validated by the temperature-diameter measurements in the flat flame burner. Temperature-diameter measurements have a significant advantage in particle combustion model development. There are at least two different applications of the measured data. First, rate law parameters for heterogeneous char consumption can be derived. This has been done for oxy-fuel char combustion using reaction rate models with varying complexity, e.g. in [22–24]. Second, such experimental data are useful for validation of the modeling results [7, 23, 25–28]. Direct measurements of particle properties (temperature, diameter, and even shape) have been subject of several studies in the past. These studies were carried out in laminar flow reactors, which provide well defined combustion atmospheres, representing air or oxy-fuel conditions. The gas phase temperature in these systems is provided from a gas flame, based on non-premixed (Hencken type, [22–24, 29–35]) or premixed (McKenna type, [30, 36–38]) combustion, or heated reactor walls [7, 17, 39–43]. For temperature measurements, different approaches were used, non-imaging techniques based on photomultipliers [7, 17, 22, 29–31, 33, 34, 39–43] as well as imaging techniques [23, 24, 30, 32, 38]. The non-imaging techniques (based on photomultipliers) derive (equivalent spherical) particle diameter from intensities in different wavelength ranges [22, 29–31, 33, 34, 42, 43] or preselected from previous sieve classifications of particle sizes [7, 17, 39–43]. The imaging techniques derive particle diameter and additional 2-D projections [30] or 3-D [44, 45] shape of burning char particles from the particle extension in the image simultaneous to the temperature measurement.

Besides comparing air and oxy-atmosphere, the particle-resolved simulations were applied to study the effect of the flow field on the particle combustion. Therefore, particle-resolved simulations were performed at different particle Reynolds numbers to investigate the effect of the flow dynamics on the temperature, oxygen concentration, and burning rate. In addition, particle-resolved simulations were applied to investigate the combustion effect on the flow dynamics. Differently from a non-reactive particle, the drag force on a reactive particle depends on the Stefan flow caused by chemical reactions. Therefore, two-dimensional particle-resolved simulations were carried out for

both reactive and non-reactive char particles. The analysis of the simulation results provides an updated drag model that considers the effect of char oxidation.

In the third chapter, simulations using an Euler-Lagrange approach are presented that were performed to study coal devolatilization and ignition for both single and group particle configurations. The ignition process of coal particles significantly affects the flame stabilization and burner performance under both air and oxy-atmosphere. The volatile flame evolution is computed applying the chemical percolation devolatilization (CPD) model [46], coupled with the finite rate chemistry for gas phase reactions. The numerical model is validated against experimentally measured ignition delay time of coal particle in the laminar entrained flow reactor [47].

It has been shown that the application of the CPD model reveals a double peak in the time evolution of the release rate of volatile mass, mostly due to the dynamics of tar [48, 49]. A double peak profile has also been observed experimentally in the time evolution of species and temperature measurements around burning coal [50–52]. The link between the double peak in the devolatilization rate produced by the CPD model and the double peak in the species measurement has not yet been investigated in detail. The appearance of the double peak in the mass release from coal manifests two phases in the devolatilization process. In the current study, the effects of the presence of these two phases in the devolatilization process on the dynamics of ignition for different particle sizes, gas temperature, and composition are investigated. The differences of these mechanisms in air and oxy-atmosphere are also assessed.

Switching from air to oxy-fuel combustion can have significant effects on the ignition and combustion dynamics, due to the different chemical and thermal properties of N_2 and CO_2. Several experimental [7, 17, 47, 53–56] and numerical [57–60] studies indicate that replacing N_2 by CO_2 increases ignition delay time and duration of devolatilization. Recently, Jimenez and Gonzalo-Tirado [60] simulated coal particle devolatilization in air and oxy-atmospheres. They explained the longer devolatilization period by the lower peak temperatures observed in the oxy-atmosphere case, which resulted from the combined effect of the chemical properties and the higher heat capacity of CO_2. However, the primary effect of CO_2 on retarding the onset of ignition remains unclear and has been a matter of debate. In the present work, numerical simulations of coal particle ignition are performed using detailed sub-models for the devolatilization process and the chemical reactions in the

gas phase. Single particle ignition is computed both in air and oxy-atmosphere at various particle sizes and ambient temperatures. The results in air and oxy-atmosphere are compared and the mechanisms responsible for the increased ignition delay in oxy-atmosphere are investigated and assessed.

In addition to the properties of the coal particle and the gas phase, the interactions between particles can significantly affect ignition and flame structure inside a real furnace. Ignition delays and flame structure in particle group configurations have been the subject of many experimental [37, 47, 61–69] and numerical [59, 70–87] studies, where the latter considered both clouds/arrays of suspended particles [70–75] and streams of moving particles [76–87].

Du et al. [71] modeled combustion of a cylindrical cloud of coal particles suspended in a hot furnace. They found that at high furnace temperatures, $1000 - 1350$ K, the dense coal stream is ignited by volatile ignition (homogeneous ignition), while the dilute coal stream undergoes carbon ignition (heterogeneous ignition). At a furnace temperature of 1100 K, they showed that by increasing particle number density (particle diameter of 64 μm) from 1 to 10×10^9 particles/m^3, the ignition delay time first decreases until it reaches a minimum and then increases. The number density of the minimum ignition delay time is usually referred to as the critical particle group number. This trend qualitatively agrees with the results from coal stream experiments performed by Ruiz et al. [88]. In oxy-atmosphere, a similar trend for the ignition delay time with respect to particle number density was observed by Liu et al. [47]. They measured coal stream ignition in a laminar entrained flow reactor and performed a parametric study of coal combustion in both air and oxy-atmosphere by varying coal type, temperature of the coflow ($1200 - 1670$ K), particle diameter ($54 - 125$ μm), O_2 concentration in the coflow ($12 - 20$ vol%), and coal feeding rates ($0.005 - 1$ g/min). Annamalai and Ramalingam [70] computed the critical group number for a spherical cloud of char particles and indicated that the group number in char combustion is higher than the corresponding one in a droplet cloud. Wang et al. [72] and Zhao et al. [73] simulated ignition and combustion of a spherical cloud of coal particles surrounded by a hot gaseous mixture. They showed the existence of two flame structures after ignition; the inner premixed flame moving towards the coal cloud center and the outer diffusion flame moving away from the cloud. Qiao [74] computed the flame propagation process and flame-speed oscillation in a spherical cloud of moving char particles surrounded by air atmosphere. In his model, ignition is initiated with an imposed hot spot in the cloud. He observed a more significant slip velocity between particles and

gas phase especially in the early flame propagation. Kiga et al. [63] measured the flame propagation speed of a pulverized coal cloud in a microgravity combustion chamber. They observed markedly lower flame propagation speed in O_2/CO_2 compared with O_2/N_2. Tufano et al. [75] computed combustion of particle arrays varying particle spacing. In their model, particles are fixed in a laminar flow, and the interface between each particle and the gas phase is spatially resolved. Depending on the distance between particles, they observed different combustion regimes. Bai et al. [87] numerically studied a turbulent coal jet flame in air atmosphere applying a two step chemistry model. They identified three coal flame structures named interspersed, stripe, and stable continuous flame. Rieth et al. [82] performed direct numerical simulation of a three-dimensional turbulent mixing layer, between an air stream seeded by coal particles and a stream of hot lean combustion products. They showed that the initial ignition occurs at very lean conditions around particles entrained in the hot gas region. They observed both non-premixed and premixed modes during volatile combustion and identified two distinguished flames, one burning into the carrier air and the other one propagating towards hot lean products.

In the aforementioned numerical/experimental studies, ignition delay time is influenced by the combined effect of particle/particle interactions in the cloud together with the mixing between the particle cloud and the surrounding coflow gas. In the current study, the effect of mixing with the surrounding ambient gas is eliminated. Extending the study of the single particle ignition, in the particle group configuration, particles are introduced with a single hot stream and without coflow to assess the impact of particle/particle interactions on the coal particle ignition and combustion under oxy-atmosphere condition.

2 Char particle combustion with a particle resolved approach

In this chapter, particle resolved simulations of the char combustion in both air and oxy-atmospheres are presented and discussed. Simulation methods including the governing equations and the numerical approaches are described. Simulation results for both atmospheres are validated with the experimental measurements of the char burnout in the flat flame burner. The reasons behind the different char combustion behavior in air and oxy-atmosphere are discussed. The relative Reynolds number Re_{rel} is varied in the expected Re_{rel} interval for pulverized char particles in a swirl burner. Differences between cases with the same Re_{rel}, but various particle sizes and relative velocities are analyzed. The same set of simulations was performed for various oxygen concentrations (24%, 30%, and 36%). These simulations determine the influence of the gas flow on the rate of the carbon consumption and the heat release. In addition, the influence of the particle combustion on the flow dynamics are discussed and an updated drag model considering the Stefan velocity effect on the drag coefficient in terms of a correlation function is presented.

2.1 Models and numerical methods

In the current study, combustion of a single particle in a laminar flow reactor is investigated. Figure 2.1 shows a schematic view of the single particle located at 60 mm height of the burner. Combustion of the particle with diameter D_p is computed in a rectangular numerical domain, $[x_1^-, x_1^+] \times [x_2^-, x_2^+] = [-50D_p, 100D_p] \times [-50D_p, 50D_p]$ (see Fig. 2.1). The computational domain origin is set to the center of the particle. The computational domain was chosen large enough so that the particle combustion is not influenced by the domain boundaries. The particle is assumed to have fixed diameter and location. A mixture of gaseous species with a relative velocity with respect to the particle, U_1^0, enters the domain through the inlet at x_1^- and leaves the domain at x_1^+. To model solid particle combustion with surrounding gas flow, the conservation equations were solved in the solution domain consisting of gas, solid, and the interface between them.

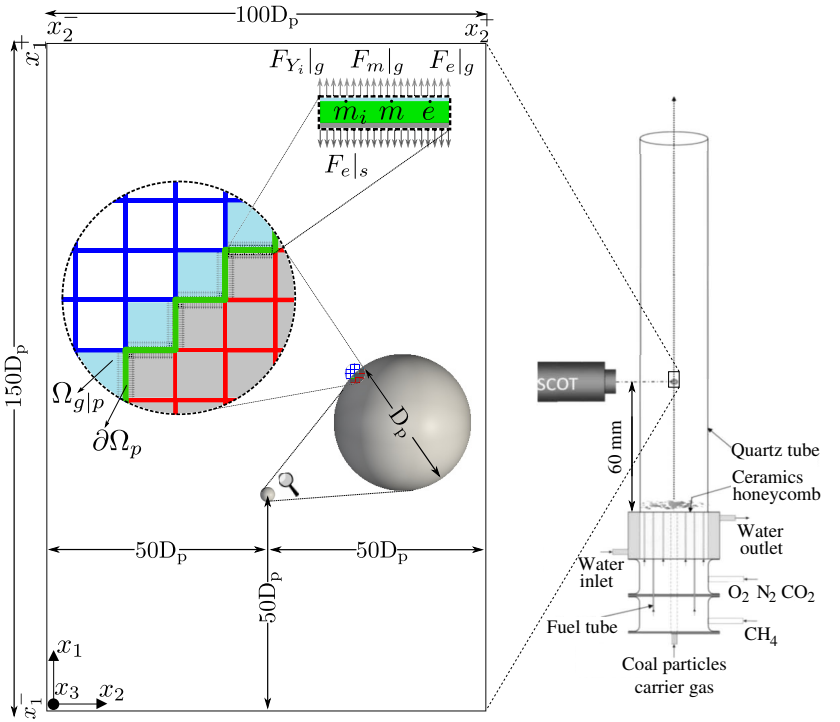

Figure 2.1: Magnified view of a particle with diameter D_p and computational domain located in a laminar flow reactor [23]. A part of the computational grid (in blue color for gas and in red for solid phase) is magnified schematically, to demonstrate the solid-gas interface (in green color) and the corresponding fluxes and source terms of species, mass, and energy.

2.1.1 Gas phase

Conservation of mass, species, momentum, and energy in the gas phase within the low-Mach formulation leads to the governing equations as [89]

$$\frac{\partial \rho_g}{\partial t} + \frac{\partial}{\partial x_\beta}(\rho_g U_\beta) = 0\,, \tag{2.1}$$

$$\frac{\partial \rho_g Y_i}{\partial t} + \frac{\partial}{\partial x_\beta}(\rho_g (U_\beta + V_{\beta,i}) Y_i) = \dot{M}_i\,, \tag{2.2}$$

$$\frac{\partial \rho_g U_\alpha}{\partial t} + \frac{\partial}{\partial x_\beta}(\rho_g U_\alpha U_\beta) = -\frac{\partial \Pi}{\partial x_\alpha} + \frac{\partial \tau_{\alpha\beta}}{\partial x_\beta}\,, \tag{2.3}$$

$$\rho_g c_{p,g} \frac{\partial T_g}{\partial t} + \rho_g c_{p,g} \frac{\partial (U_\beta T_g)}{\partial x_\beta} = \frac{\partial}{\partial x_\beta}\left(\lambda_g \frac{\partial T_g}{\partial x_\beta}\right) - \rho_g \frac{\partial T_g}{\partial x_\beta} \sum_i^n c_{p,i} Y_i V_{\beta,i} + \dot{Q}\,, \tag{2.4}$$

where ρ_g is the density of the gas phase, U_β the bulk velocity in β direction, Π the pressure, $\tau_{\alpha\beta}$ the viscous stress tensor, T_g the temperature, λ_g the thermal conductivity, n the number of gaseous species, $c_{p,g}$ the specific heat of the mixture at constant pressure, and $\dot{Q}$ the heat released from the chemical reactions in the gas phase. Within the low-Mach formulation, Π becomes a projection to enforce mass conservation through the Poisson equation. For the i^{th} gas phase species, Y_i is its mass fraction, $V_{\beta,i}$ the diffusion velocity in β direction and $\dot{M}_i$ the mass production or consumption rate by homogeneous chemical reactions. $V_{\beta,i}$ in Eqs. (2.2) and (2.4) is calculated from the Curtiss-Hirschfelder approximation as

$$V_{\beta,i} = -\frac{1}{Y_i} d_i \frac{W_i}{W} \frac{\partial X_i}{\partial x_\beta} + V_\beta^c \tag{2.5}$$

with

$$V_\beta^c = \sum_{i=1}^n d_i \frac{W_i}{W} \frac{\partial X_i}{\partial x_\beta}\,. \tag{2.6}$$

d_i, W_i, and X_i denote the diffusion coefficient, the molar mass, and the molar fraction of the i^{th} species, respectively. W is the molar mass of the gaseous mixture. Assuming unity Lewis number, species diffusion coefficients are calculated from the thermal diffusion coefficient. In Eqs. (2.5) and (2.6), V_β^c indicates the correction velocity to enforce mass conservation. Based on the Newtonian fluid assumption with Stokes hypothesis, viscous stresses can be computed as

$$\tau_{\alpha\beta} = \mu_g \left[\left(\frac{\partial U_\alpha}{\partial x_\beta} + \frac{\partial U_\beta}{\partial x_\alpha}\right) - \frac{2}{3}\frac{\partial U_\gamma}{\partial x_\gamma}\delta_{\alpha\beta}\right]\,, \tag{2.7}$$

where μ_g is the dynamic viscosity of the gaseous mixture and $\delta_{\alpha\beta}$ the Kronecker delta function. The heat released from the homogeneous reactions in the gas

phase, is calculated as

$$\dot{Q} = -\sum_{i}^{n} h_i \dot{M}_i \,, \tag{2.8}$$

where h_i is the enthalpy of the i^{th} species.

The ideal gas equation of state is used to close the system of equations. Transport coefficients, reaction rates, and thermodynamic relations of the mixture are obtained from the mechanism developed by Blanquart et al. [90] and extended by Cai and Pitsch [91]. The $H_2 - CO$ part of this mechanism is applied which contains 14 species and 78 reactions.

2.1.2 Solid phase

Mass and species transport is neglected within the solid phase. Thus, for the solid phase, only the energy equation has to be solved given by

$$\rho_s c_{p,s} \frac{\partial T_s}{\partial t} = \frac{\partial}{\partial x_\beta} \left(\lambda_s \frac{\partial T_s}{\partial x_\beta} \right) . \tag{2.9}$$

Here, T_s, λ_s , ρ_s, and $c_{p,s}$ are temperature, thermal conductivity, density, and specific heat at constant pressure of the solid phase, respectively. Char particle density mainly depends on the volatile content in the raw coal and the oxygen composition in the surrounding gas [92]. For coal of similar volatile content to the Colombian bituminous, Moloney et al. [93] reported a density of 560 ± 150 kg/m^3. The Colombian bituminous char considered in the current study is assumed to have $\rho_s = 560$ kg/m^3. The value of the specific heat $c_{p,s} = 2000$ J/(kg K) is taken from Murphy and Shaddix [22]. They applied this value of $c_{p,s}$ for the chars from both Highvale and US eastern bituminous coals. Zhang and Bar-Ziv [94] measured carbon particle thermal conductivity and showed that λ_s varies from 0.4 W/(mK) at 400 K to 1.3 W/(mK) at 1100 K. For applications within the temperature range from 1690 to 3000 K investigated in Hecht et al. [12], $\lambda_s = 1.33$ W/(mK) has been chosen. This value has been applied by Shaddix et al. [10] as well. Therefore, for the temperature range in the current study from 1500-2300 K, a value for the thermal conductivity of $\lambda_s = 1.33$ W/(mK) is used.

2.1.3 Solid-gas interface

At the solid-gas interface, $\partial\Omega_p$, species, mass, and energy source terms, $\dot{m}_i$, $\dot{m}$, and $\dot{e}$ exist (see Fig. 2.1). The exchange of species, mass, and energy

between the interface and the gaseous region next to the interface ($\Omega_{g|p}$) is realized with the corresponding fluxes, $F_{Y_i}|_g$, $F_m|_g$, and $F_e|_g$, respectively (see Fig. 2.1). With the assumption that there is no mass transport inside the particle, only the energy flux, $F_e|_s$ is present towards the solid phase. The balance between species, mass, and energy source terms and corresponding fluxes to both gas phase and solid yield the interface equations for species, mass, and energy as [20]

$$\underbrace{\rho_g U_\beta Y_i n_\beta}_{\text{convection}} + \underbrace{\rho_g V_{\beta,i} Y_i n_\beta}_{\text{diffusion}} = \dot{m}_i \,, \tag{2.10}$$

$$\rho_g U_\beta n_\beta = \dot{m} \,, \tag{2.11}$$

$$\underbrace{\lambda_s \frac{\partial T}{\partial x_\beta}\Big|_s n_\beta}_{\text{conduction}_\text{s}} - \underbrace{\lambda_g \frac{\partial T}{\partial x_\beta}\Big|_g n_\beta}_{\text{conduction}_\text{g}} + \underbrace{T \sum_i^n c_{p,i} \dot{m}_i}_{\text{advection}} = \dot{e} \,. \tag{2.12}$$

$\dot{m}_i$ is calculated based on the production or consumption rate of the i^{th} gas phase species due to the heterogeneous reactions at the interface. In Eq. (2.11), $\dot{m}$ is equal to the carbon consumption rate, $\dot{m}_\text{C}$, computed as

$$\dot{m}_\text{C} = \sum_i^n \dot{m}_i \,, \tag{2.13}$$

which is defined to be positive for a flux into the gas phase. With a known $\dot{m}$, the so-called Stefan flow velocity, U_β, can be computed, which has the same direction as the unit normal vector of the interface surface towards the gas phase, n_β. In Eq. (2.12), the energy source term, $\dot{e}$, is calculated as

$$\dot{e} = \underbrace{-\sum_i^n h_i \dot{m}_i}_{\text{surface reactions}} \underbrace{-\epsilon\sigma(T^4 - T_w^4)}_{\text{radiation}} , \tag{2.14}$$

where T_w is the wall temperature, ϵ the emissivity coefficient, and σ the Stefan-Boltzmann constant. Production and consumption rates of each species due to the heterogeneous reactions at the interface are computed using a chemical mechanism taken from Bradley et al. [95] with eight gaseous species and five

reactions,

$$\mathrm{C(s)} + \frac{1}{2}\mathrm{O_2} \rightarrow \mathrm{CO}\,, \tag{2.15}$$

$$\mathrm{C(s)} + \mathrm{CO_2} \rightarrow 2\mathrm{CO}\,, \tag{2.16}$$

$$\mathrm{C(s)} + \mathrm{H_2O} \rightarrow \mathrm{CO} + \mathrm{H_2}\,, \tag{2.17}$$

$$\mathrm{C(s)} + \mathrm{OH} \rightarrow \mathrm{CO} + \mathrm{H}\,, \tag{2.18}$$

$$\mathrm{C(s)} + \mathrm{O} \rightarrow \mathrm{CO}\,, \tag{2.19}$$

where C(s) refers to the solid carbon. This mechanism is chosen due to its consideration of species and radicals, which allows a good gas phase coupling in the presented simulation framework [96]. Table 2.1 represents the kinetic parameters for heterogeneous reactions, where P_i refers to the partial pressure of the i^{th} species. For reaction r, R_r is the reaction rate, K_r the rate coefficient computed as $K_r = A_r T^{B_r} \exp(-E_r/RT)$. Here, A_r is the pre-exponential factor, B_r the temperature exponent, E_r the activation energy, and R the universal gas constant.

To account for particle porosity and species partial penetration into the porous particle, similar to the approach used by Lee et al. [21], a constant multiplicative factor, κ is applied in each heterogeneous reaction rate expression. A value of $\kappa = 12$ was chosen to represent the ratio of the effective area provided by pores (in size range of 0.4-50 μm) to the apparent particle surface area. This choice yields a particle effective specific surface area equal to 0.852 $\mathrm{m^2/g}$, which is in the range mentioned by Hecht et al. [8] from 0.225 $\mathrm{m^2/g}$ to 8 $\mathrm{m^2/g}$ in oxygen concentrations of 36% down to 12%. Furthermore, the sensitivity of the results to the kinetic parameters is studied. The results show strong sensitivity with respect to the pre-exponential factor A_i, when it is varied

r	B_r	E_r [kJ/mol]	A_r	R_r [kg/(m^{2}s)]
15a	0	125.6	2400 [kg/(m^2 s atm)]	$R_{15} = \frac{K_{15a}P_{\mathrm{O_2}}\xi}{1+K_{15b}P_{\mathrm{O_2}}} + K_{15c}P_{\mathrm{O_2}}(1-\xi)$
15b	0	-17.17	21.3 [1/atm]	
15c	0	63.64	0.535 [kg/(m^2 s atm)]	$\xi = 1/(1+\frac{K_{15d}}{K_{15c}P_{\mathrm{O_2}}})$
15d	0	406.1	18.1×10^6 [kg/(m^2 s)]	
16	0	285	9×10^3 [kg/(m^2 s atm$^{0.5}$)]	$R_{16} = K_{16}P_{\mathrm{CO_2}}^{0.5}$
17	0	288	4.8×10^5 [kg/(m^2 s atm$^{0.5}$)]	$R_{17} = K_{17}P_{\mathrm{H_2O}}^{0.5}$
18	-0.5	0	361 [kg K$^{0.5}$/(m^2 s atm)]	$R_{18} = K_{18}P_{\mathrm{OH}}$
19	-0.5	0	665.5 [kg K$^{0.5}$/(m^2 s atm)]	$R_{19} = K_{19}P_{\mathrm{O}}$

Table 2.1: Kinetic parameters for heterogeneous reactions Eq. (2.15-2.19) taken from Bradley et al. [95].

from $0.25A_i$ to A_i. In this range, a difference in the steady state temperature of about 400 K is observed.

2.1.4 Initial and boundary conditions

Due to symmetry about the x_1 axis, only half of the domain ($[-50D_p, 100D_p] \times [0, 50D_p]$) is computed. The initial conditions in the gas phase at time $t = 0$ are

$$Y_i(x_1, x_2, 0) = Y_i^0\,, \tag{2.20}$$

$$T_g(x_1, x_2, 0) = T_g^0\,, \tag{2.21}$$

$$\mathbf{U}(x_1, x_2, 0) = (U_1^0, 0, 0)\,. \tag{2.22}$$

The initial density in the gas phase is calculated via the equation of state. The initial temperature in the solid phase, T_s is given as

$$T_s(x_1, x_2, 0) = T_s^0\,. \tag{2.23}$$

At the inlet ($x_1 = x_1^-$), all gas phase variables are specified by the Dirichlet boundary condition according to

$$Y_i(x_1^-, x_2, t) = Y_i^0\,, \tag{2.24}$$

$$T_g(x_1^-, x_2, t) = T_g^0\,, \tag{2.25}$$

$$\mathbf{U}(x_1^-, x_2, t) = (U_1^0, 0, 0)\,. \tag{2.26}$$

while for $x_2 = x_2^+$ the free stream and for $x_2 = (x_2^- + x_2^+)/2$ symmetry boundary with the Neumann boundary condition (zero flux) is used. At the outlet ($x_1 = x_1^+$), the Neumann boundary conditions are used for Y_i, T_g, and Π, while $\mathbf{U}$ is specified so that during the simulation the total mass in the domain remains constant. Furthermore, Eqs. (2.10)-(2.12) are solved to obtain Y_i, $\mathbf{U}$, and T at the solid-gas interface. The calculated value of Y_i and $\mathbf{U}$ at the interface enforce the Dirichlet boundary conditions on the gas phase. At the interface, T imposes the Dirichlet boundary conditions on the gas (specifying T_g) and the Neumann boundary conditions on the solid phase (specifying $\partial T_s / \partial x_\beta$).

2.1.5 Particle shape and grid size

In resolved particle simulations, coal particles are often treated as perfect spheres [7, 12, 15, 16]. However, it is well known that particle geometries are

complex. An example is given in Fig. 2.2 showing SEM images of Colombian bituminous raw coal. Here, some of the particles might be well approximated as spheres, others rather as cylinders, and both shapes could be studied as limiting cases. Here, the cylindrical geometry is considered and as a consequence, the particles are assumed to be infinitely long rods, which can then be studied in 2-D simulations. This geometry has the advantage that also particle arrays can be studied using 2-D simulations, which is quite useful when detailed chemistry simulations are performed. The computational domain is discretized by a Cartesian grid, which is refined around the particle by 45 cells with sizes of $|\Delta \mathbf{x}| = 0.02 D_p$. This mesh spacing is comparable with the work of Tufano et al. [58], who used 50 cells per particle for resolved simulations

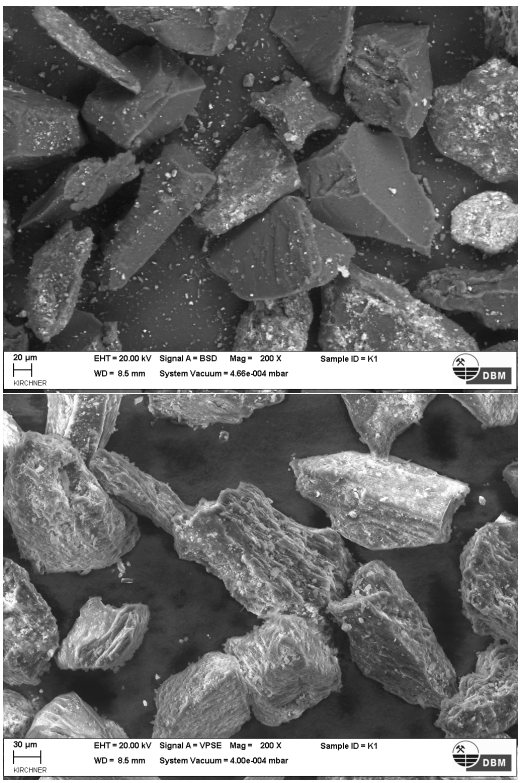

Figure 2.2: SEM images of the Colombian bituminous raw coal [3].

at similar Reynolds numbers. The grid was verified in simulations of the particle drag coefficient and comparisons with experimental measurement by Tritton [97] shown in Fig. 2.3. The drag coefficient C_D of a circular cylinder is computed as

$$C_D = \frac{\int_A \{\tau_{\alpha\beta} \cdot n_\beta\} \cdot n_\alpha dA}{\frac{1}{2}\rho_g U_1^2 A_2}, \tag{2.27}$$

where A and A_2 indicate the particle surface area and its projection along x_2 perpendicular to the flow direction.

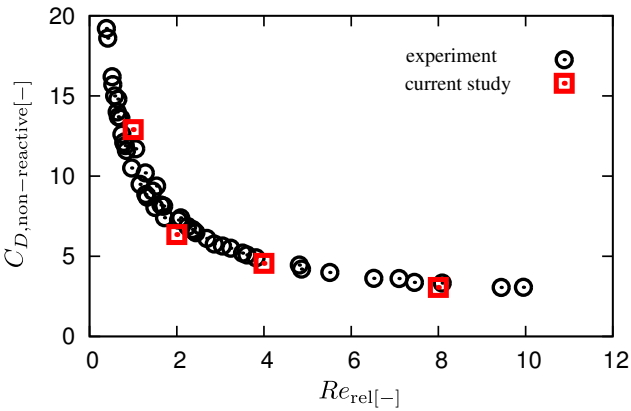

Figure 2.3: Drag coefficient of a non-reactive circular cylinder calculated numerically in the current study and compared with experimental data by Tritton [97].

2.1.6 Numerical methods

The in-house code CIAO is used to solve the presented model equations numerically. From CIAO, a semi-implicit finite difference low-Mach solver is used with 2$^{\mathrm{nd}}$ order accuracy in space and time. Figure 2.4 shows a flowchart of the low-Mach solver in CIAO. The numerical methods in CIAO are described in Desjardins et al. [98]. The 2$^{\mathrm{nd}}$ order staggered grid method is used to discretize Eqs. (2.1)-(2.4) both in time and space and the Crank-Nicolson method is used for time advancement along with an iterative predictor-corrector scheme. During time-marching from t to $t + \Delta t$ (from step n to $n + 1$), interface equations (2.10)-(2.12) are solved in Pre-Step to provide boundary conditions for the equations in the solid and gas phase. Then, Eqs. (2.1)-(2.4) in the gas

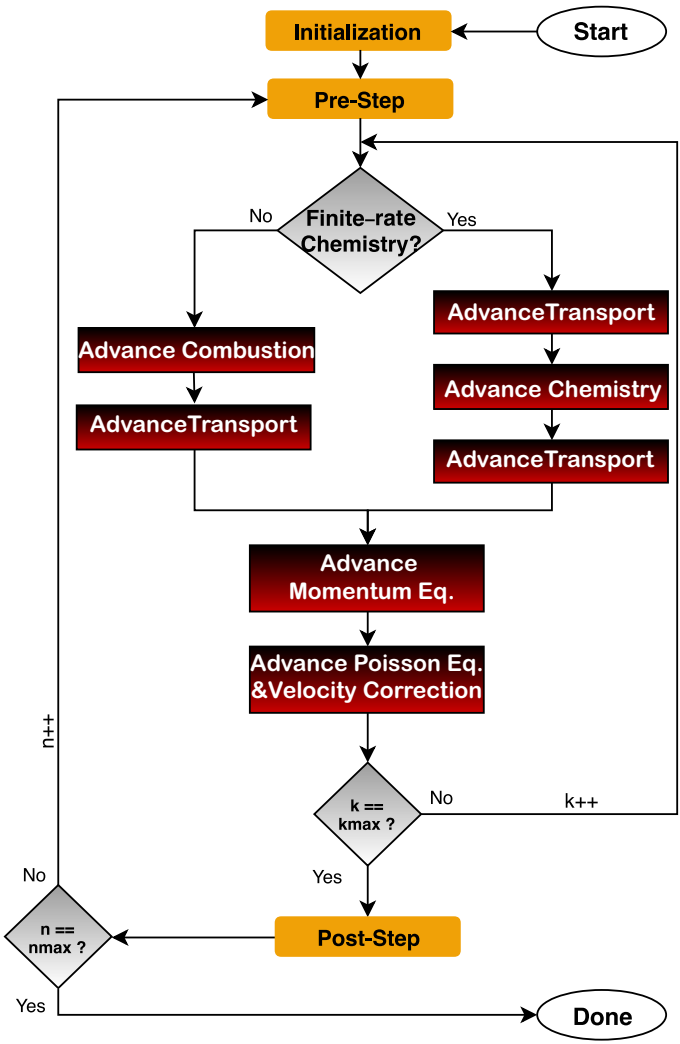

Figure 2.4: Flowchart of the low-Mach solver in the CIAO code.

and Eq. (2.9) in the solid phase are advanced in time separately.

In the gas phase, first, the scalar equations (Eqs. (2.2) and (2.4)) are advanced

for species mass fractions and temperature, respectively. Solving the scalar equations follows the Strang splitting approach [99] with two independent operators as

$$\mathcal{F}^{\text{Trans}}_{\Delta t/2}\mathcal{F}^{\text{Chem}}_{\Delta t}\mathcal{F}^{\text{Trans}}_{\Delta t/2}(Y_i^k, T_g^k) \rightarrow (Y_i^{k+1}, T_g^{k+1})\,, \tag{2.28}$$

where the upper index k denotes the time step and $\mathcal{F}^{\text{Chem}}_{\Delta t}$ and $\mathcal{F}^{\text{Trans}}_{\Delta t/2}$ account for homogeneous reactions and for transport, respectively, and are given as

$$\mathcal{F}^{\text{Chem}}_{\Delta t}: \begin{cases} \dfrac{\partial \rho_g Y_i}{\partial t} = \dot{M}_i \\ \rho_g c_{p,g}\dfrac{\partial T_g}{\partial t} = -\sum_i^n h_i \dot{M}_i \end{cases} \tag{2.29}$$

$$\mathcal{F}^{\text{Trans}}_{\Delta t}: \begin{cases} \dfrac{\partial \rho_g Y_i}{\partial t} + \dfrac{\partial}{\partial x_\beta}(\rho_g(U_\beta + V_{\beta,i})Y_i) = 0 \\ \rho_g c_{p,g}\dfrac{\partial T_g}{\partial t} + \rho_g c_{p,g}\dfrac{\partial (U_\beta T_g)}{\partial x_\beta} = \\ \quad \dfrac{\partial}{\partial x_\beta}(\lambda_g \dfrac{\partial T_g}{\partial x_\beta}) - \rho_g \dfrac{\partial T_g}{\partial x_\beta}\sum_i^n c_{p,i} Y_i V_{\beta,i} \end{cases} \tag{2.30}$$

The chemistry operator in Eq. (2.29) is an ODE system, which is solved by a time-implicit backward difference method as implemented in DVODE [100]. For the transport operator, convective fluxes are calculated using a 3$^{\text{rd}}$ order WENO (Weighted Essentially Non-Oscillatory) scheme [101]. After updating species mass fractions and temperature, density is updated using the equation of state. Finally, the Poisson equation (derived from Eq. (2.1) and (2.3) based on the low-Mach assumption) is advanced using the multi-grid HYPRE solver [102] to update the velocity and pressure fields in the gas phase. As shown in Fig. 2.4, gas phase equations are solved in each time step for kmax sub iterations, which has a value of 5 in the current study.

In the solid phase, the energy equation, Eq. (2.9), is spatially discretized using a 2$^{\text{nd}}$ order central difference scheme. A Crank-Nicolson scheme with an iterative predictor-corrector update has been applied for the time advancement.

Simulations were performed on the RWTH Compute Cluster, which is part of JARA-HPC partition consisting of Intel Xeon Processors X5675 (Westmere) with a base frequency of 3.06 GHz. For each case study, 168 CPUs were used for almost 4 days.

2.2 Validation against experiment

In this section, a validation of the model should be performed. It is important to note that the purpose here is not to prove this as a generally applicable model, but rather to demonstrate that the interaction of chemistry and transport is described sufficiently adequate that these interactions can be studied in terms of the governing non-dimensional parameters as done in the remainder of the paper.

2.2.1 Experimental setup

Experimental data measured in a laminar flow reactor (Fig. 2.1) have been used. A detailed description of this reactor is given in Schiemann et al. [23]. The reactor is a small glass channel (5×5 cm^2 cross section), in which coal particles are entrained in a combustion gas atmosphere with excess oxygen. For the present study, an exemplary Colombian bituminous coal was chosen, which has been studied extensively for its combustion behavior in Schiemann et al. [23], Vorobiev et al. [24], and Köser et al. [35]. Atmospheres with N_2 and CO_2 diluents were chosen to represent the classical air-fired case in comparison to oxy-fuel conditions.

The combustion behavior is analyzed by temperature and particle diameter measurements using an imaging stereoscopic pyrometer, which is described in [23] and [24]. Since the main focus of the present study is char combustion, the data set was carefully analyzed for volatile flames, which were removed from the data set mainly based on the event size [23]. Before particle injection into the burner, mean temperatures of the gas phase are measured along the burner height. Figure 2.5 shows the gas phase temperature profile in both air and oxy-atmospheres. Experimentally obtained gas compositions in the flat flame burner are given in Tab. 2.2. The experiments are designed so that $X^0_{O_2} = 0.3$ in both atmospheres.

Test Cases	Diluent	$Y^0_{O_2}$	$Y^0_{H_2O}$	$Y^0_{CO_2}$	$Y^0_{N_2}$
Air	N_2	0.326	0.086	0.105	0.483
Oxy	CO_2	0.262	0.087	0.651	0.0

Table 2.2: Measured gas composition at the flat flame burner for two test cases.

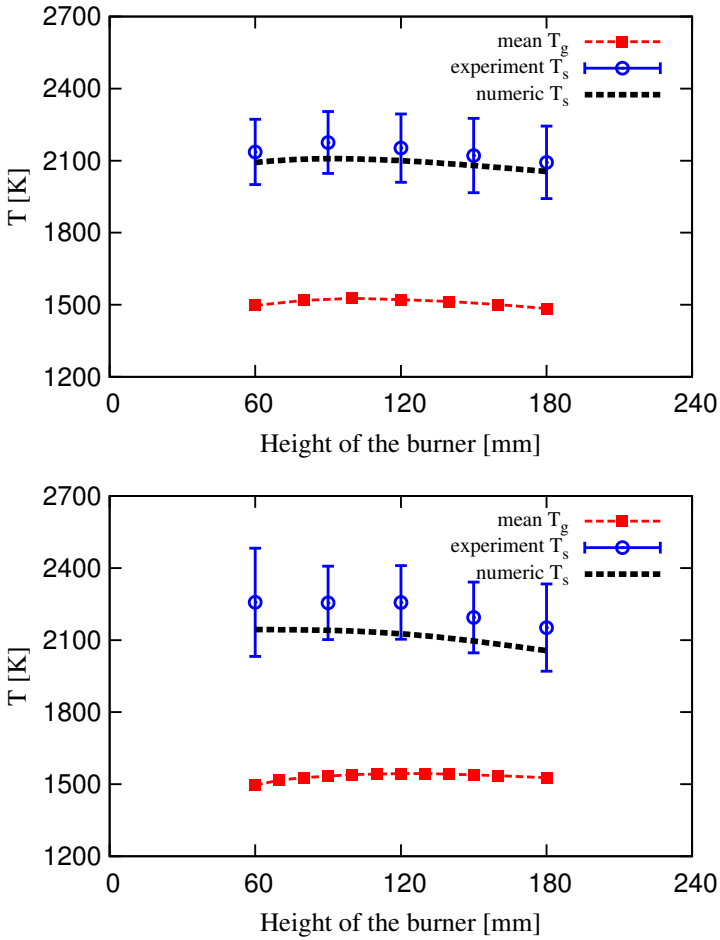

Figure 2.5: The initial gas phase temperature plus measured and computed maximum particle temperature along the burner height.The upper plot shows the temperature distribution in oxy-, the lower plot in air atmosphere.

2.2.2 Char particle temperature

After particle injection into the burner, coal particles undergo devolatilization and then char burnout. To capture char combustion and to ensure that

devolatilization is finished, the measurement point begins at 60 mm height above the burner (Fig. 2.1), which corresponds to a particle residence time of 35 and 40 ms in air and in oxy-atmospheres, respectively. Char particle temperatures at burner heights of 60, 90, 120, 150, and 180 mm have been measured, which correspond to residence times of 35-86 ms in air and 42-95 ms in oxy-atmosphere.

To validate the model, each measurement point is computed to steady state, which for all points is reached in less than 0.5 ms, using the conditions of the local atmosphere. The char combustion is computed for a diameter of $D_p = 100$ μm in both air (N_2 diluent) and oxy- (CO_2 diluent) atmospheres. In the computational domain, the initial conditions and the boundary conditions at the upstream boundary are given by the measured gas compositions (Tab. 2.2) and temperatures (Fig. 2.5) from the experiment. For each atmosphere, U_1^0 is computed so that the relative Reynolds number of the particle, $Re_{\mathrm{rel}} = \rho^0 U_1^0 D_p / \mu^0$ becomes 0.125. This value was shown by Knappstein et al. [103] to be appropriate for this kind of configuration. Computed particle temperatures are recorded and shown in Fig. 2.5. Comparing the particle temperatures in Fig. 2.5 reveals that the computed temperatures in both atmospheres are within the experiment's confidence interval. This provides some validation to show that the current resolved model for char particle combustion leads to suitable results to be used for the following investigation.

2.3 Results and discussions

In this section, first, the influence of the oxidizing environment on single char particle combustion will be investigated by analyzing results from computations for cases with both air and oxy-atmospheres. Second, the interactions between the gas flow and the chemistry will be studied.

The gas compositions of both air and oxy-atmospheres used in this study are defined in Tab. 2.2. To capture the transient combustion behavior, the initial gas and particle temperatures are set to 1500 K. In both atmospheres, $D_p = 100$ μm. Later in this section, particle Reynolds numbers are varied from 0.125 to 8. The upper value of the Reynolds numbers studied here is chosen considering the observed gas velocity range in Aachen's 100 kW swirl burner [104]. Recently, Franchetti et al. [105] performed an LES study of the oxy-coal furnace of Aachen's swirl burner. The highest magnitude of mean velocity is reported to be in the order of 22 m/s. Assuming that some of the 100 μm particles experience a slip velocity around 22 m/s, the maximum

particle Reynolds numbers are $Re_{\mathrm{rel}} \approx 10$.

The computed results will be presented in terms of a set of non-dimensional parameters, which are defined as $x_1^* = x_1/D_p$, $x_2^* = x_2/D_p$, and $t^* = t/\tau_{\mathrm{c,ref}}$, where $\tau_{\mathrm{c,ref}}$ is the reference time scale defined as $\tau_{\mathrm{c,ref}} = D_p/U_1^0$ based on the value of U_1^0 in oxy-atmosphere with $X_{\mathrm{O_2}}^0 = 0.3$. Each simulation is performed in time up to $60 \times \tau_{\mathrm{c,ref}}$. It is seen in the simulations and also the experiments that at each condition, the particles are in a quasi-steady state. Here, the simulations are only for the initial unsteady phase until a steady state is reached (3 ms). Further changes of porosity and particle diameter then happen at a much longer time scale and burnout at a time scale of about 200 ms. Char combustion is computed up to 3 ms, which is much less than of the whole char burnout time (around 200 ms). Thus, density variations can be neglected for the small time period compared with the total burnout time [106]. Furthermore, it was shown by experimental determination of particle diameters during char burnout of this coal sample under similar conditions [24, 107] and in theory by Mitchell et al. [106] that diameter changes during the early burning phase are rather small. Thus, for the short time frame considered, diameter changes are neglected. Later times could be simulated by quasi-steady calculations at different particle diameters and porosity, which is considered here by independently varying Reynolds and Damköhler numbers of the particle.

2.3.1 Oxy- versus air atmosphere

In this section, char combustion is analyzed in air and oxy-atmospheres. Mass and energy exchanges between the particle and its surrounding gas are studied and comparisons between the different atmospheres are made. The simulations for the initial comparison are performed for $Re_{\mathrm{rel}} = 1$ in both atmospheres. Figure 2.6 shows the evolution of the maximum temperature in the gas phase, $T_{g_{\max}}$, in both air and oxy-atmospheres. A higher temperature in the oxy- than in the air atmosphere is observed at the early stage of char combustion, while afterwards until $t^* = 60$, higher $T_{g_{\max}}$ is obtained in the air atmosphere. Moreover, Figure 2.7a shows that at $t^* = 60$, not only $T_{g_{\max}}$, but also T_g around the particle is higher in the air compared to the oxy-atmosphere. The temperatures inside the particle vary almost linearly in time with a heating rate of about 10^5 K/s. The radial changes of temperature inside the particle are less than 10 K.

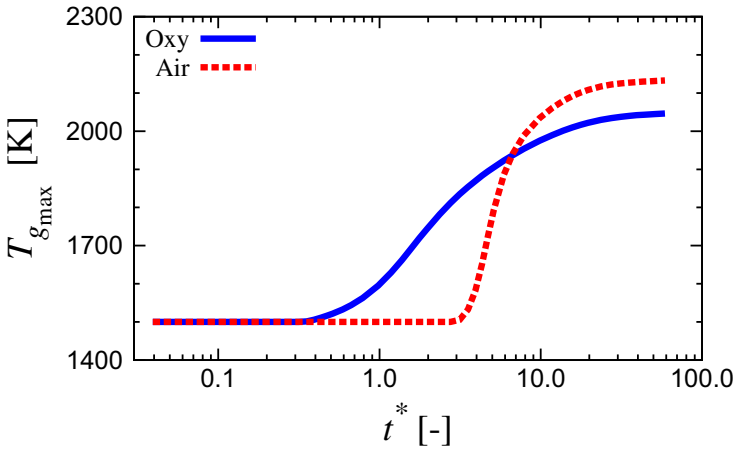

Figure 2.6: Evolution of the maximum temperature in the gas phase, $T_{g_{\max}}$, in both oxy- and air atmospheres with $Re_{\text{rel}} = 1$ and $X^0_{O_2} = 0.3$.

2.3.1.1 Mass exchange

Locating a char particle in a hot oxidizing environment leads to heterogeneous reactions at the solid-gas interface (see Eqs. (2.15)-(2.19)). The gaseous reactants and products of these reactions are transported between the interface and the gas phase by diffusive and convective fluxes (see Eqs. (2.10) and (2.11)). The main product of all heterogeneous reactions is CO, which is transported to the gas phase. There, CO undergoes oxidation due to the homogeneous reactions given in the mechanism introduced in section 2.1.

Analyzing the data reveals that in both atmospheres, the surface oxidation reaction, Eq. (2.15), has the highest CO production rate (more than 95%) among all heterogeneous reactions. Hecht et al. [9] found that even for oxy-combustion at elevated partial pressure of oxygen, the oxidation reaction is dominating in char combustion [9]. This is in agreement with the present findings that the oxidation reaction contributes to more than 95% of carbon consumption. Because of the relatively high activation energies of the gasification reactions, it could be expected that at higher temperatures under oxy-fuel condition, these reactions will have a higher contribution. Therefore, to quantify mass exchange, the relevant parameters of the involved species in this particular surface oxidation reaction will be studied in detail.

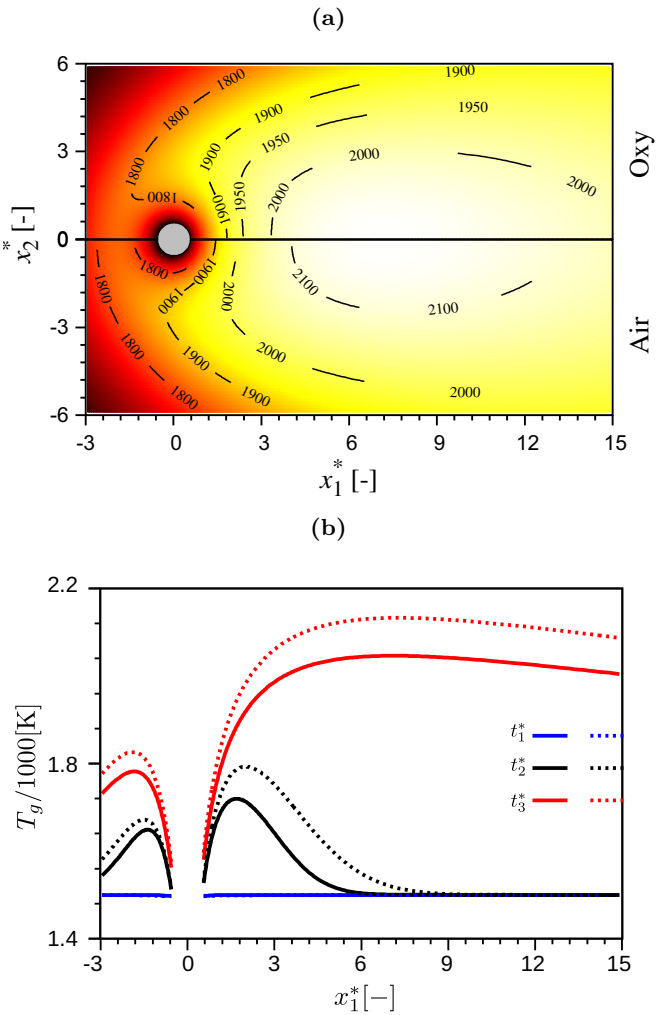

Figure 2.7: (a) 2-D distribution of gas phase temperature, T_g, in Kelvin at $t^* = 60$ and (b) evolution for oxy- (solid line) and air (dashed line) atmospheres along the centerline in the vicinity of the particle with $Re_{\text{rel}} = 1$ and $X^0_{\text{O}_2} = 0.3$.

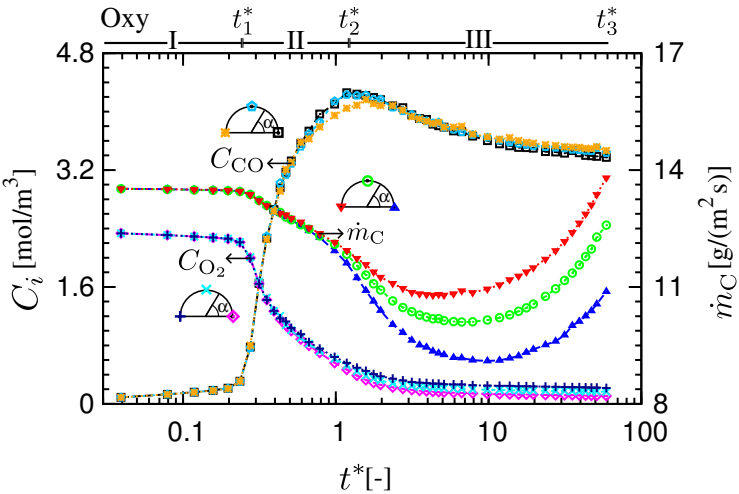

Figure 2.8: Evolution of C_{CO}, C_{O_2}, and $\dot{m}_C$ at the solid-gas interface via three probes located at angles $\alpha = 0$, $\pi/2$, and π [rad] in the oxy-atmosphere with $Re_{rel} = 1$.

Figure 2.8 shows the evolution of $\dot{m}_C$, C_{O_2}, and C_{CO} at the particle surface for three different angles $\alpha = 0$, $\pi/2$, and π. C_i is the molar concentration of the i^{th} species. The evolution of carbon monoxide at the particle surface can be separated into three different phases (see Fig. 2.8). In phase I ($t^* < t_1^*$), the value of C_{CO} increases very slowly. This phase is followed by phase II, which is initiated by the ignition of the gas phase. During this phase, the amount of C_{CO} increases sharply until it reaches a maximum at $t^* = t_2^*$. Finally, in phase III ($t_2^* < t^* < t_3^*$), C_{CO} is decreasing to approach a constant value. It can be observed in Fig. 2.8 that C_{O_2} weakly decreases in phase I. In phase II, this decrease is significantly enhanced, before slowing down again in phase III. Furthermore, Fig. 2.8 shows that $\dot{m}_C$ is decreasing during phase I and II, while it shows a minimum with a subsequent increase within phase III.

The magnitude of $\dot{m}_C$ strongly depends on the rate of the surface oxidation reaction, which is a function of C_{O_2} and the particle surface temperature. During phase I and II, the C_{O_2} drop leads to a reduction of $\dot{m}_C$, while during phase III, the temperature increases (see Fig. 2.7b). This temperature increase compensates the impact of the C_{O_2} drop, and thus leads to the reversed trend

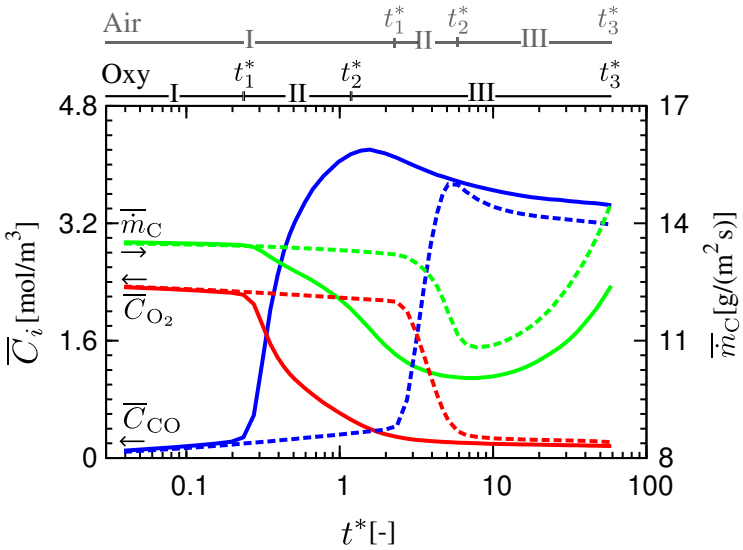

Figure 2.9: Evolution of $\overline{C}_{CO}$, $\overline{C}_{O_2}$, and $\overline{\dot{m}}_C$ at the solid-gas interface, in the oxy- (solid line) and air atmospheres (dashed line).

in the $\dot{m}_C$ evolution.

Due to the non-uniform distribution of the aforementioned quantities, $\dot{m}_C$ and C_i are averaged on the particle surface to compare oxy- and air atmosphere. These averages are referred to as $\overline{\dot{m}}_C$ and $\overline{C}_i$, and shown over time in Fig. 2.9 for both atmospheres. A comparison between the air and oxy-atmospheres reveals that in spite of an increased $\overline{C}_{CO}$ in the oxy-atmosphere, the corresponding $\overline{\dot{m}}_C$ profile exhibits lower values. Further, it is seen in Fig. 2.9 that the starting point of phase II in the oxy-atmosphere lies before that in the air atmosphere. This leads to a time shift between the profiles in the oxy- and air atmosphere. Therefore, to find the reasons for different mass exchange in the oxy- and air atmospheres, the transition from phase I to II must be studied in detail.

2.3.1.2 Budget of interface mass balance

To understand the underlying physics at the transition from phase I to II, the evolution of the O_2 and CO species source terms due to the surface reactions and their corresponding diffusive and convective fluxes have to be

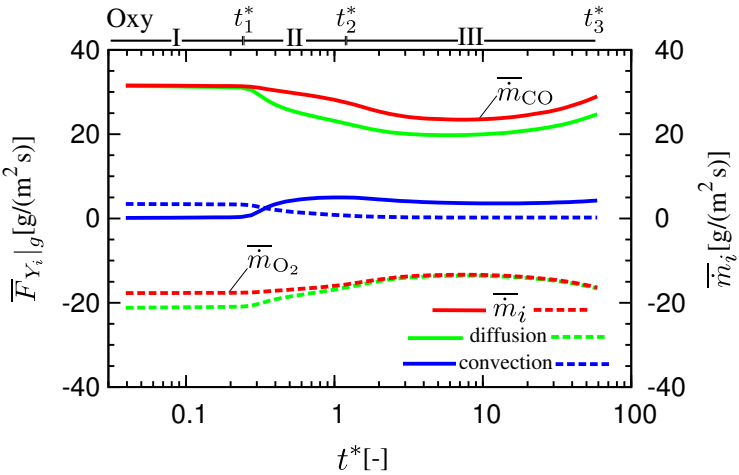

Figure 2.10: Evolution of $\overline{\dot{m}}_i$ and $\overline{F}_{Y_i|g}$ (due to the diffusion and convection) of the species CO (solid line) and O_2 (dashed line) at the interface, for the oxy-atmosphere.

quantified at the interface. These are related through the budget of Eq. (2.2), which states that the sum of convective and diffusive species fluxes at the interface are equal to the chemical production rates of the surface reactions. To analyze this budget, the species production rates, $\dot{m}_i$, and species mass fraction fluxes, $F_{Y_i|g}$ are averaged on the particle surface. The species fluxes are defined positive away from the interface. Figure 2.10 shows the evolution of these averaged quantities, $\overline{F}_{Y_i|g}$ and $\overline{\dot{m}}_i$, for the oxy-atmosphere. Within the entire investigated time frame, the absolute value of the diffusive flux exceeds convection. Therefore, it is concluded that the diffusive fluxes are the dominant transport mechanism at the interface. Figure 2.10 further indicates that the absolute value of the species diffusive flux first decreases gradually in phase I and then stronger in phase II. A qualitatively similar behavior is observed for $\overline{F}_{Y_i|g}$ and $\overline{\dot{m}}_i$ in air atmosphere.

The lower O_2 diffusive flux supplies less O_2 at the interface and hence, $\overline{C}_{O_2}$ at the interface reduces. In contrast, the lower CO diffusive flux diffuses less CO away from the interface and thus, $\overline{C}_{CO}$ at the interface increases. Therefore, a significant reduction in the diffusive fluxes of O_2 and CO enforces a sharp drop in $\overline{C}_{O_2}$ and a significant increase in $\overline{C}_{CO}$ along with transition from phase I to II (see Fig. 2.9).

The absolute value of the O_2 and CO diffusive fluxes are decreasing because of O_2 deficiency and CO abundance at $\Omega_{g|p}$. During phase I, C_{O_2} deficiency and C_{CO} abundance at $\Omega_{g|p}$ are caused by a slow transport in the gas phase that cannot compensate the impact of the surface oxidation reaction. However, within phase II, the reason for a significant reduction in C_{O_2} at $\Omega_{g|p}$ is not only the slow transport, but also O_2 consumption by homogeneous reactions. Figure 2.11 shows the evolution of $\overline{\dot{C}}_{O_2}$, which is the volume-averaged value of $\dot{C}_{O_2}$ (over $\Omega_{g|p}$) defined as $\dot{M}_{O_2}/W_{O_2}$. In both atmospheres, the absolute value of $\overline{\dot{C}}_{O_2}$ increases significantly at the beginning of the second phase. However, the maximum absolute value of $\overline{\dot{C}}_{O_2}$ in oxy-atmosphere is almost twice as high as that in air atmosphere. The analysis of the data shows that the reaction

$$O_2 + H \rightarrow OH + O \tag{2.31}$$

is the main contribution to O_2 consumption at $\Omega_{g|p}$ for both the oxy- and air atmospheres. During phase II in the oxy-atmosphere, Eq. (2.31) consumes more O_2 than in air. Consequently, due to the reduced oxygen content, the surface oxidation reaction Eq. 2.15 yields smaller values of $\overline{\dot{m}}_C$ (see Fig. 2.9)

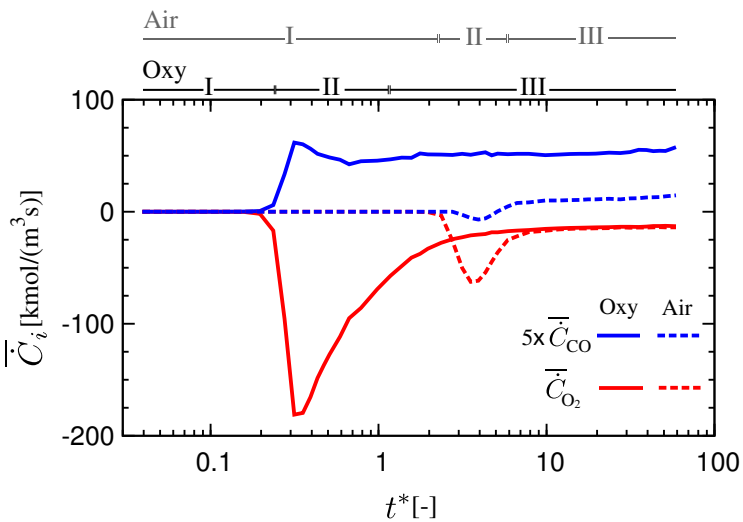

Figure 2.11: Evolution of $\overline{\dot{C}}_{O_2}$ and $\overline{\dot{C}}_{CO}$ in the oxy- (solid line) and air (dashed line) atmospheres.

and $\overline{\dot{m}}_{\mathrm{CO}}$ in the oxy- compared to the air atmosphere.

Figure. 2.9 also shows that at the interface, $\overline{C}_{\mathrm{CO}}$ has a higher value in the oxy- compared with air atmosphere. The reason originates from the CO production within the boundary layer by reaction

$$\mathrm{CO_2 + H \rightarrow CO + OH}\,, \tag{2.32}$$

which leads to an almost three times higher value of $\overline{\dot{C}}_{\mathrm{CO}}$ (at $\Omega_{g|p}$) in the oxy-atmosphere (see Fig 2.11).

Equation (2.31) consumes O_2, which leads to lower values of $\overline{\dot{m}}_{\mathrm{C}}$ in the oxy-atmosphere within phase II (see Fig. 2.9). During phase III, lower temperatures in the oxy-atmosphere (see Fig. 2.7a) keep $\overline{\dot{m}}_{\mathrm{C}}$ lower, which strongly couples the mass exchange to the energy exchange.

2.3.1.3 Budget of interface energy balance

The production of CO, for instance by the surface oxidation reaction (2.15), and the consumption of CO within the gas phase are both exothermic processes. Studying the energy exchange at the solid-gas interface clarifies which process has the main contribution in supplying thermal energy for the system. To quantify the energy exchange at the solid-gas interface, the budget of the energy interface condition in Eq. (2.8) is considered. The energy fluxes, $F_{e|g}$, appearing in that equation and the energy source terms by surface reactions and radiation are shown. The individual terms are defined such that fluxes away from the interface are positive and that the sum of the fluxes equals the sum of the source terms. Due to the non-uniform distribution, these quantities are averaged on the particle surface and referred to as $\overline{F}_{e|g}$ and $\bar{\dot{e}}$. Figure 2.12 illustrates the evolution of the fluxes $\overline{F}_{e|g}$ due to conduction from the interface into the gas phase and into the solid as well as due to advection. Further, the evolution of the individual contributions to $\bar{\dot{e}}$ due to surface reactions and radiation are shown over time in Fig. 2.12. During phase I, almost constant energy fluxes at the solid-gas interface can be observed. Within this time interval, heat released from the surface reactions and conduction from the solid particle provide most of the energy at the interface. This energy is then mostly removed by radiation. During phase II, both conductive fluxes undergo significant variations along with the temperature increase in the vicinity of the particle (see Fig. 2.7b at t_1^* and t_2^*). During phase III, conduction from the gas phase along with surface reactions become the dominant processes supplying energy to the interface, which then heats

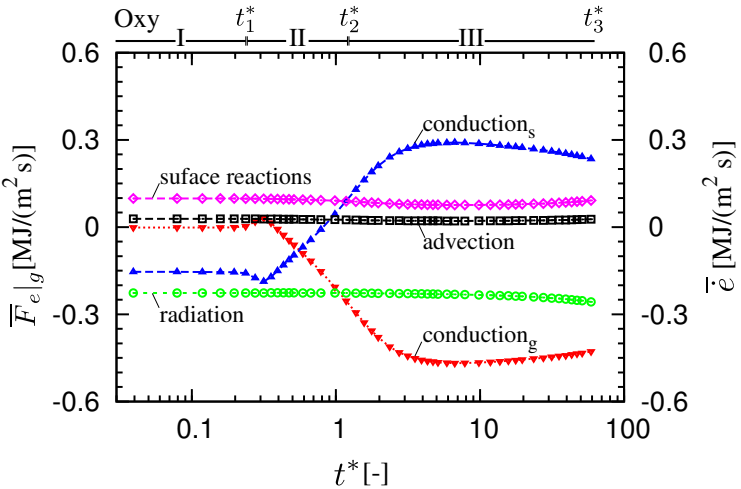

Figure 2.12: Budget of interface energy balance (Eq. 2.10) showing fluxes $\overline{F}_{e|g}$ due to the conduction from the interface into gas and solid phase as well as due to the advection and source terms $\overline{\dot{e}}$ due to surface reactions and radiation at the solid-gas interface in the oxy-atmosphere. Fluxes are defined positive away from the interface and the signs of source terms such that their sum equals the sum of the fluxes.

up the particle and radiates back into the gas phase. In the air atmosphere, the $\overline{F}_{e|g}$ and $\overline{\dot{e}}$ evolutions reveal an analogous behavior. As a consequence, for both oxy- and air atmospheres, during the first phase, the heat release comes from the heterogeneous reactions, while during the third phase, the CO oxidation by homogeneous reactions provides much more energy than the surface oxidation reactions. In phase II, both contributions are equally important.

2.3.1.4 Heat release distribution

Figure 2.13 shows the heat release $\dot{Q}$ from the CO oxidation by homogeneous reactions along the centerline in a region around the particle at t_1^*, t_2^*, and t_3^* in both oxy- and air atmospheres. In both atmospheres, within the entire investigated time frame, $\dot{Q} < 0$ next to the interface, while the rest of the domain exhibits $\dot{Q} \geq 0$. At t_1^*, the endothermic homogeneous reactions Eq. (2.31) and Eq. (2.32) possess the highest rates and constitute the biggest

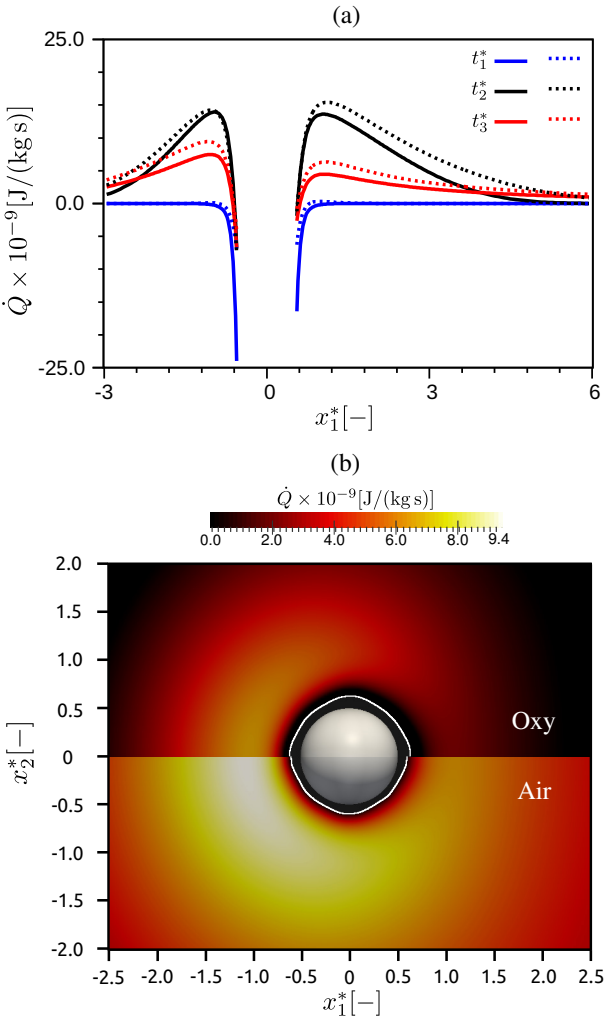

Figure 2.13: Gas phase heat release $\dot{Q}$: (a) evolution along centerline and (b) 2-D distribution at t_3^* in a region around the particle for both oxy- (solid line) and air (dashed line) atmospheres with $Re_{\mathrm{rel}} = 1$ and $X_{\mathrm{O_2}}^0 = 0.3$. In (b), $\dot{Q}$ is negative in the region between the white line and the particle surface.

energy sink in the vicinity of the particle. From t_1^* to t_2^*, the rates of the exothermic reactions (with $\dot{Q} > 0$) are increasing along with the transport of CO from the particle interface to the gas phase. At t_2^*, $\dot{Q}$ reaches its maximum value in the vicinity of the particle, where reaction

$$\mathrm{CO} + \mathrm{OH} \rightarrow \mathrm{CO_2} + \mathrm{H}\,, \tag{2.33}$$

has the highest rate. From t_2^* to t_3^*, $\dot{Q}$ is decreasing again, while the chemical reactions are approaching equilibrium.
A comparison between the air and oxy-atmospheres in Fig. 2.13a indicates that at t_1^*, the highest energy sink occurs in oxy-atmosphere due to increased activity of the endothermic reactions. Furthermore, Fig. 2.13a shows that at t_2^* and t_3^*, $\dot{Q}$ in the oxy-atmosphere is lower than in air. The lower $\dot{Q}$ in oxy-atmosphere results from the lower $\overline{\dot{m}}_\mathrm{C}$ (see Fig. 2.9), which represents the rate of production of CO on the surface that is released as a combustible fuel to the gas phase. Within phase II and III, not only $\dot{Q}$, but also the gas phase temperature, T_g, is lower for the oxy-atmosphere (see Fig. 2.7). Finally, the lower T_g in the oxy-atmosphere can be explained by the combination of its lower $\dot{Q}$ and higher $c_{p,g}$ values.

2.3.2 Transport and chemistry interactions

While the flow passes through the reactive region in the vicinity of the particle, the gas temperature is constantly increasing. Therefore, the gas phase temperature downstream ($x_1^* > 0.5$) is higher than upstream ($x_1^* < -0.5$), as is observed in Fig. 2.7a. Consequently, the temperature at the solid-gas interface increases when varying the central angle α from π to 0, where the latter denotes the downstream location.

In contrast to temperature, $C_{\mathrm{O_2}}$ decreases in flow direction, because of the $\mathrm{O_2}$ consumption by both surface oxidation and homogeneous reactions. This is evidenced in Fig. 2.8, the upstream side of the particle ($\alpha = \pi$) is shown to have a higher $C_{\mathrm{O_2}}$ value than the downstream side ($\alpha = 0$).
Both parameters, T and $C_{\mathrm{O_2}}$ affect $\dot{m}_\mathrm{C}$ at the interface. At $\alpha = \pi$, the influence of $C_{\mathrm{O_2}}$ is dominant in enforcing the highest $\dot{m}_\mathrm{C}$. From this point on, $\dot{m}_\mathrm{C}$ decreases in flow direction (see Fig. 2.8), at least for phase III, where substantial heat release and oxygen consumption has occurred.

Furthermore, the non-uniform $\dot{Q}$ distribution in Fig. 2.13b exhibits an increased value on the upstream side of the particle compared to the downstream region. The amount of $\dot{Q}$ depends on $\dot{m}_\mathrm{C}$, $C_{\mathrm{O_2}}$, and T_g. Within the upstream

region, the higher values of $\dot{m}_C$ and C_{O_2} compensate for the impact of the lower temperature. As a result, higher $\dot{Q}$ values are observed upstream compared to the downstream region. It is concluded that the upstream region is the most active region for both heterogeneous and homogeneous reactions.

2.3.2.1 Damköhler numbers

The non-uniform distribution of the aforementioned quantities at the interface and in the gas phase are caused by the relative gas flow with respect to the particle and its interaction with chemistry. To quantify the interactions between flow field and chemistry, diffusive and convective Damköhler numbers, Da_{conv} and Da_{diff}, are evaluated. The Damköhler number demonstrates which phenomenon, either transport or chemistry, is faster. Convective and diffusive Damköhler numbers are defined as $Da_{conv} = \tau_{conv}/\tau_{chem}$ and $Da_{diff} = \tau_{diff}/\tau_{chem}$, respectively. τ_{conv} and τ_{diff} refer to the characteristic times for convection and diffusion, which are computed as $\tau_{conv} = D_p/U_1^0$ and $\tau_{diff} = D_p^2/d_i$. τ_{chem} is the characteristic time for chemistry and defined as the time scale of a dynamically important reaction r with rate R_r. To calculate τ_{chem}, Eq. (2.31) is considered because of its important contribution to O_2 consumption. τ_{chem} is then computed as $\tau_{chem} = C_H/R_{32}$. Figure 2.14 shows for both atmospheres that the Damköhler numbers decrease towards the surface of the particle, $Da_{conv} > 1$ and $Da_{diff} > 1$, meaning that the relevant chemistry is faster compared with transport. Thus, CO oxidation and the flame chemistry are controlled by transport rather than by chemistry.

2.3.2.2 Re_{rel} variation approach

To accelerate oxygen convective transport within the reaction zone, τ_{conv} can be decreased by varying either D_p, U_1^0, or both. Therefore, to investigate the sensitivity of the convection process within the reaction zone to these parameters, a study varying Re_{rel} is carried out in the following by changing either the relative velocity or the particle diameter.

The oxy-atmosphere case presented in subsection 2.3.1 is selected as a reference defining reference particle diameter D_{ref}, relative velocity U_{ref}, Reynolds number Re_{ref}, characteristic time for convection and diffusion $\tau_{c,ref}$ and $\tau_{d,ref}$, and corresponding Damköhler numbers $Da_{c,ref}$ and $Da_{d,ref}$. Table 2.3 shows the four defined cases normalized with the reference case. In case i and ii, τ_{conv} decreases by downsizing the particle, whereas in case iii and iv, τ_{conv} is

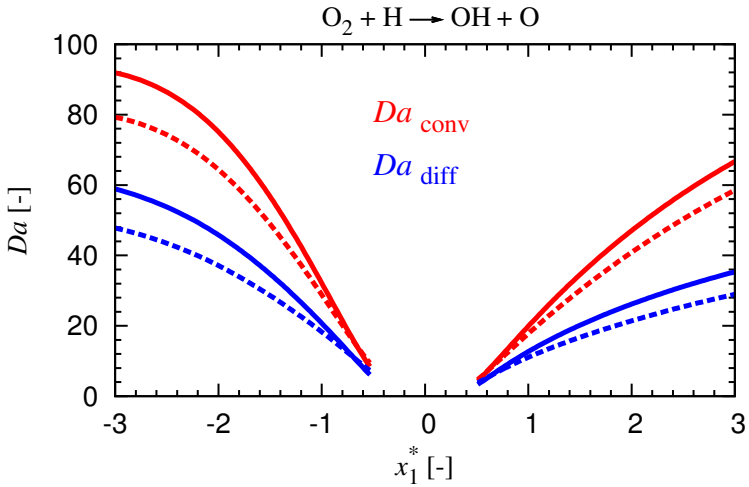

Figure 2.14: *Da* distribution around the particle at t_3^* for the oxy- (solid line) and air (dashed line) atmospheres.

Test case	$\frac{\tau_{\text{conv}}}{\tau_{\text{c,ref}}}$	$\frac{\tau_{\text{diff}}}{\tau_{\text{d,ref}}}$	$\frac{D_p}{D_{\text{ref}}}$	$\frac{U_1^0}{U_{\text{ref}}}$	$\frac{Re_{\text{rel}}}{Re_{\text{ref}}}$	$\frac{Da_{\text{conv}}}{Da_{\text{c,ref}}}$	$\frac{Da_{\text{diff}}}{Da_{\text{d,ref}}}$
i	2	4	2	1	2	2	4
ii	0.5	0.25	0.5	1	0.5	0.5	0.25
iii	2	1	1	0.5	0.5	2	1
iv	0.5	1	1	2	2	0.5	1

Table 2.3: Test cases with different Re_{rel} by varying U_1 and D_p.

decreased by increasing the relative velocity. Each of the four cases is tested at three different oxy-atmospheres with oxygen mole fractions of $X_{\text{O}_2}^0 = 0.24$, 0.3, and 0.36. The two τ_{conv} variation approaches are compared based on the results for the four cases given in Tab. 2.3. Figure 2.15a shows the temperature distributions of cases i and ii. The combustion of the larger particle in case ii with higher Re_{rel} yields a more stretched flame structure compared to case i. Analysis of the data shows that the volume-averaged gas phase temperature in case i is higher than in case ii. Particle downsizing reduces both τ_{conv} and τ_{diff}. Thus, species transport is faster in case i compared with case ii. Further, it can be observed from Fig. 2.15b that case iv with a faster gas flow and higher Re_{rel} exhibits a more stretched flame but lower temperatures than

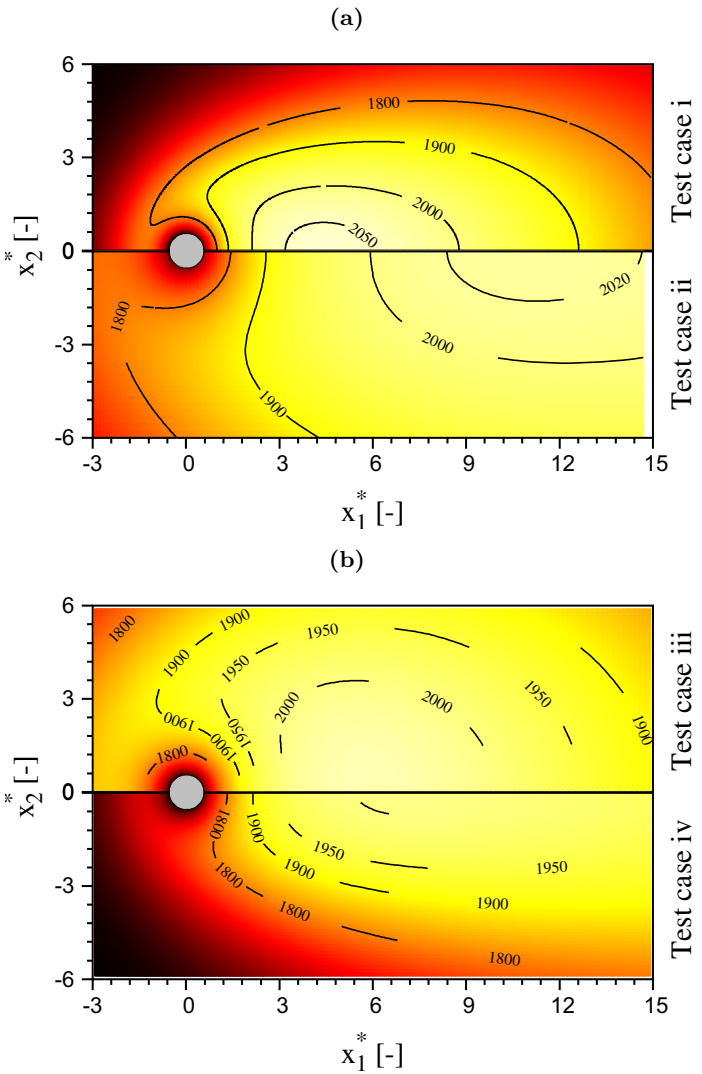

Figure 2.15: Distribution of T_g [K] around the particle at t_3^* with $X_{O_2}^0 = 0.3$ for test cases defined in Tab. 2.3.

case iii. Due to the lower τ_{conv}, species transport in case iv is faster than in case iii. Both temperature and species transport affect the total heat released from the char particle combustion.

Figure 2.16 shows the normalized mean of the heat release $\overline{\dot{Q}}/\overline{\dot{Q}}_{\mathrm{ref}}$ for each case at three different oxygen concentrations. Irrespective of the gas composition, decreasing τ_{conv}, either by varying particle size (from case i to ii) or relative velocity (from case iii to iv), yields higher heat release. The increase in heat release becomes more pronounced by decreasing particle size. The reason originates in the presence of higher temperature and faster oxygen transport around a smaller particle. In fact, the smaller particle possesses the lowest Da_{conv} and Da_{diff}.

It is concluded that decreasing τ_{conv} by reducing the particle size enhances both temperature and oxygen supply and thus, leads to higher heat release. Decreasing τ_{conv} by increasing relative velocity enforces faster oxygen supply for both surface and homogeneous reactions while decreasing temperature. Therefore, in a next step, Re_{rel} is varied in a wide range using different relative velocities to investigate the competing impacts of temperature and oxygen supply on total heat release.

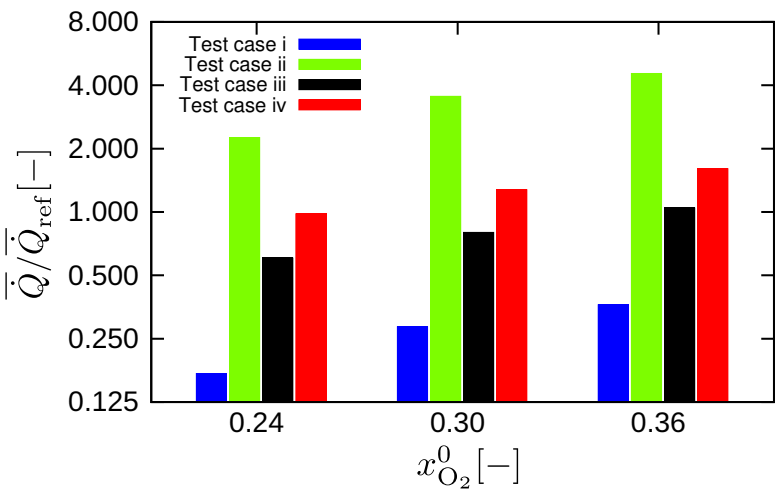

Figure 2.16: Variation of $\overline{\dot{Q}}/\overline{\dot{Q}}_{\mathrm{ref}}$ versus $X^0_{\mathrm{O}_2}$ for the test cases defined in Tab. 2.3.

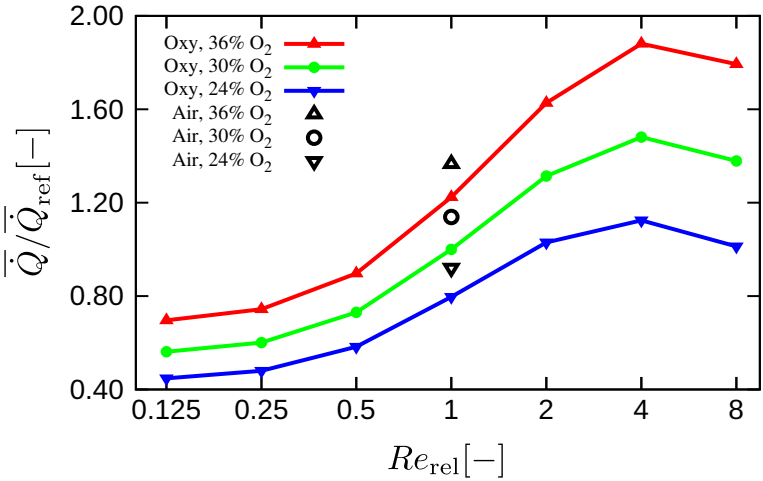

Figure 2.17: Variation of $\overline{\dot{Q}}/\overline{\dot{Q}}_{\mathrm{ref}}$ versus Re_{rel} (varied by U_1^0) at t_3^* with $X_{\mathrm{O_2}}^0 = 0.24$, 0.30, and 0.36 in the oxy- and air atmospheres at $Re_{\mathrm{rel}} = 1$.

2.3.2.3 Re_{rel} variation by relative velocity

Here, Re_{rel} is varied from 0.125 to 8 by changing the relative velocity, while keeping the particle diameter constant. Each variation is done for three different oxy-atmospheres with $X_{\mathrm{O_2}}^0 = 0.24$, 0.3, and 0.36.

The normalized heat release $\overline{\dot{Q}}/\overline{\dot{Q}}_{\mathrm{ref}}$ over Re_{rel} is shown in Fig. 2.17. In all studied oxy-atmospheres, $\overline{\dot{Q}}/\overline{\dot{Q}}_{\mathrm{ref}}$ increases with increasing Re_{rel} from 0.125 to 4, before it decreases at $Re_{\mathrm{rel}} = 8$. As discussed in section 4.1, the heat release from the homogeneous reactions mainly depends on the amount of the oxygen in the atmosphere, the CO released due to surface reactions, and the temperature. Therefore, to understand the reasons for the $\overline{\dot{Q}}/\overline{\dot{Q}}_{\mathrm{ref}}$ variation over Re_{rel}, the impact of the flow field on the aforementioned parameters is discussed in the following.

Increasing Re_{rel} leads to a faster oxygen transport for both heterogeneous and homogeneous reactions. The mean gas phase temperature, $\overline{T}_g$ normalized by $\overline{T}_{g,\mathrm{ref}}$ is shown in Fig. 2.18a. In all investigated cases, the normalized mean gas phase temperature decreases with increasing Re_{rel}. This decrease is more pronounced at higher Re_{rel}. In fact, increasing Re_{rel} with relative flow

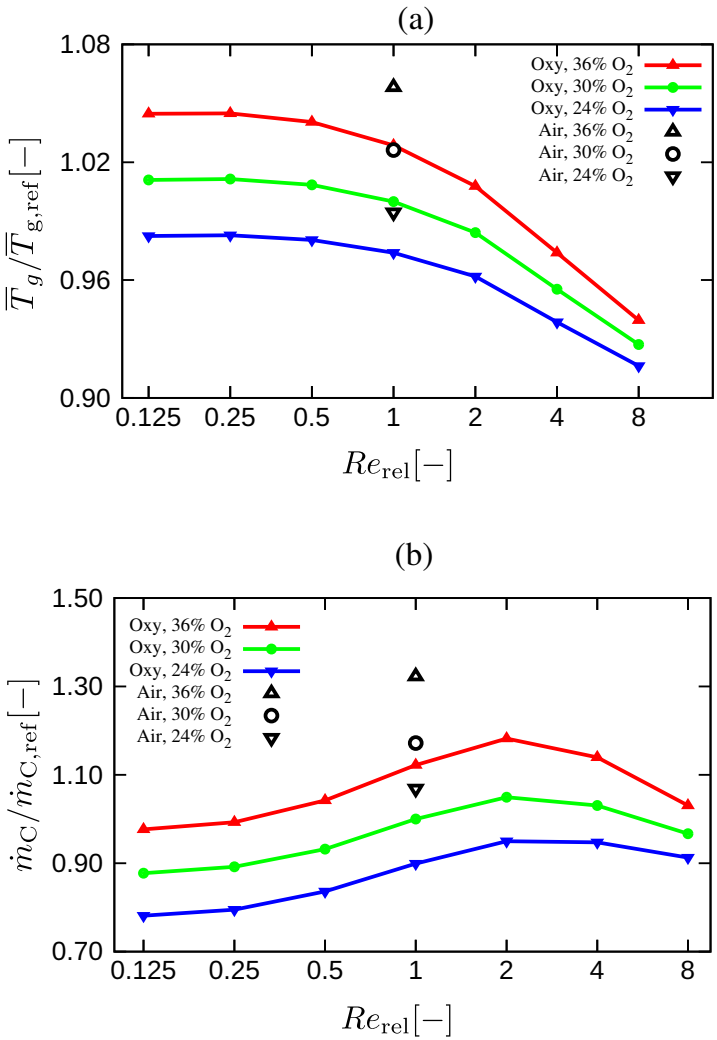

Figure 2.18: Variation of $\overline{T}_g/\overline{T}_{g,\mathrm{ref}}$ (a) and $\overline{\dot{m}}_C/\overline{\dot{m}}_{C,\mathrm{ref}}$ (b) over Re_{rel} (varied by U_1^0) at t_3^* with $X_{O_2}^0 = 0.24$, 0.30, and 0.36 in the oxy- and air atmospheres at $Re_{\mathrm{rel}} = 1$.

velocity enforces a faster gas stream, which transitions the combustion zone faster. Consequently less heat is absorbed by the gas flow compared to cases with lower relative flow velocity.

Figure 2.18b shows for each gas composition that $\overline{\dot{m}}_C/\overline{\dot{m}}_{C,ref}$ first increases with increasing Re_{rel} and then decreases at $Re_{rel} = 2$. $\overline{\dot{m}}_C$ represents the mean CO production rate and is a function of the oxygen concentration and the temperature. It was discussed that increasing Re_{rel} enhances the oxygen transport to the combustion zone, while $\overline{T}_g$ reduces. Based on these results, it is concluded that from $Re_{rel} = 0.125$ to 2, the higher oxygen concentration compensates the temperature drop and thus $\overline{\dot{m}}_C/\overline{\dot{m}}_{C,ref}$ increases. When Re_{rel} increases from 2 to 8, the Da_{conv} is low enough to cause a competition between chemistry and transport. This leads to a significant decrease in temperature, and consequently $\overline{\dot{m}}_C/\overline{\dot{m}}_{C,ref}$ decreases. Comparing the $\overline{\dot{m}}_C/\overline{\dot{m}}_{C,ref}$ variation over Re_{rel} for each gas composition shows that at higher oxygen concentrations, the impact of the flow on the CO production rate is enhanced.

2.3.3 Char combustion in array configuration

An industrial furnace contains millions of burning coal particles interacting with the surrounding gas flow and their neighboring particles. Therefore, in addition to the single particle, char combustion has also been investigated in an array configuration using the particle resolved approach. To discuss the interaction between the gas flow and the array combustion, a few cases from [108] are presented here. In these cases, the particle spacing L is varied from $3D_p$ to $9D_p$ and the relative Reynolds number Re_{rel} from 1 to 8. Similar to the single particle simulations, the particle array configuration has inlet-outlet boundaries in the streamwise direction. However, the particle array configuration is periodic in the spanwise direction to reduce the computational effort. All particles have a diameter of 100 μm and their initial temperature is the same as the initial gas temperature of 1500 K. In all cases, the gas phase burns under oxy-fuel condition with the same composition as Oxy defined in Tab. 2.2.

A reference case is defined by three particles in streamwise direction, with $6D_p$ particle spacing and a relative Reynolds number of 1. Figure 2.19 shows the distribution of the heat release rate, temperature, OH, and O_2 mass fractions in the vicinity of the particles for the reference case. The first particle (from the left side) upstream, behaves similar to a single particle, while downstream particles behave very differently. All quantities are non-uniformly distributed around particles. The peak of the heat release rate is upstream of the first

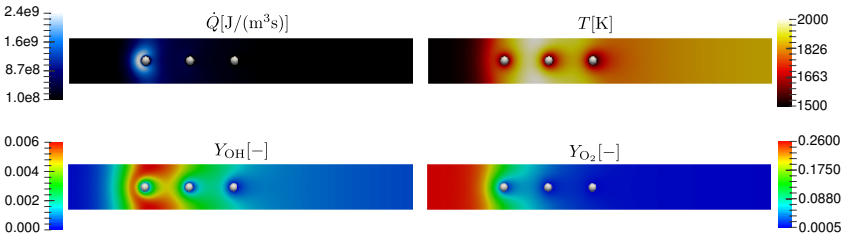

Figure 2.19: Distribution of the heat release rate, temperature, and OH and oxygen mass fractions in the vicinity of the particles with $6D_p$ spacing at $Re_{\mathrm{rel}} = 1$.

particle, while the peak of the gas temperature is further downstream. Besides the heat release rate, OH and O_2 distributions reveal substantially higher values around the first particle. The non-uniform distribution of the quantities originates from the gas flow, which continuously supplies oxygen for the first particle. The higher O_2 concentration leads to faster oxidation on the surface of the first particle. As a result of the faster surface oxidation rate together with the higher oxygen concentration, the vicinity of the first particle becomes the most active region for exothermic gaseous reactions and yields the highest heat release values.

The influence of the relative flow on the particle combustion is further investigated by considering cases at $Re_{\mathrm{rel}} = 1$ and 8 for different configurations with particle spacing of $3D_p$, $6D_p$, and $9D_p$. Figure. 2.20 shows the distribution of the heat release rate and temperature for these cases. For each configuration with a specific particle spacing, increasing Re_{rel} changes the particle combustion differently depending on the particle location in the array. For the first particle upstream, varying Re_{rel} has a non-linear impact on the heat release rate. For the first particle, increasing Re_{rel} accelerates the burning rate only up to a certain point, beyond which increasing Re_{rel} even decreases the burning rate. For the second and third particles however, increasing Re_{rel} up to 8 monotonously increases the burning rate.

Figure. 2.20 further shows that increasing Re_{rel} expands the flame front and forms a different flame structure around particles. For each particle spacing, increasing Re_{rel} shifts the temperature peak further downstream towards the outlet. In the array with $9D_p$ particle spacing, increasing Re_{rel} shifts combustion of each array particle towards the single particle regime. However, in a denser array with $3D_p$ particle spacing, increasing Re_{rel} leads to particle group combustion, where particles are burning in the flame of the neighboring

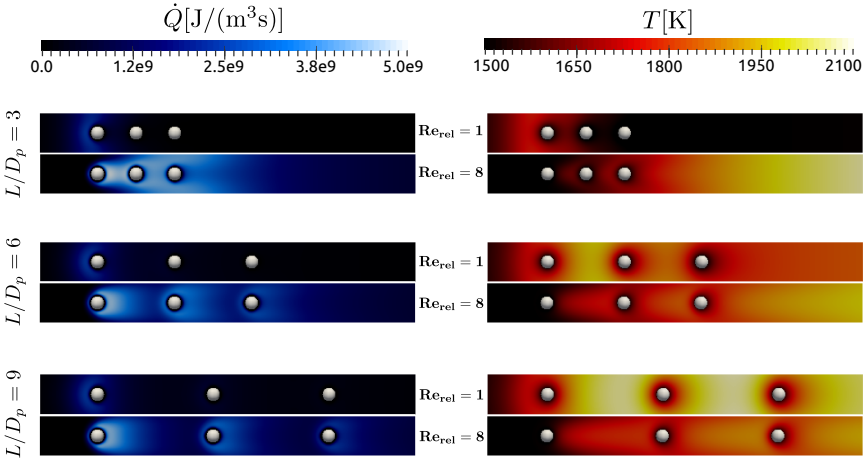

Figure 2.20: Distribution of the heat release rate and gas temperature around the particles for different array configurations (particle spacing $L = 3D_p$, $6D_p$, and $9D_p$) with $Re_{\mathrm{rel}} = 1$ and 8.

particles and particle interactions can intensify combustion rates. This could be explained with the presence of both higher temperatures in the denser particle cloud and faster oxygen supply at the higher Re_{rel}. Further parametric studies are discussed and analyzed to incorporate the particle interaction into the model development for point particle simulations in [108].

2.3.4 Drag force acting on the reactive particle

A char particle in a hot atmosphere undergoes heterogeneous reactions on the surface. There exists a two-way coupling between the gas flow around the particle and the surface reactions. The presence of a gas flow around the particle affects the temperature and oxygen concentration on the surface, which in turn influences the heterogeneous reactions. These reactions, on the other hand, result in a Stefan flow on the particle surface, impacting the dynamics of the surrounding gas. This Stefan flow velocity shifts the stagnation point away from the particle surface, altering the flow pattern in comparison with the non-reactive particle, and resulting in a modified drag force. Therefore, this study provides the correlation between the computed drag coefficient of the reactive particle and the dimensionless Stefan flow velocity.

$X_{O_2,ref}$	$X_{CO_2,ref}$	$X_{H_2O,ref}$	T_{ref} [K]	D_{ref} [μm]	U_{ref} [m/s]	Re_{ref}	$\tau_{c,ref}$ [μs]
0.3	0.53	0.17	1500	100	2	1	50

Table 2.4: Reference parameters and their corresponding values

Test case	$\frac{\tau_{conv}}{\tau_{c,ref}}$	$\frac{D_p}{D_{ref}}$	$\frac{U_1}{U_{ref}}$	$\frac{Re_{rel}}{Re_{ref}}$
a	1	1	1	1
b	1/2	1	2	2
c	1/4	1	4	4
d	1/8	1	8	8

Table 2.5: Case studies at different Re_{rel} and τ_{conv} by varying U_1^0.

Reference quantities needed for the envisioned parameter study are defined in Tab. 2.4. The reference density and viscosity are computed at the reference gas composition and temperature. The reference Reynolds number is defined by the reference density, viscosity, velocity, and the particle diameter. The reference time is defined based on the characteristic convection time scale, which is 1-2 orders of magnitude (depending on the reaction rates) higher than the characteristic time of the gaseous chemical reactions. In previous sections, it was shown that the oxygen molar fraction and the particle relative velocity have the significant impact on the combustion behavior. Here, simulation results are analyzed at various X_{O_2} and U_1 to investigate the variation of the drag force. Varying X_{O_2} with respect to its reference value, yields three simulation sets corresponding to $X_{O_2} = 0.24$, 0.3, and 0.36, respectively. This interval was chosen for oxygen concentration, which is close to the required amount of oxygen in oxy-atmosphere to get the same adiabatic temperature as in air environment. Keeping X_{H_2O} the same as its reference value in each simulation set, X_{CO_2} is varied to compensate for the variation in X_{O_2}. Each simulation set includes four case studies; a, b, c, and d, which are defined in Tab. 2.5. In cases a to d, Re_{rel} is increased by increasing U_1 and keeping D_p constant. As Re_{rel} increases, the characteristic time scale for convection, $t_{conv} = D_p/U_1$, however, decreases. In each case study, the results are computed up to $t = 60\tau_{c,ref}$.

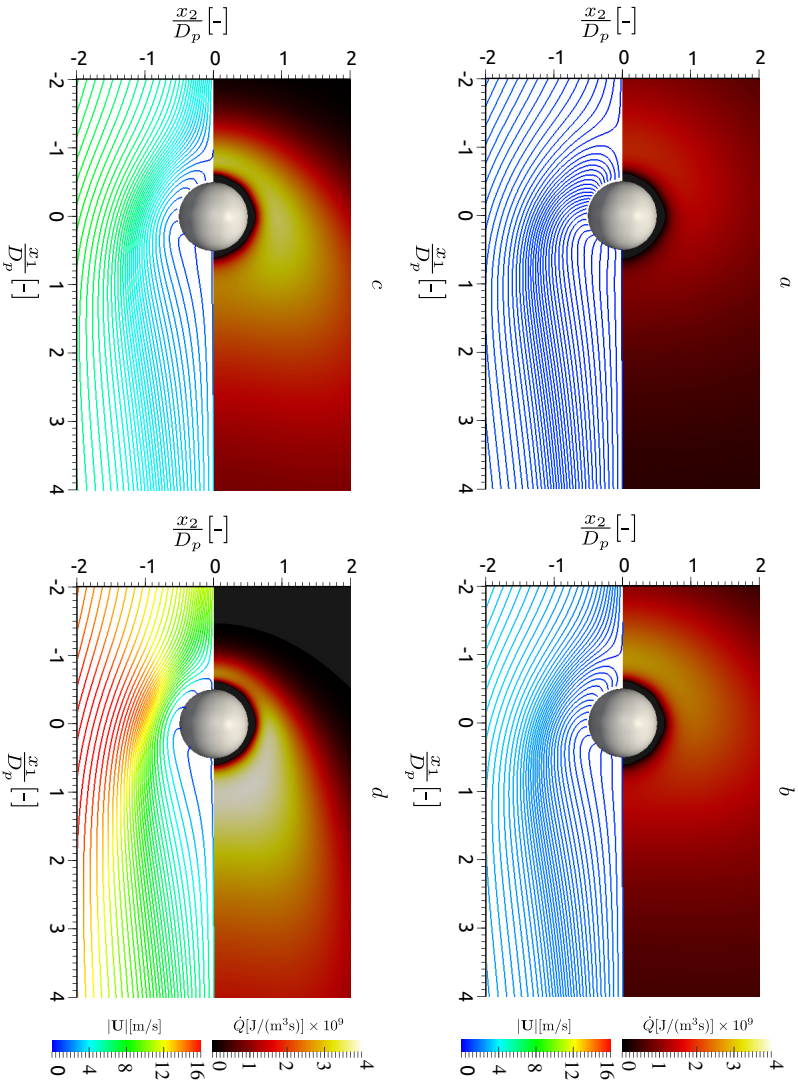

Figure 2.21: Distribution of $\dot{Q}$ (upper) and streamlines (lower) for case studies a-d (defined in Tab. 2.5) with $X_{O_2} = 0.30$ at $t = 60\tau_{c,ref}$.

2.3.4.1 Surface reaction effects on the flow field

Figure 2.21 shows the heat release from homogeneous reactions, $\dot{Q}$ together with the streamline distribution around the particle, with $X_{O_2} = 0.30$ at $t = 60\tau_{c,ref}$. Comparing heat release distributions of cases a-d suggests that increasing the relative velocity results in a more stretched flame around the particle. The increase in relative velocity enhances the heat release peak and shifts its location further downstream. The perpendicular streamlines on the particle surface, shown in Fig. 2.21, support the presence of the Stefan flow velocity. The stagnation point locates farther from the particle surface in the cases with lower relative velocity or slower forced convection. The location of the stagnation point in such flows depends on both U_1 and U_{St}. Thus, the ratio of U_{St} to U_1 is more suitable in investigating the impact of the Stefan flow velocity on the flow field. The magnitude of U_{St} depends on the heterogeneous reactions, amongst which the surface oxidation reaction $C + 1/2O_2 \rightarrow 2CO$ has more than 95% contribution in carbon consumption rate and consequently in the Stefan flow velocity magnitude. The value of U_{St}/U_1 distributes non-uniformly around the particle surface, decreasing from upstream to downstream. The reason originates in the higher oxygen concentration and consequently higher activity of the surface oxidation reaction, at the upstream region.

For further investigation, $\overline{U}_{St}/U_1$ is considered, where $\overline{U}_{St}$ refers to the averaged value of the Stefan velocity on the particle surface. Although, after $t = 20\tau_{c,ref}$ the maximum temperature in the gas phase approaches a constant value, surface temperature increases linearly over time. The increase in surface temperature raises surface reaction rates and consequently $\overline{U}_{St}/U_1$. To analyze the data, three different times are considered, $t_1 = 20\tau_{c,ref}$, $t_2 = 40\tau_{c,ref}$, and $t_3 = 60\tau_{c,ref}$ for each case study. Figure 2.22a shows the variation of $\overline{U}_{St}/U_1$ for each simulation set with respect to Re_{rel}. As Re_{rel} decreases, $\overline{U}_{St}/U_1$ increases. Therefore, at lower Re_{rel}, Stefan velocity impacts the flow pattern more and moves the stagnation point farther from the particle surface. Furthermore, it can be observed from Fig. 2.22a, that at each Re_{rel}, a higher oxygen concentration yields a higher U_{St}. This can be explained by the fact that the higher oxygen concentration accelerates the oxidation reaction and consequently increases the Stefan flow velocity.

The drag force on the particle defined in Eq. 2.27 can be written as

$$C_D = \frac{\int_A \{-\frac{\dot{m}^2}{\rho} n_\alpha + \tau_{\alpha\beta} \cdot n_\beta\} \cdot n_\alpha dA}{\frac{1}{2}\rho_g U_1^2 A_2}, \tag{2.34}$$

where $\dot{m}^2/\rho dA$ is the thrust force due to the surface reactions and the remaining term in the numerator is the viscous force. In Eq. 2.34, the impact of the pressure term is neglected due to the low-Mach assumption applied in the simulations.

The ratio of the drag coefficient of the reactive case to the non-reactive set-up

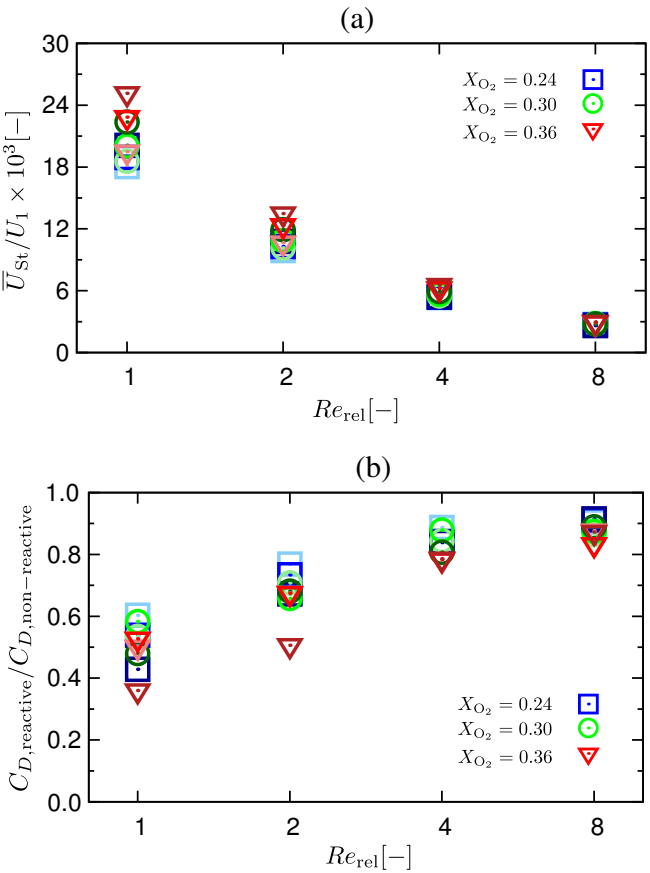

Figure 2.22: (a) Ratio of Stefan velocity to initial relative flow velocity; (b) drag coefficient ratio of reactive to non-reactive particle at various Re_{rel} and gas composition. For each gas composition, the symbols with the light, intermediate, and dark color refer to t_1, t_2, and t_3, respectively.

is plotted in Fig. 2.22b for varying Re_{rel}. This figure shows that this ratio remains less than one for each gas composition. This observation implies that a lower drag force acts on the surface of the reactive with the non-reactive particle. Since the thrust force is negligible compared to the viscous forces on the surface, the reduction in the drag force can be attributed to the lower strain rate. Combustion affects the drag coefficient more at lower Re_{rel}. In other words, particle combustion reduces the drag force more at the lower Re_{rel} and higher t_{conv}. Furthermore, Fig. 3b illustrates that at $Re_{\mathrm{rel}} < 2$, the drag force oscillates over time. However, considering an average value indicates that independent of Re_{rel}, the lower drag force belongs to the particle in a higher oxygen content.

Figure 2.23 shows drag reduction profile versus $\overline{U}_{\mathrm{St}}/U_1$ at $t = 20\tau_{\mathrm{c,ref}}$, $40\tau_{\mathrm{c,ref}}$, and , $60\tau_{\mathrm{c,ref}}$ for each case study. The higher $\overline{U}_{\mathrm{St}}/U_1$ intensifies the impact of reactions on the fluid flow and yields a lower drag coefficient.

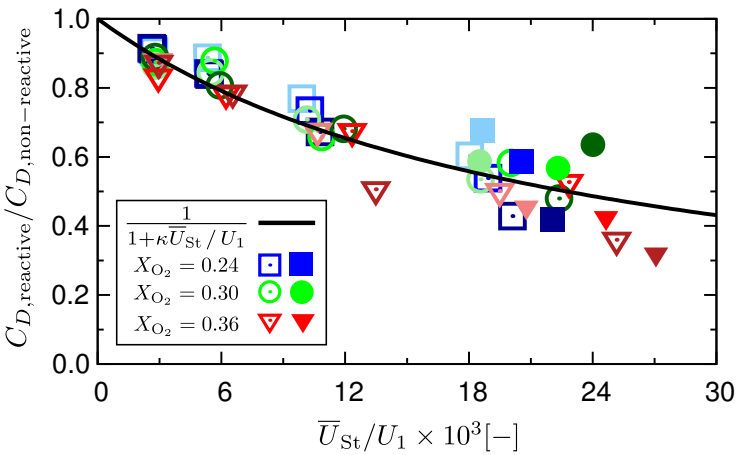

Figure 2.23: Drag coefficient reduction for reactive particle at various ratios of Stefan flow velocity to the inlet velocity. The corresponding correlation function is shown as solid line. For each gas composition, the symbols with the light, intermediate, and dark color refer to the t_1, t_2, and t_3, respectively. The blank symbols represent oxy-atmosphere and the filled symbols refer to the char combustion under air atmosphere.

2.3.4.2 Drag force correlation

It is anticipated that $C_{D,\text{reactive}}/C_{D,\text{non-reactive}}$ can be correlated with $\overline{U}_{\text{St}}/U_1$ by a reciprocal function. To support this prediction, first an empirical relation for the drag reduction of the evaporating droplet is considered. Renksizbulut and Yuen [109] suggested that Stefan convection reduces the drag coefficient of the evaporating droplet by factor of $1/(1 + B_M)$, where B_M is the mass transfer number. It is assumed that $\overline{U}_{\text{St}}/U_1$ is proportional to this mass transfer number. Thus, $\kappa\overline{U}_{\text{St}}/U_1$ is chosen as the mass transfer number for the reactive case, where κ is the free parameter for curve fitting. Using this relation, the drag reduction factor becomes 1 and 0 in the limits of very small and very high $\overline{U}_{\text{St}}/U_1$, respectively. Using least-squares method, $\kappa = 43.97 \pm 1.79$ results in a curve with minimum distance from the scatter data points. Furthermore, Fig. 2.23 includes some results for char combustion under air atmosphere with lower and various oxygen concentrations. The drag reduction of char combustion in air environment follows the extracted correlation in oxy-atmosphere. Data analysis shows that oxidation reaction has more than 95% contribution in carbon consumption rate and consequently, the magnitude of Stefan flow. Therefore, with the current surface kinetics, gasification reactions have minor impact on the Stefan flow and drag modification.

Char combustion processes might happen in three different regimes; either kinetic controlled, diffusion controlled or kinetic-diffusion controlled. Depending on the size of the particle, char combustion turns to the kinetically controlled process under low temperature and high oxidizer concentration conditions. In the current study, due to the presence of high initial temperature and low oxidizer at the particle surface, char combustion shifts towards the diffusion controlled regime. Particle porosity has also critical impact on char combustion regime specification. In the current work, coal type with certain porosity has been considered. To generate a model that covers the whole char combustion regimes, further investigations are required to study the correlation between Stefan flow velocity and drag coefficient at various particle size, porosity, temperature, and oxidizer concentration.

3 Ignition of coal particles with an Euler-Lagrange approach

In this chapter, devolatilization and ignition of coal particles in both air and oxy-atmosphere are investigated by using Euler-Lagrange method. The governing equations and numerical methods for both particle and gas phase within the Euler-Lagrange framework are described. The details about the sub-models and the interphase coupling approach are provided. The simulation results are validated against experimental measurements of ignition delay time of coal particles in a laminar entrained flow reactor by Liu et al. [47]. Using the validated model, two configurations are investigated; first, a single particle and second, a group particle configuration. For the single particle configuration, the coal ignition process is computed at various particle sizes and gas temperatures in both air and oxy-atmosphere. For both atmospheres, detailed discussions regarding devolatilization and volatile flame evolution are provided. Coal ignition in oxy-atmosphere is compared with the conventional condition for a large set of parameters and the primary effect of the delayed ignition in oxy-atmosphere is discussed. In the group particle configuration, the impact of particle number density, gas temperature, and slip velocity on the ignition delay time is investigated and discussed in detail.

3.1 Models and numerical methods

Coal combustion involves mass, momentum, and energy transfer between the coal particles and the gas phase. In the present work, the two-phase interaction is modeled using an Euler-Lagrange approach. Gas phase equations are given in the Eulerian framework, while particle equations are in the Lagrangian framework. The Eulerian and the Lagrangian equations are fully coupled. The performance of the models and methods has been extensively validated against experimentally measured ignition delay time data by Liu et al. [47]. The corresponding model equations are given in the following sections.

3.1.1 Gas phase

The gas phase is described in the Eulerian formulation. The governing equations for the gas phase are similar to those applied by Attili et al. [110]. The gas phase equations include source terms due to the coupling with the particles similar to those employed by Sirignano [111], Bai et al. [87], and Rieth et al. [82]. The balance of mass, species, momentum, and energy leads to the following equations:

$$\frac{\partial \rho_g}{\partial t} + \frac{\partial}{\partial x_\beta}\left(\rho_g U_{g,\beta}\right) = \dot{S}_m, \tag{3.1}$$

$$\frac{\partial \rho_g Y_i}{\partial t} + \frac{\partial}{\partial x_\beta}\left(\rho_g \left(U_{g,\beta} + V_{\beta,i}\right) Y_i\right) = M_i + \dot{S}_{Y_i}, \tag{3.2}$$

$$\frac{\partial \rho_g U_{g,\alpha}}{\partial t} + \frac{\partial}{\partial x_\beta}\left(\rho_g U_{g,\alpha} U_{g,\beta}\right) = -\frac{\partial \Pi}{\partial x_\alpha} + \frac{\partial \tau_{\alpha\beta}}{\partial x_\beta} + \dot{S}_{U,\alpha}, \tag{3.3}$$

$$\begin{aligned} C_{p,g}\frac{\partial \rho_g T_g}{\partial t} + C_{p,g}\frac{\partial}{\partial x_\beta}\left(\rho_g U_{g,\beta} T_g\right) = &-\rho_g \frac{\partial T_g}{\partial x_\beta}\sum_i^n C_{p,g,i} Y_i V_{\beta,i} \\ &+ \frac{\partial}{\partial x_\beta}\left(\lambda_g \frac{\partial T_g}{\partial x_\beta}\right) + Q_g + \dot{S}_T. \end{aligned} \tag{3.4}$$

Here, ρ_g is the density of the gas phase, $U_{g,\beta}$ the gas velocity in β direction, and $\dot{S}_m$ the rate of mass released from particles. For the i^{th} species in the gas phase, Y_i is the mass fraction and $V_{\beta,i}$ the diffusion velocity in β direction, which is calculated from the Curtiss-Hirschfelder approximation [112]. M_i is the species production rate due to chemical reactions in the gas phase, while $\dot{S}_{Y_i}$ accounts for the production rate of the i^{th} species due to the release of vapor and volatiles from particles. $\tau_{\alpha\beta}$ is the viscous stress tensor and $\dot{S}_{u,\alpha}$ refers to the momentum source term in the α direction originating from particle motion. Π is the pressure that enforces mass conservation through the Poisson equation within the low-Mach formulation [113] adopted in the present work. T_g is the gas temperature, λ_g the thermal conductivity, $C_{p,g}$ the specific heat of the gas phase at constant pressure. Q_g accounts for the rate of heat released from the homogeneous reactions in the gas phase and $\dot{S}_T$ refers to the rate of thermal energy exchange between the gas phase and coal particles. The physical models for $\dot{S}_m$, $\dot{S}_{Y_i}$, $\dot{S}_{U,\alpha}$, and $\dot{S}_T$ are described in section 3.1.3. Chemical reactions in the gas phase are modeled with finite rate chemistry adopting the GRI 3.0 mechanism [114].

3.1.2 Particle phase

3.1.2.1 Lagrangian equations

Coal is modeled as a collection of point particles within the Lagrangian framework. Particle equations are similar to those applied by Miller and Bellan [115] to model liquid droplet evaporation. The trajectory, velocity, mass, and temperature of each particle are computed from the following equations:

$$\frac{dx^k_{p,\alpha}}{dt} = U^k_{p,\alpha}, \tag{3.5}$$

$$\frac{dU^k_{p,\alpha}}{dt} = f^k_d \frac{18\mu_g \left(U_{g,\alpha} - U^k_{p,\alpha}\right)}{\rho_g (D^k_p)^2}, \tag{3.6}$$

$$\frac{dm^k_p}{dt} = \dot{m}^k_{p,e} + \dot{m}^k_{p,d}, \tag{3.7}$$

$$C^k_p m^k_p \frac{dT^k_p}{dt} = \dot{m}^k_{p,e}\Delta H_e + \dot{m}^k_{p,d}\Delta H_d + \Psi^k_{p,c} + \Psi^k_{p,r}, \tag{3.8}$$

where for the k^{th} particle, m^k_p is the total particle mass and D^k_p its diameter. $x^k_{p,\alpha}$ refers to the particle position and $U^k_{p,\alpha}$ to the velocity along the α direction. In Eq. (3.6), f^k_d is a correction coefficient which accounts for the effect of the Stefan flow on the drag force and is computed as:

$$f^k_d = \frac{1 + 0.0545 Re^k_s + 0.1(1 - 0.03 Re^k_s)\sqrt{Re^k_s}}{1 + \kappa_1 (Re^k_b)^{\kappa_2}}, \tag{3.9}$$

$$Re^k_s = \rho_g D^k_p \frac{\left|U_{g,\alpha} - U^k_{p,\alpha}\right|}{\mu_g}, \tag{3.10}$$

$$Re^k_b = \frac{1}{\pi D^k_p \mu_g} \left|\frac{dm^k_p}{dt}\right|, \tag{3.11}$$

$$\kappa_1 = 0.09 + 0.077 \exp(-0.4 Re^k_s), \tag{3.12}$$

$$\kappa_2 = 0.4 + 0.77 \exp(-0.04 Re^k_s), \tag{3.13}$$

where Re^k_s and Re^k_b refer to the slip and blowing Reynolds numbers, respectively. Equation (3.9) is an empirical correlation applied by Miller and Bellan [115] as a fit to the simulation results of Cliffe and Lever [116].

In Eq. (3.7), the particle mass is reduced due to the evaporation and devolatilization processes by $\dot{m}^k_{p,e}$ and $\dot{m}^k_{p,d}$, respectively. The applied models for

evaporation and devolatilization are explained in section 3.1.2.2 and 3.1.2.3.

In Eq. (3.8), the first and second term on the right hand side refer to the required energy for the evaporation and devolatilization processes. ΔH_e is the heat of evaporation and ΔH_d the heat of devolatilization. The term $\Psi^k_{p,c}$ accounts for the energy transfer by convection and conduction between the particle and the surrounding gas, while the term $\Psi^k_{p,r}$ accounts for the energy transfer due to radiation. These processes are treated similarly to those applied by Sirignano [111] and Bai et al. [87] as :

$$\Psi^k_{p,c} = A^k_p \frac{\lambda_g Nu}{D^k_p}(T_g - T_p)\left(\frac{B^k_h}{\exp(B^k_h) - 1}\right), \tag{3.14}$$

$$\Psi^k_{p,r} = A^k_p \sigma \epsilon_p \left(T^4_w - T^4_p\right), \tag{3.15}$$

where Nu is the Nusselt number computed by Ranz and Marshall [117, 118] as $Nu = 2 + 0.552 {Re^k_s}^{0.5} Pr^{0.333}$, with $Pr = 0.7$. A^k_p is the particle surface area and T_w is assumed to be 500 K, which is similar to the typical temperature of industrial burner walls. $\epsilon_p = 0.7$ and $\sigma = 5.6 \times 10^{-8}$ W/(m^{2}K^4) are the emissivity and the Stefan-Boltzmann constant, respectively. The heat transfer number B^k_h is computed as $B^k_h = C_g \dot{m}^k_p / (2\pi D^k_p \lambda_g)$.

3.1.2.2 Evaporation model

The evaporation rate of water, $\dot{m}^k_{p,e}$ is computed using a spherical water drop model as:

$$\dot{m}^k_{p,e} = \pi Sh D^k_p D_{\mathrm{H_2O}} \rho_g \left(\frac{x_{\mathrm{H_2O},s} - x_{\mathrm{H_2O},\infty}}{1 - x_{\mathrm{H_2O},s}}\right)\left(\frac{B^k_m}{\exp(B^k_m) - 1}\right), \tag{3.16}$$

$$B^k_m = \frac{\dot{m}^k_{p,e}}{2\pi D^k_p \rho_g D_{\mathrm{H_2O}}}, \tag{3.17}$$

where Sh is the Sherwood number computed by Ranz and Marshall [117, 118] as $Sh = 2 + 0.552 {Re^k_s}^{0.5} Sc^{0.333}$, with $Sc = 0.7$. $D_{\mathrm{H_2O}}$ refers to the diffusion coefficient of the water vapor. The mole fraction of water at the particle surface, $x_{\mathrm{H_2O},s}$ is computed as the ratio of the water vapor pressure to the total pressure $x_{\mathrm{H_2O},s} = P_{\mathrm{H_2O}}/P$, where P is the thermodynamic pressure and $P_{\mathrm{H_2O}}$ the Antoine pressure which is computed as $P_{\mathrm{H_2O}} = \exp\left(A - \frac{B}{T+C}\right)$, with $A = 18.3036$ mmHg, $B = 3816.44$ mmHg K, and $C = -46.13$ K [119].

For each particle, the particle diameter D_p remains constant in time, while

the particle density reduces due to mass loss caused by evaporation and devolatilization processes. A constant particle diameter is a reasonable assumption in the current study, as only devolatilization and ignition that happen during the early stage of coal combustion, are considered. This assumption is also consistent with the numerical studies performed by Goshayeshi and Sutherland [57] and Tufano et al. [58].

3.1.2.3 Devolatilization model

To compute the devolatilization rate $\dot{m}_{p,d}^{k}$ for each particle, the chemical percolation devolatilization (CPD) model [46] is applied. The CPD model describes the devolatilization phase according to the coal molecular structure. Figure 3.1 schematically shows the devolatilization process in the CPD model according to the molecular structure. The coal lattice contains aromatic rings connected by stable and labile bridges. One aromatic ring or a group of neighboring aromatic rings are referred to as node in the CPD model. Stable bridges mainly appear within the (so-called) infinite fragments of aromatic rings that continue from one side of the lattice to the other side. In the coal lattice, infinite fragments are referred to as char. The labile bridges can break by exposing the coal lattice to the external energy during devolatilization. Breaking of the labile bridges between side chains and aromatic rings results in the release of light gases. However, breaking of labile bridges between aromatic rings forms finite fragments. Finite fragments with lower molecular weight are vaporized as tar, while the heavier fragments remain in the lattice and form metaplast, which can be converted to char by a cross-linking process. As Fig. 3.1 shows, the CPD model computes the formation rate of the char, tar, and light gases inside the coal lattice. Therefore, the devolatilization rate of the k^{th} particle, $\dot{m}_{p,d}$, can then be computed by adding the formation rate of the tar and light gases.

Evolution of the coal lattice is used to describe the formation of light gases, tar, metaplast, and char from the parent coal. Figure 3.2 shows the chemical reaction pathway corresponding to the bridge breaking mechanism applied in the CPD model. The chemical reaction pathway begins by breaking a labile bridge $\mathcal{L}$ into a highly reactive intermediate bridge $\mathcal{L}^*$ with the reaction rate constant k_b. The intermediate bridge $\mathcal{L}^*$ can then be consumed by two further reactions. In the first reaction, with the rate k_δ, $\mathcal{L}^*$ is converted to two side chains that consequently form a first type of gaseous species g_1. In the second reaction, with the rate k_c, $\mathcal{L}^*$ forms a stable bridge in char structure and releases a second type of gaseous species g_2. Solving a system of ordinary

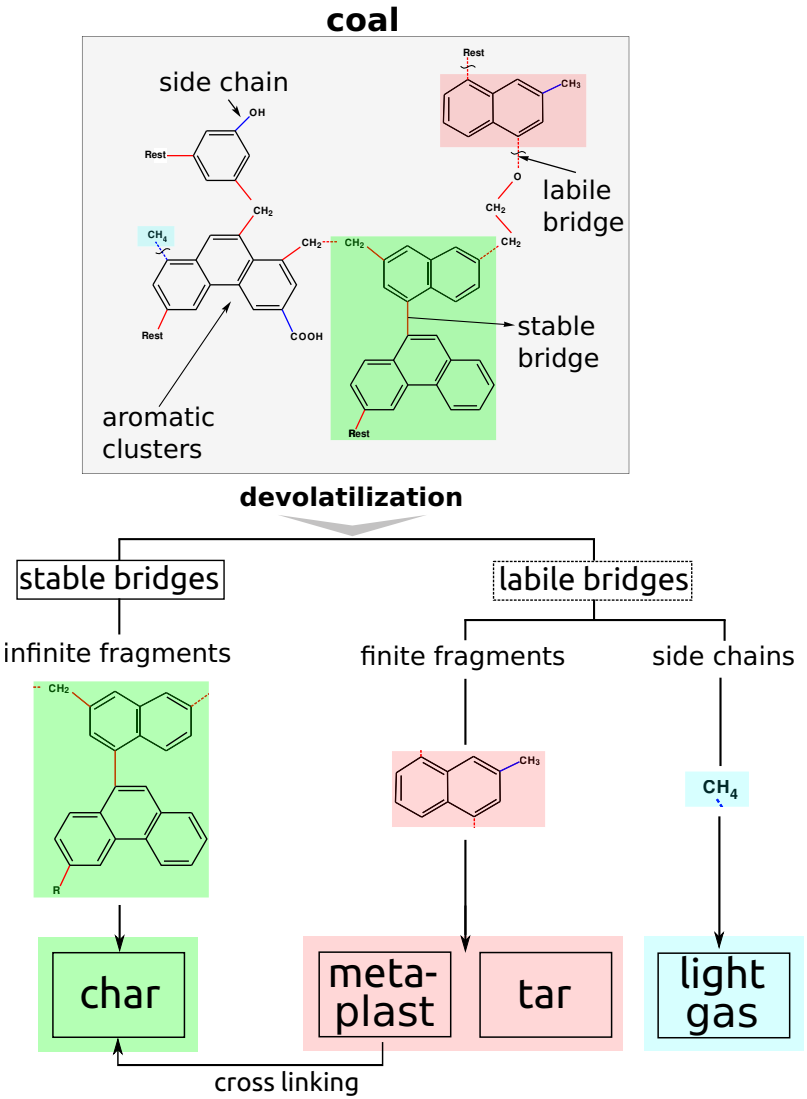

Figure 3.1: Schematic of the coal molecular structure and devolatilization process in the CPD model. The coal molecular structure is a modification of [120].

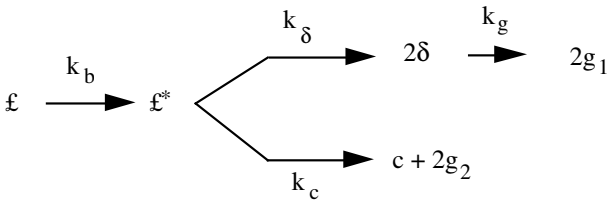

Figure 3.2: The chemical reaction pathway applied in the CPD model.

differential equations yields the fractions of the broken bridges, side chains and light gases. To compute the fraction of the finite fragments (tar) from the number of the broken bridges, the CPD model applies the percolation theory. In the CPD model, the percolation theory is applied to a Bethe lattice to provide an analytical expression relating the number of broken bridges to the mass of finite fragments.

Applying the CPD model, the release rate and composition of the light gases are computed as a function of time according to the study of Jupudi et al. [121]. The light gases consist of CH_4, CO, H_2O, CO_2, and "other gases". It is assumed the "other gases" calculated by CPD to be C_2H_2, similar to the assumption applied by Jimenez and Gonzalo-Tirado [60] and Goshayeshi and Sutherland [57]. The rate of tar released is also computed by the CPD model and it is assumed that tar is only C_2H_2. This assumption is consistent with the work of Goshayeshi and Sutherland [57] and Tufano et al. [58] on ignition of the same coal considered in the present work. To assess the effect of this assumption on ignition delay, selected ignition cases have been computed replacing C_2H_2 with a heavier hydrocarbon, i.e., benzene (C_6H_6) and no significant differences in the ignition process have been observed. Ignition sensitivity to the tar composition is explained in the section 3.2.3.2.

The input parameters for the CPD model are the coordination number of the coal lattice, the molecular mass of aromatic clusters, the molecular mass of side chains, and the fraction of broken bridges. In a lattice, the coordination number refers to the number of possible bridges between a certain node and its neighboring nodes. The input parameters for the CPD model can be extracted from ^{13}C NMR spectroscopy measurements of the coal molecular structure. The ^{13}C NMR spectroscopy is an expensive process, and therefore, the required input parameters for many coal types are not available. Genetti et al. [122] developed a non-linear correlation according to ^{13}C NMR data of 30 coal samples. The developed correlation yields required CPD input

parameters from the ultimate and proximate analysis of coal.

Proximate analysis		
	wr.%,as rec'd	wt.% dry
Moisture	1.4	
Ash	6.9	7.0
Volatiles	35.4	35.9
Fixed carbon	56.3	57.1
Ultimate analysis		
	wr.% dry	wt.% daf
C	77.2	82.9
H	5.2	5.6
O	7.2	7.7
N	1.5	1.6
S	2.0	2.2

Table 3.1: Proximate and ultimate analysis of the Pittsburgh coal [47] employed in the present study.

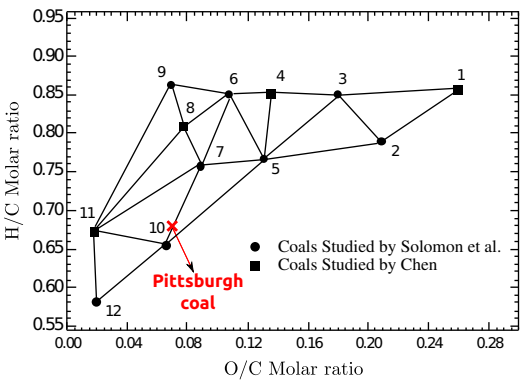

Figure 3.3: The interpolation mesh applied in the CPD model to compute light gas composition reported by [123] and [121]. The Pittsburgh coal, used in the current study, is marked on the interpolation mesh.

3.1.2.4 Coal type

The Pittsburgh coal used by Liu et at. [47], has been employed for the current study. The proximate and ultimate analysis of this coal is shown in Tab. 3.1. The current Pittsburg coal is in the validity range of the CPD model. Figure 3.3 shows the interpolation mesh for the light gas composition in the CPD model. The current Pittsburg coal is marked within the interpolation mesh of O/C and H/C molar ratios.

3.1.3 Interphase coupling

In the current study, equations of the particle and gas phase are fully coupled. Figure 3.4 schematically shows the applied coupling approach. The gas phase

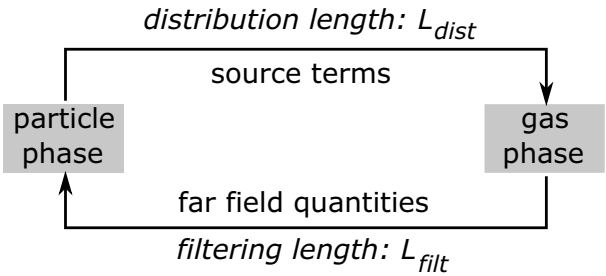

Figure 3.4: Schematic of the applied interphase coupling approach.

is coupled to the particles through the source terms appearing in Eq. (3.1)-(3.4) at each computational cell with volume $\Delta\Omega_g$. The source terms for mass, species, momentum, and energy are computed as:

$$\dot{S}_m = -\frac{1}{\Delta\Omega_g}\sum_{k=1}^{n_p}\phi_p^k\left(\frac{dm_p^k}{dt}\right), \tag{3.18}$$

$$\dot{S}_{Y_i} = -\frac{1}{\Delta\Omega_g}\sum_{k=1}^{n_p}\phi_p^k\left(\frac{dm_{p,d,i}^k}{dt}+\frac{dm_{p,e,i}^k}{dt}\right), \tag{3.19}$$

$$\dot{S}_{U,\alpha} = -\frac{1}{\Delta\Omega_g}\sum_{k=1}^{n_p}\phi_p^k\left(\frac{dm_p^k}{dt}U_{p,\alpha}^k + m_p^k\frac{dU_{p,\alpha}^k}{dt}\right), \tag{3.20}$$

$$\dot{S}_T = -\frac{1}{\Delta\Omega_g}\sum_{k=1}^{n_p}\phi_p^k\left(\frac{dm_p^k}{dt}C_p^k T_p^k + \dot{\Psi}_{p,c}^k\right), \tag{3.21}$$

where n_p refers to the total number of particles in the domain and ϕ_k is a distribution coefficient for the source terms of the k^{th} particle. ϕ_k is computed from a Gaussian function with a characteristic width L_d, centered at the k^{th} particle. This approach is similar to the approach used by Apte et al. [124]. The distribution length L_d is set to $2D_p$, where D_p is the particle diameter. All simulations were performed using a uniform grid with a cell size Δx, equal to the particle diameter. Increasing L_d from D_p up to $5D_p$ (corresponding to a volume of $125\Delta x^3$) changes the ignition delay by less than 10%. With the bigger values of L_d, the source term is distributed far beyond the reaction zone around each particle, which leads to a significant influence on the ignition delay time.

The particles are coupled to the gas phase through the gas phase quantities required in the particle equations. In the Lagrangian-Eulerian approach, particle equations are derived according to the film model assuming a uniform gas field around the particle. To evaluate the state of the particle surrounding consistently with the film model, a filter is applied to provide smoother gas phase fields. The quantities required from the gas phase are averaged within a cube with side length L_f, centered at the particle location. Sensitivity studies showed that the filter length does not have any significant effect on the results.

3.1.4 Numerical methods

The governing equations are implemented and solved using a semi-implicit finite difference numerical method [98]. Similar to the approach applied in the second chapter, the scalar equations (Eqs. (3.2) and (3.4)) are first advanced for the species mass fractions and temperature using the Strang splitting approach [99]. Strang splitting is performed by applying two independent operators referred to as transport operator, which includes convective, diffusive, and particle source terms, and chemistry operator, which accounts for the source term due to the homogeneous reactions. Accordingly, Eqs. (3.2) and (3.4) are solved for half (time step) transport, then full (time step) chemistry, and finally half (time step) transport. The transport step is performed using a third order WENO scheme [101] for the convective terms and a second order central difference scheme [98] for the diffusive terms. The chemistry step is advanced using the CVODE solver of the Sundials library [125]. After updating the species mass fractions and temperature, the density is updated

using the equation of state. The momentum equation is solved applying a second order central difference scheme [98] and the Poisson equation (derived from Eqs. (3.1) and (3.3) using the low-Mach assumption) is solved applying the multi-grid solver of HYPRE [102]. The Crank-Nicolson method is applied for time advancement along with an iterative predictor-corrector scheme similar to the method developed by Kim and Moin [126]. To update the particle state, position, and the source terms for the gas phase equations, the particle equations are advanced using a two stages Runge-Kutta solver with second order of accuracy. The particle equations are only advanced in the beginning of the time step and the particle source terms (in the gas phase equations) are then constant during the first and second transport steps.

3.2 Validation

Since modeling ignition and combustion of coal particles requires a significant number of physical models and simplifying assumptions, a comparison with available experimental measurements [47] and previously published numerical results [57] is presented in this section.

3.2.1 Experimental setup

Validation is performed by comparing the computed ignition delay time τ_{igni} with the experimental data provided in the study of Liu et al. [47]. Their experiments were performed in the laminar entrained flow reactor at Sandia National Laboratories. In their reactor, a diffusion flamelet-based Hencken burner is used so that a gas flow with high temperature and velocity can be provided. A 5cm $\times$ 5cm square glass isolates the reactor from surrounding air and provides optical access for experimental measurements. In the experiment, particles are injected with a carrier gas from a thin tube with diameter $D_{\text{tube}} = 0.75$ mm located at the center of the burner inlet. In addition, the hot gas oxidizer (coflow) enters the furnace and rapidly mixes with the carrier gas providing the energy for particle heating.

Liu et al. [47] experimentally studied the particle feeding rate effect on the ignition delay time under various conditions. Figure 3.5 shows their photographs of igniting and burning streams of the Pittsburgh coal with particle diameter within 75 to 105 μm in Sandia's laminar entrained flow reactor with the initial gas temperature of 1320 K. Liu et al. [47] varied the coal feeding rate from 0.005 to 1 g/min in order to cover transition from single particle to group ignition. In their experiments, ignition mainly happens

at the height of $50D_{\text{tube}}$ from the inlet or above. They computed ignition delay time by measuring ignition location and assuming a constant velocity of 2.5 m/s along the vertical centerline of the burner. In the experiment [47], the ignition location is defined as the height above the burner where the

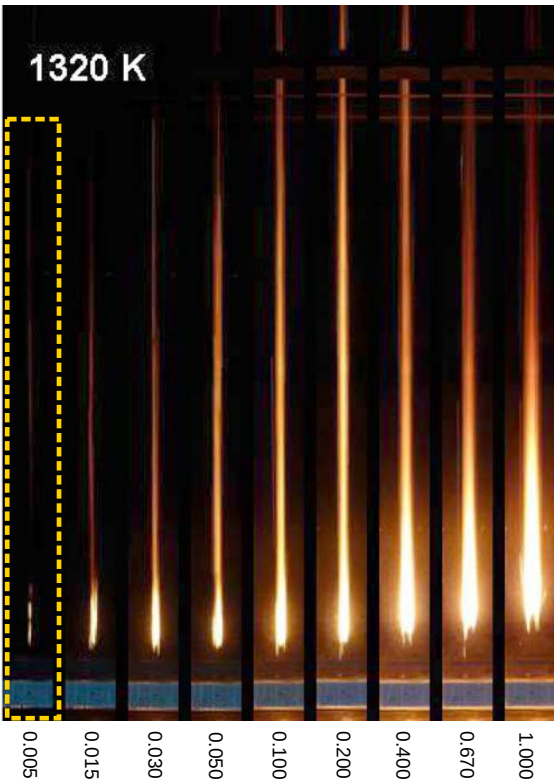

Figure 3.5: Photographs of igniting and burning streams of the Pittsburgh coal with particle diameters within 75 to 105 μm in Sandia's laminar entrained flow reactor with the initial gas temperature of 1320 K. The particle feeding rate is increasing from left to right. The lowest particle feeding rate of 0.0005 g/min represents single particle combustion. This image is taken from the experimental study by Liu et al. [47], where more details about the experimental setup can be found.

CH intensity reaches half of its maximum value. The measured ignition delay times for the cases with very low particle feeding rate of 0.005 g/min correspond to the single particle ignition, and are mainly considered here.

3.2.2 Numerical configurations

Ignition and combustion of coal particles in the laminar entrained burner depend on the interactions between particles, combustion, and mixing of the coflow and carrier gas. Figure 3.6 schematically shows four possible numerical configurations to compute coal combustion in the laminar entrained flow reactor. In configuration i, single particle combustion is considered in a periodic cube. In this configuration, particle/combustion interactions can be investigated. In configuration ii, combustion of a particle group is considered in a single hot gas flow. In this configuration, particle/particle/combustion interactions can be studied. Differently from configurations i and ii, configuration iii and iv include mixing between particle carrier gas and coflow to capture particle/particle/combustion/mixing interactions. Due to simplicity, configurations i and ii require less computational effort and are more appropri-

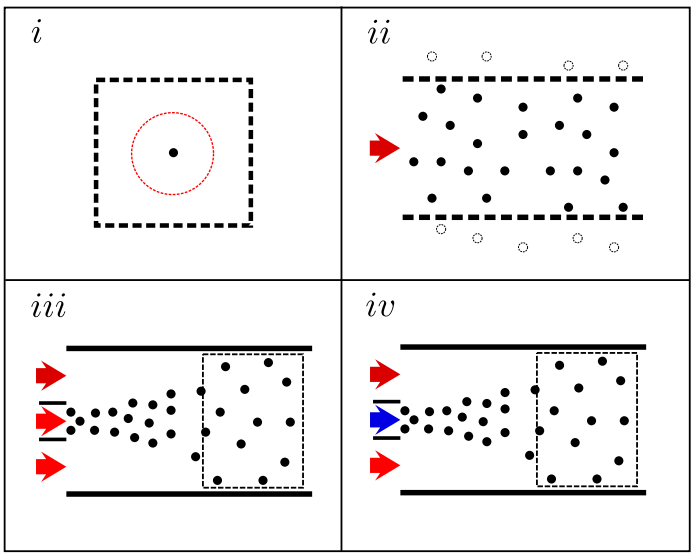

Figure 3.6: Schematic of the possible configurations; i, ii, iii, iv to study coal combustion. Configuration i and ii are the objective of the current study.

ate to perform validation for a larger set of conditions. Therefore, to validate the current model with the experimental measurements of the ignition time at very low feeding rate, configuration i is applied. In configuration i, it is assumed that in the experiment, the carrier gas has the same properties as the coflow and particle slip velocity is negligible. Uncertainties regarding these assumptions are discussed in section 3.2.3.1. Figure 3.7 represents the applied numerical configuration, where a single coal particle with the diameter D_p is located at the center of a periodic cube with side length $L_x = 61D_p$, $L_y = 61D_p$, and $L_z = 61D_p$ in x, y, and z directions, respectively. The periodic cube consists of the stationary gas with the same initial composition and temperature as the coflow of the experiment.

Ignition delay time is computed for a large set of conditions, varying particle size ($55-125$ μm), initial gas temperature ($1200-1670$ K), and diluent in the gas phase (N_2 and CO_2). Cases A, B, and C are used for a detailed validation against experimentally measured ignition delay time data by Liu et al. [47].

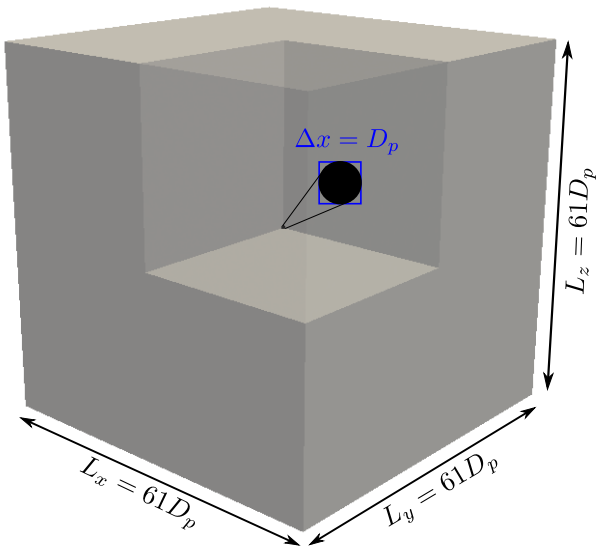

Figure 3.7: Applied numerical configuration, which includes a periodic cube with side length $61D_p$, where D_p is the diameter of the coal particle located in the middle of the cube. The numerical domain is discretized by a uniform grid with cell length $\Delta x = D_p$.

Case	A(1-7)	B(1-6)	C(1-6)	Air(1-15)	Oxy(1-15)
D_p [μm]	55-125	90	90	55-125	55-125
T_g [K]	1320	1200-1670	1200-1670	1175-1500	1175-1500
X_{N_2}[-]	0.464	0.384	0	0.684	0
X_{CO_2}[-]	0.3	0.3	0.684	0	0.684
X_{O_2}[-]	0.12	0.2	0.2	0.2	0.2

Table 3.2: Conditions for all the particle ignition cases considered: particle diameter D_p, initial gas temperature T_g, and gas-phase species mole fractions X_i. In all cases, gaseous mixture contains steam with the value of 0.116 and the initial particle temperature is 300 K.

These cases are labelled A(1-7), B(1-6), and C(1-6) in Tab. 3.2. In cases A(1-7), the particle diameter is varied keeping the gas-phase properties constant; in cases B(1-6) and C(1-6), the initial gas temperature is changed. In addition, the N_2 species in B(1-6) is replaced by CO_2 in C(1-6).

In order to compare the results in a consistent way, the ignition delay time τ_{igni} is computed with the same criteria used by Liu et al. [47] and Goshayeshi and Sutherland [57]. In the experiment [47], the ignition delay time is defined as the time at which the CH intensity reaches half of its maximum value. The ignition delay time is also computed according to the evolution of the maximum mass fraction of CH radical. An error bar for this computation is defined by the width of an interval from the first sharp increase in $Y_{\text{CH,max}}$ to the time when $Y_{\text{CH,max}}$ reaches its peak. Figure 3.8 shows the ignition delay times for various particle diameters ($55 - 125$ μm). This plot includes results from the current study compared with those from the numerical study by Goshayeshi and Sutherland [57] together with experimental data by Liu et al. [47]. Computed results are in good agreement with both numerical and experimental studies. Figure 3.8 also shows the ignition delay times for different values of the initial gas temperature ($1200 - 1670$ K). The present results agree well with the numerical simulations of Goshayeshi and Sutherland [57] and with experimental data. Furthermore, the cases C(1-6) with CO_2 as diluent are considered. Also for these cases, the present results are in close agreement with the experimental measurements.

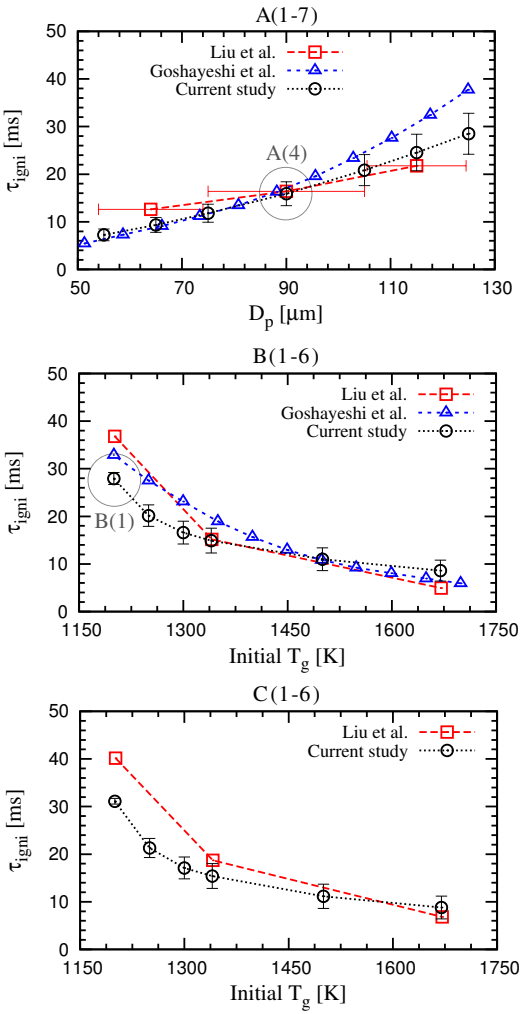

Figure 3.8: Ignition delay times at various particle diameters in cases A(1-7), and at various initial gas temperatures in cases B(1-6) and C(1-6). These cases are defined in Tab. 3.2. Results from the Current study are compared with experimental data reported by Liu et al. [47] and numerical data by Goshayeshi and Sutherland [57].

3.2.3 Error analysis

Here, the uncertainties regarding assumptions about the numerical configuration and tar composition will be discussed.

3.2.3.1 Numerical setup

The applied models are validated by comparing computed ignition delay times of a coal particle in a periodic cube with the measured ignition delay times from experiments by Liu et al. [47]. However, the particle in box configuration is simplified and assumes fast mixing of the carrier stream with the hot gas so that negligible relative velocity is reached quickly. To assess these assumptions, additional simulations are performed considering the mixing process as well. To quantify uncertainties due to the numerical approach and the approximation in the configuration setting, particle ignition is computed in two additional cases with an inlet-outlet set-up, similar to the experiment by Liu et al. [47]. As it is shown in Fig. 3.9, these two cases have 3-D inlet-outlet configuration and are employed in order to test the simplification of a periodic domain for case A(4), defined in Tab. 3.2.

For the first case (on the left side of Fig. 3.9), a single coal particle is injected from the inlet boundary with a jet of carrier gas that differs in terms of gas composition, temperature, and velocity from the surrounding coflow. For the second case (on the right side of Fig. 3.9), rapid mixing between carrier gas and coflow is assumed, and the particle is injected with the carrier gas having the same composition, temperature, and velocity as the coflow. The second case is very similar to the configuration used by Goshayeshi and Sutherland [57].

Fig. 3.9 shows the computed gas temperature at different heights of the burner (and corresponding times) for both configurations. The coal particle is marked with a black circle at each time in the corresponding 2-D plot of the gas temperature. In the first case, the particle is moving slightly slower and the surrounding gas has lower temperature. The reason is the lower velocity and temperature of the carrier gas in the first case, which is similar to the experimental setup. To assess the assumption in the validation configuration, the ignition delay time for both cases can be compared with that for the particle in the box configuration in Tab. 3.3. The computed ignition delay time in the first case is 9% higher than that of the particle in a box (case A(4)). This extra time is required for mixing between the carrier stream and the ambient gas inside the burner. Due to the very low particle Reynolds number, ignition delay in the second case is only 1% higher than that computed for

the particle in the periodic box, i.e., case A(4).

3.2.3.2 Tar composition

In order to assess the effect of the choice of the gas species released as tar, single particle ignition in the A(4) case has been performed employing a heavier hydrocarbon as tar species.

First, it should be noted that, in a purely gas-phase setting, C_2H_2 is characterized by a significantly shorter ignition delay time compared to heavier hydrocarbons. Therefore, 0-D simulations are performed to compare ignition delay times of C_2H_2 and benzene (C_6H_6) in a gaseous mixture without particle. Figure 3.10 shows that C_6H_6 ignites around 10 times slower than C_2H_2. Figure 3.10 also shows that both C_6H_6 and C_2H_2 mixtures have a significantly shorter ignition delay time than that observed in the particle simulations. This observation suggests that the kinetics of the homogeneous reactions might play a relatively small role in the ignition of coal particles.

To investigate this point, simulations of particle ignition are performed using C_6H_6 as tar. Figure 3.11 shows the evolution of the particle and gas temperature together with the devolatilization rate for the cases with C_2H_2, and C_6H_6 as tar species. The ignition delay time for each case is marked with a vertical line in Fig 3.11. In the case with C_6H_6, all the quantities evolve very similarly to the case with C_2H_2. Overall, replacing C_2H_2 by C_6H_6 increases ignition delay time by less than 3%.

In fact, the ignition delay time is mainly controlled by the time required for particle heating. In order to start volatile release, the particle temperature should be around 800 K. The time required to reach this temperature, is more than 10 ms, which is much larger than the characteristic time for ignition of C_2H_2 and C_6H_6, as shown in Fig. 3.10. Therefore, ignition delay time of particles shows very low sensitivity with respect to the choice of tar composition. In fact, for the coal type in the current study, the ignition delay time is

Configuration	τ_{igni} [ms]
Inlet-outlet (w mixing)	17.6
Inlet-outlet (wo mixing)	16.2
Particle in box	16.0

Table 3.3: Ignition delay time of case A(4) in inlet-outlet configurations and stationary particle in a periodic box.

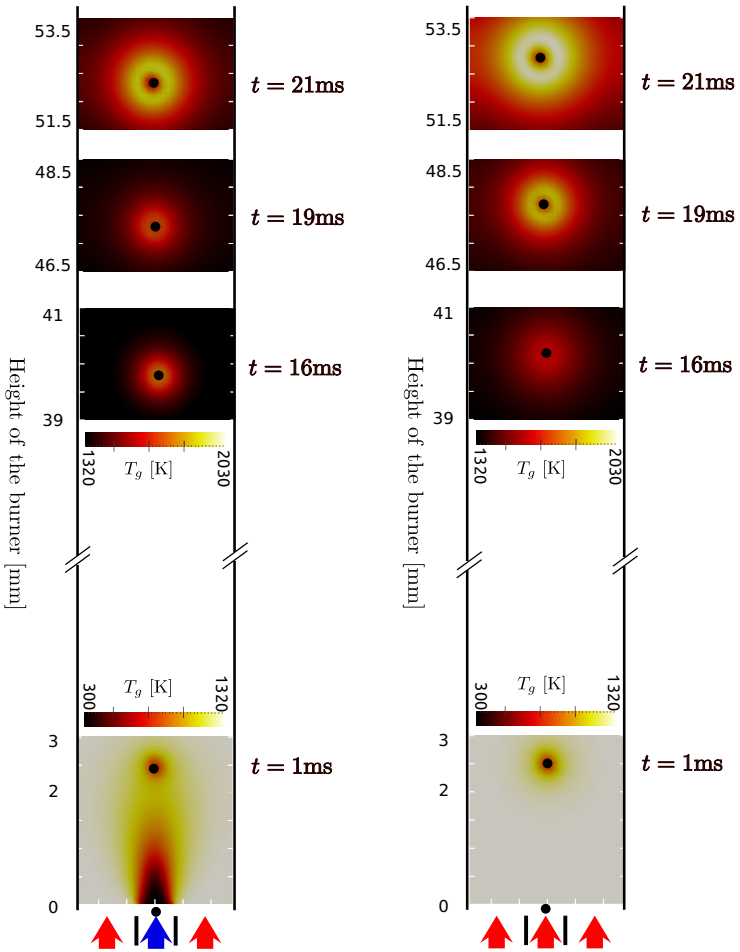

Figure 3.9: The left configuration represents Sandia's laminar entrained flow reactor including the mixing process between carrier and coflow similar to the experiment performed by Liu et al. [47]. In the right configuration, the mixing process between the carrier and coflow gases is excluded and the particle carrier gas is assumed to have the same temperature, composition, and velocity as the coflow gas. Computed gas temperature at different heights of the burner (and corresponding times) can be compared between the configurations.

mainly controlled by the time required for particle heating. For other coal types, which are also characterized by an ignition delay time dominated by the characteristic time required for particle heating, it is speculated that the conclusion regarding the choice of C_2H_2 as tar holds true.

3.3 Single particle ignition

Coal ignition is first studied by applying the single particle configuration to exclude particle/particle interactions. Ignition of the single coal particle is considered in both air and oxy-atmosphere. To perform a comprehensive comparison between air and oxy-atmosphere, coal ignition is computed for 30 different cases. These cases are defined in Tab. 3.2 as Air(1-15) in $N_2/O_2/H_2O$ and Oxy(1-15) in $CO_2/O_2/H_2O$ mixtures referred to as air and oxy-atmosphere, respectively. In each case, a single coal particle is located in the middle of a 3-D periodic cube, similar to the configuration in Fig. 3.7 that was applied for the model validation. For both Air and Oxy cases, a large set of conditions is covered by varying particle size from 55 to 125 μm and initial gas temperature from 1175 to 1500 K.

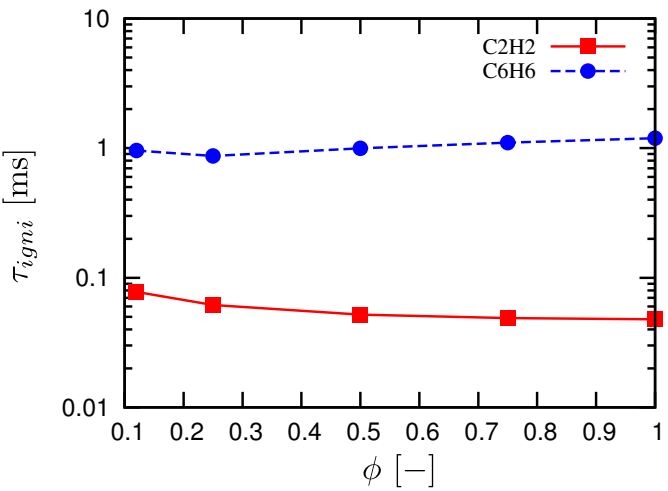

Figure 3.10: 0-D ignition delay time of C_2H_2 and C_6H_6 in a gaseous mixture without particle, at gas temperature of 1300 K under different fuel/oxidizer ϕ rations ranged from 0.1 to 1.

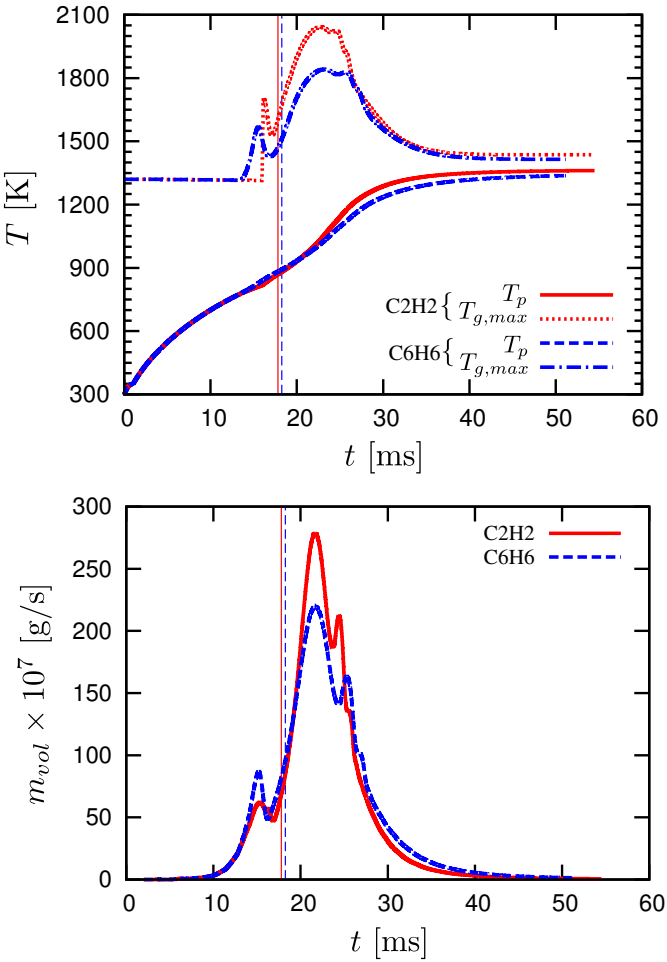

Figure 3.11: Evolution of T_p the particle temperature and $T_{g,max}$ the maximum gas temperature together with m_{vol} the devolatilization rate for cases with C_2H_2, and C_6H_6 as tar species.

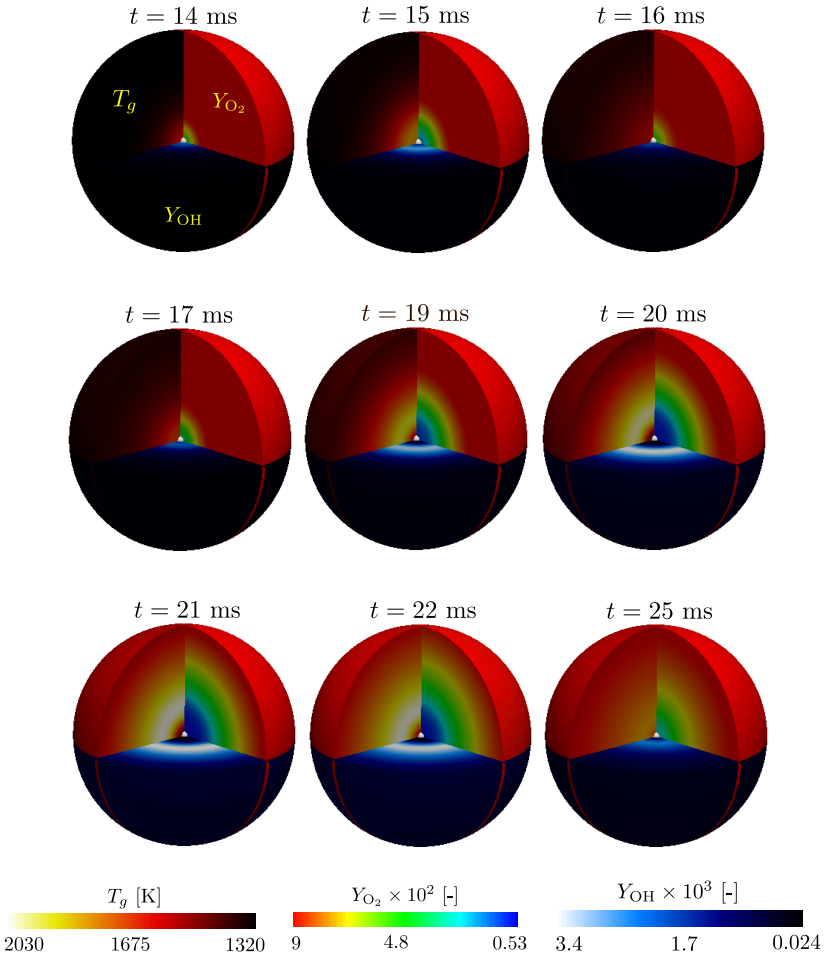

Figure 3.12: Distribution of gas temperature, mass fraction of O_2 and OH around the coal particle from time $t = 14$ to 25 ms for case A(4) defined in Tab. 3.2 with particle diameter $D_p = 90$ μm.

3.3.1 Results and discussions

3.3.1.1 Volatile flame evolution

The ignition and development of a typical volatile flame is shown in Fig. 3.12 for the case A(4). The particle diameter considered is $D_p = 90$ μm and the

initial gas temperature is $T_g = 1320$ K. The properties of the hot ambient gas are defined in Tab. 3.2. The flame front initially forms in the vicinity of the particle and then moves outwards. At $t = 16$ ms, the flame weakens and moves slightly towards the particle. A decrease in the temperature and the OH mass fraction are observed during this phase. As time progresses, the temperature and radical mass fractions increase again and remain rather stable for a few milliseconds. After $t = 22$ ms, the volatile flame begins to extinguish.

To understand the process of volatile flame formation, the evolution of selected quantities are shown in Fig. 3.13 for the two cases A(4) and B(1). These cases differ in the initial temperature and oxygen concentration in the gas phase. The two cases are compared as they show a different mechanism for the ignition of gas phase reactions. The volatile flame evolves faster in the A(4) case, due to the higher initial gas temperature. In both cases, the particle temperature increases due to the energy transfer from the surrounding gas. Approaching a certain particle temperature, enough bounds inside the coal network break and volatile gases begin to be released from the particle. The released volatiles diffuse away from the particle towards the hot oxidizer and form a volatile flame. The heat released from the volatile flame rapidly increases the gas phase temperature. The elevated temperature of the surrounding gas accelerates particle heating and consequently the devolatilization process is enhanced.

3.3.1.2 Double peak profile

Within the early stage of devolatilization, the rate of devolatilization m_{vol} shows two distinct peaks. This typical behavior is explained by Yang et al. [48] in the context of the CPD model. The first peak is due to the release of light tar compounds not initially connected with the coal lattice. The second peak is caused by the release of heavier tar compounds due to the cleavage of the bridges between aromatic clusters. For the case A(4), the double peak in the devolatilization rate m_{vol} results in two distinct peaks also in the maximum gas temperature $T_{\mathrm{g,max}}$. On the contrary, the double peak profile is not present in the gas temperature profile for the case B(1). Due to the lower initial gas temperature of case B(1), the particle does not ignite when the first part of the volatiles is released and ignition occurs only at the onset of the second peak of the devolatilization rate m_{vol}. This is evident from the profile of heat released from gas-phase combustion Q_g, which is negligible for the entire duration of the first volatile release. It is worth noting that the much longer ignition delay time observed for case B(1) compared to A(4), is

mostly related to the lack of ignition during the first release of volatile matter. If ignition happened during the first volatile release also for case B(1), the ignition delay time would be much shorter and close to the value obtained for case A(4). In addition, it is clear that ignition cannot be predicted solely from the devolatilization rate, but the diffusive-reactive processes in the gas phase need to be included.

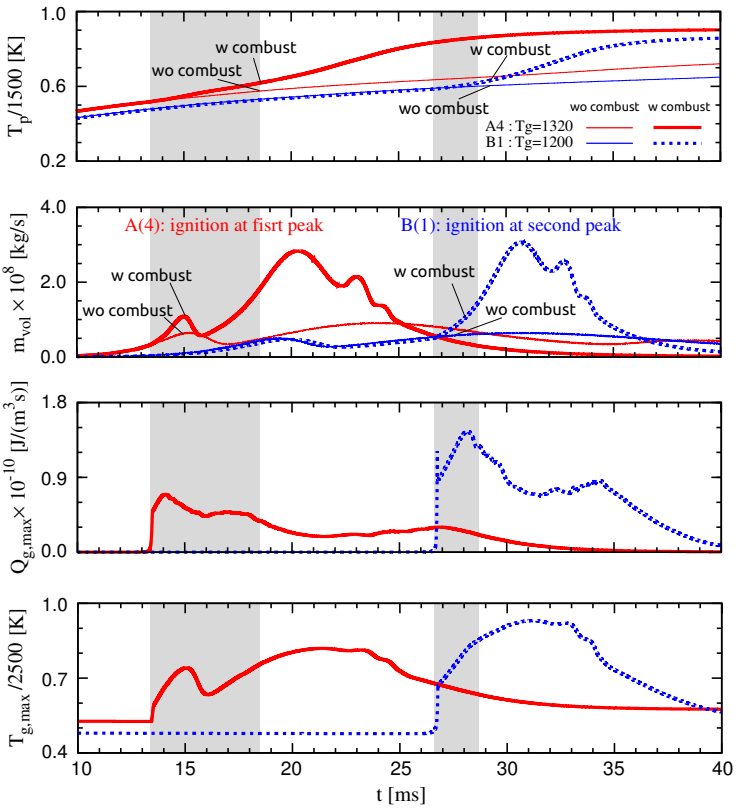

Figure 3.13: Evolution of the particle temperature T_p, rate of volatile release m_{vol}, maximum heat release rate from combustion in the gas-phase $Q_{\mathrm{g,max}}$, and maximum temperature of the gas phase $T_{\mathrm{g,max}}$ for case studies A(4) and B(1). In both cases, particle diameter is 90 μm. Case A(4) has initial gas temperature of 1320 K and oxygen mole fraction of 0.12, while in case B(1), initial temperature is 1200 K and oxygen mole fraction 0.2.

In order to provide more details on the role of the gas-phase flame on the process, the results are compared with two cases at the same conditions and for which the gas-phase combustion is artificially suppressed (shown as "wo combust" in Fig. 3.13. The double peak behavior in the devolatilization rate is still present, proving that it is due to the devolatilization process modeled with the CPD approach. However, the heat release from gas-phase combustion significantly increases the maximum value of the second peak and shifts its appearance to a slightly earlier time.

Since the ignition delay time is strongly influenced by the presence (or lack) of significant heat release during the first peak of the devolatilization rate, it is of interest to assess the influence of the particle size and ambient conditions on this phenomenon. From the analysis of the multiple cases described in Tab. 3.2, it is found that the particle diameter and the initial gas temperature have strong influence on this process. The abundance of CO_2 is also important, and its effect is described in section 3.3.1.3. Figure 3.14 shows the evolution of $T_{g,max}$ for several cases with various particle sizes at the same initial gas temperature and cases with different initial gas temperatures for the same particle size. The parametric study reveals that the maximum temperature in the gas phase $T_{g,max}$ approaches a double peak profile by increasing the initial gas temperature, the particle size or both. The double peak in the gas phase temperature is observed if ignition occurs during the first peak of

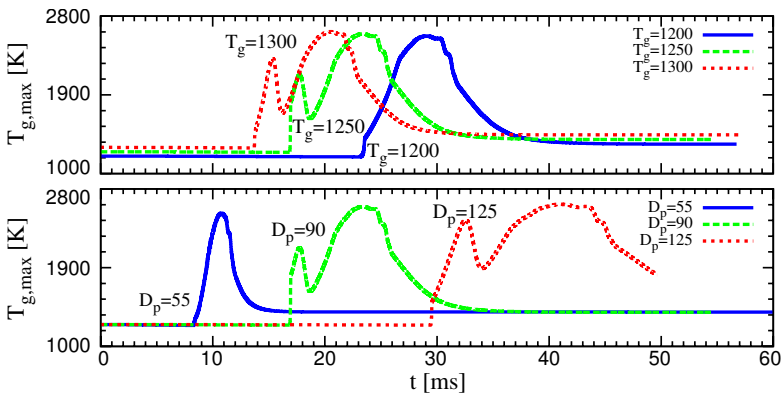

Figure 3.14: Evolution of maximum gas temperature for different cases; varying initial gas temperature (with $D_p = 90$ μm) and varying particle size (with initial $T_g = 1250$ K). These cases are defined as air in Tab. 3.2.

devolatilization. The higher initial gas temperature provides more energy to activate gas phase reactions such that the particle can ignite during the first peak of volatile release. The larger particle releases more volatile due to the higher surface area and therefore, enables the ignition at the first peak of volatile release. Figure 3.14 further shows that the double peak in the flame temperature profile might be present for cases with short and long ignition delay time. Furthermore, it is observed that the distance between the two peaks increases if the diameter of the particle is increased or if the initial gas temperature is decreased. This analysis might also help to explain the two peaks observed in some experimental measurements of the gas phase temperature and species concentration during coal ignition and combustion [50–52].

3.3.1.3 Ignition in air versus oxy-atmosphere

Figure 3.15 shows the ignition delay time for the air and the oxy-atmosphere at various particle sizes and gas temperatures. Keeping the initial gas temperature constant, ignition delay times decrease with the particle size. Smaller particles ignite faster because they have a higher surface to volume ratio

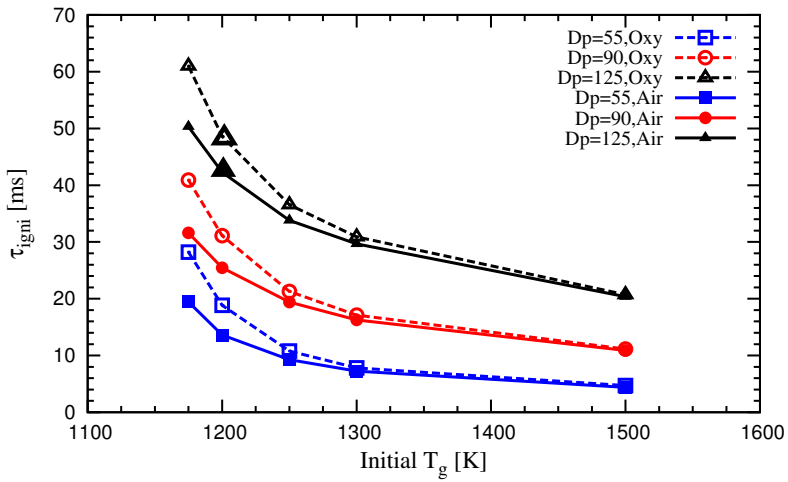

Figure 3.15: Ignition delay time for various particle diameters and gas phase temperatures in air and oxy-atmosphere. These cases are defined as Air(1-15) and Oxy(1-15) in Tab. 3.2.

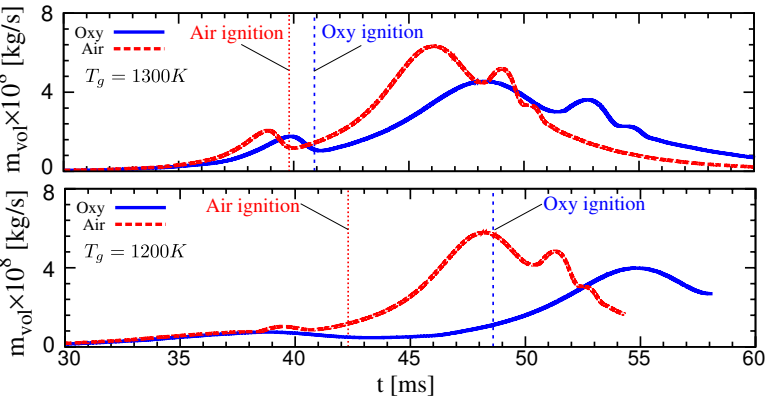

Figure 3.16: Evolution of the devolatilization rate for a 125 μm particle in air and oxy-atmosphere with initial temperature $T_g = 1300$ K and $T_g = 1200$ K. Gas composition of air and oxy-atmosphere are defined in Tab. 3.2.

and consequently, heat up faster. For constant particle size, coal particles ignite faster at higher initial gas temperatures. Higher gas temperatures accelerate the devolatilization process as well as the chemical reactions in the gas phase. At lower temperatures and in both atmospheres, the ignition delay time becomes more sensitive to the variation of the initial gas temperature. For all gas temperatures and diameters, coal particles require a longer time to ignite in oxy-atmosphere compared to air. For each particle size, the difference between air and oxy-atmosphere becomes more significant with decreasing initial temperature of the gas phase. To understand the reason of this increased difference, the time evolution of the devolatilization rate for both air and oxy cases at two different temperatures is shown in Fig. 3.16. For $T_g = 1300$ K, coal particles ignite around the first peak of devolatilization for both atmospheres. For $T_g = 1200$ K, ignition occurs at the onset of the second peak of devolatilization. While the location of the first peak does not change much if the temperature goes from 1300 K to 1200 K, the location of the second peak is much more sensitive to temperature variations.

3.3.1.4 Primary reason for delayed ignition in oxy

The slower ignition in oxy-atmosphere can be related to the thermal or chemical effects induced by the presence of CO_2. An increase of ignition delay in the presence of CO_2 was already observed in a number of experiments [17, 41, 47, 53–55], and was ascribed to the higher heat capacity of CO_2, its chemical properties, or a combination of both. To investigate the reason of the increased ignition delay, a detailed analysis of air and oxy cases with initial gas temperature of 1200 K is performed.

Figure 3.17 shows the evolution of the maximum gas temperature $T_{g,max}$ in both atmospheres. As the coal particle ignites earlier in air atmosphere, the

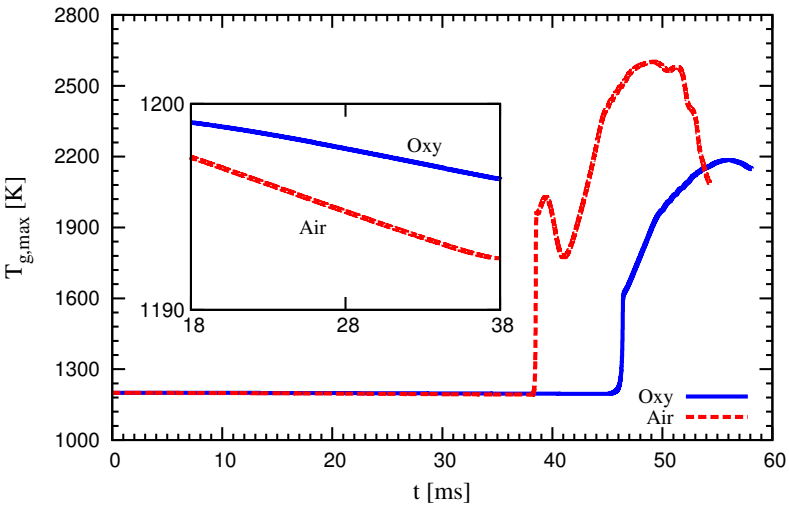

Figure 3.17: Evolution of the maximum gas temperature for a 125 μm particle in air and oxy-atmosphere with the initial temperature $T_g = 1200$ K.

first sharp increase in $T_{g,max}$ occurs earlier around $t = 38$ ms. Notwithstanding the earlier ignition in air atmosphere, the zoomed view in Fig. 3.17 shows that, up to $t < 38$ ms, the oxy-atmosphere case displays a higher temperature in comparison to the air case. This difference can be explained by the heat capacity of CO_2, which is almost 1.5 times higher than the heat capacity of N_2. During particle heating, for the same amount of energy transfer to the particle, the gas-phase in the oxy-atmosphere case experiences a smaller temperature

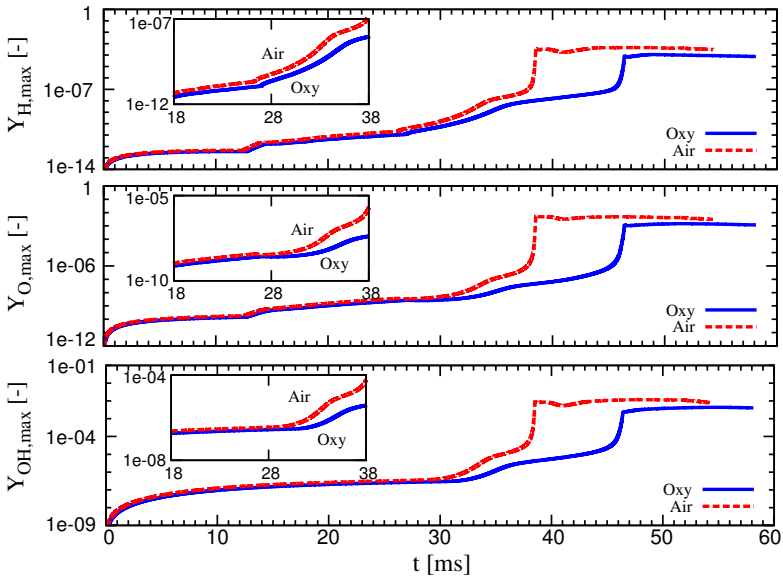

Figure 3.18: Evolution of H, O, and OH radical mass fractions for a 125 μm particle in air and oxy-atmosphere with initial temperature $T_g = 1200$ K.

drop due to the higher heat capacity of CO_2. Based on this observation regarding the gas temperature in the two cases, it is concluded that the higher heat capacity of CO_2 has very little effect on the ignition delay and its effect would be toward a decrease, if any. However, after the occurrence of ignition, the higher heat capacity of CO_2 together with its chemical effect results in lower flame temperature in oxy- compared to air atmosphere, consistently with the analysis by Jimenez and Gonzalo-Tirado [60].

Figure 3.18 shows the evolution of the maximum value of mass fractions of $Y_{H,max}$ $Y_{O,max}$, and $Y_{OH,max}$ in both atmospheres. As coal ignites earlier in air atmosphere, each radical profile shows the sharp increase in air (around $t = 38$ ms) earlier than in oxy-atmosphere. Also before ignition, the radical mass fractions are higher in air atmosphere. Among all radicals, the early difference in $Y_{H,max}$ is most evident. To assess the effect of the presence of CO_2 in the chemistry of ignition, a reaction pathway analysis has been performed. It is found that in oxy-atmosphere, H radicals are strongly consumed by the reaction R : $CO_2 + H \rightarrow CO + OH$. Figure 3.19 shows the spatial distribution

of the rate of this reaction, W_{R}, at $t = 18, 23,$ and 28 ms. In comparison

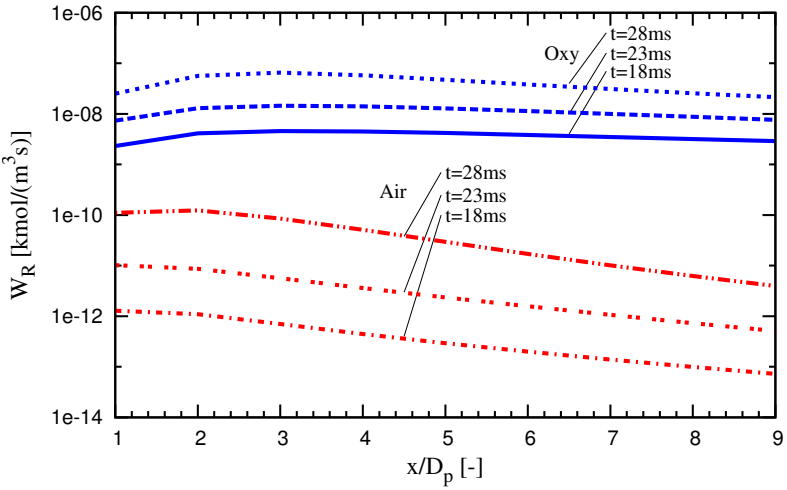

Figure 3.19: Distribution of reaction rate W_{R} for a 125 μm particle in air and oxy-atmosphere with initial temperature $T_g = 1200$ K.

to air atmosphere, W_{R} is almost 1000 times higher in oxy-atmosphere. The reaction rate W_{R} depends on the gas temperature and the concentrations of H and CO_2 species. In oxy-atmosphere, the rate of reaction is much higher due to the higher CO_2 concentration. In fact, the higher concentration of CO_2 causes an almost complete depletion of H radicals. The H radical depletion decelerates intermediate reactions that are responsible for the production of O and OH radicals such as $O_2 + H \rightarrow OH + O$ and, consequently, the O and OH mass fractions are reduced. It is concluded that the presence of CO_2 decreases the reactivity of the mixture by reducing the mass fraction of radicals (primarily H and consequently O and OH), which results in delayed ignition.

3.3.1.5 Particle porosity evolution

The particle porosity increases the available surface for the heterogeneous reactions and allows the diffusion of oxygen into the particle. As a result, the particle porosity enhances the volumetric burnout rate of the coal particles. In the current study, the critical influence of the particle porosity on the coal

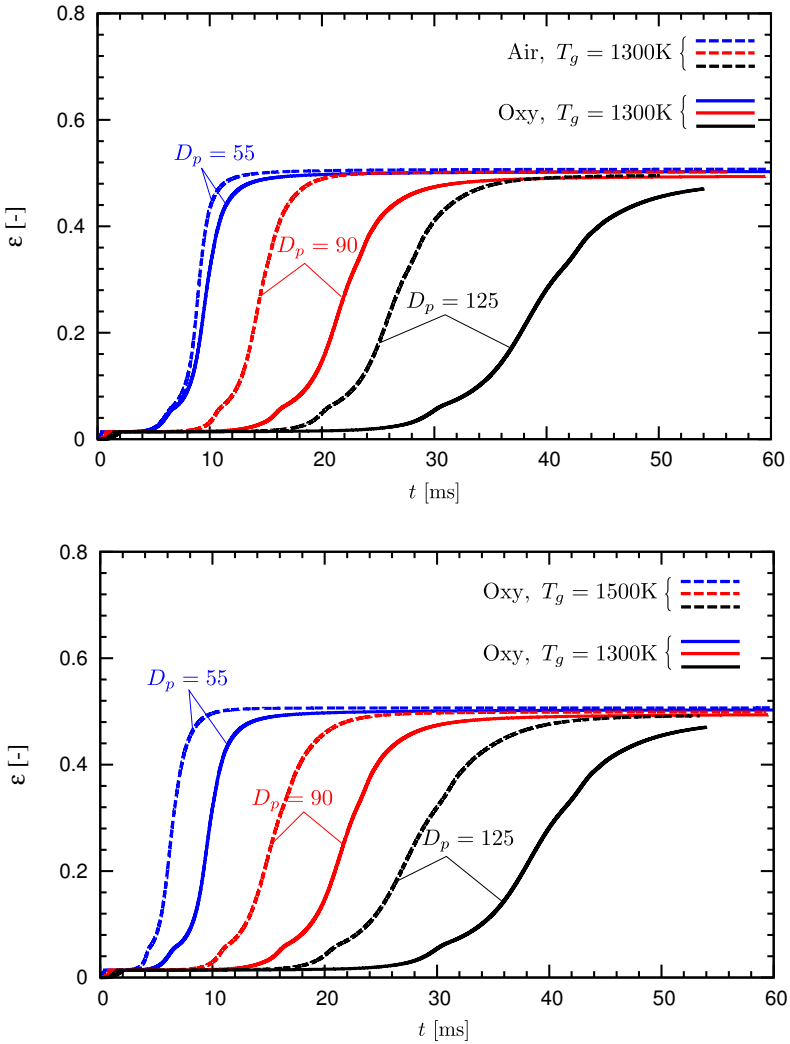

Figure 3.20: Evolution of the particle porosity ϵ in Air and Oxy cases with the same initial gas temperature (upper plot), and in Oxy cases at different initial gas temperatures(lower plot). In both plots, different particle diameters Dp are considered.

burnout rate was observed during computation of the char particle combustion in the second chapter. In the particle resolved approach, the particle porosity has been considered in the form of an effectiveness factor, which accelerates heterogeneous reactions. However, the initial porosity of the char particle is rarely available in the literature. Therefore, the particle porosity during devolatilization phase is computed to provide useful insight towards initial porosity of the char particle.

Here, the evolution of the particle porosity is investigated under air and oxy-atmosphere considering cases defined in Tab. 3.2. The initial porosity of the particle is assumed to be zero. In the current model, the particle size remains constant, while the particle density varies due to the mass loss because of the devolatilization process. The reduction in particle density is assumed to be directly related to the increase in particle porosity. Thus, the particle porosity ϵ evolves in time as $\epsilon(t) = 1 - m_p(t)/m_{p,0}$, where $m_p(t)$ is the particle mass at the time t, and $m_{p,0}$ is the initial particle mass. Figure 3.20 shows the particle porosity evolution in both Air and Oxy cases at initial gas temperature of 1300 K and various particle diameters. Release of volatile accelerates pore formation and thus particle porosity evolution. In each atmosphere, smaller particles experiences faster evolution of the porosity. Comparing Oxy and Air cases shows that porosity of the bigger particles evolves slower under oxy-atmosphere. As Fig. 3.20 shows, increasing initial gas temperatures from 1300 to 1500 K accelerate the particle porosity evolution due to the faster devolatilization process. At the end of the devolatilization process of all cases, the particle porosities become almost 0.5, which can then be referred as the initial porosity of the char particle.

3.4 Particle group ignition

3.4.1 Configurations

The current study containes coal particle stream ignition and combustion in a three-dimensional channel configuration under oxy-fuel atmosphere. The length of the channel in the streamwise direction x, and the spanwise directions y, and z are $L_x = 1000R_p$, $L_y = 62R_p$, and $L_z = 62R_p$, respectively, where R_p is the particle radius with a fixed value of 45μm. For all cases presented, the channel is long enough to ensure that devolatilization is complete when particles reach the outlet. The domain is discretized using a uniform grid consisting of cubic cells with size dx equal to the particle diameter. The channel has inlet and outlet boundaries in the streamwise direction x, while

Case	A1	A2	A3	B1	B3	B4	C3	C4	C5
$U_{g,in}$ [m/s]	1	1	1	0.5	0.5	0.5	1	1	1
$T_{g,in}$ [K]	1300	1300	1300	1300	1300	1300	1500	1500	1500
$N_{p,in}[10^8/\mathrm{m}^3]$	1.25	2.0	2.5	1.25	2.5	3.7	2.25	4.0	4.7
Composition	$X_{\mathrm{CO_2}} = 68.4$,$X_{\mathrm{O_2}} = 20$, and $X_{\mathrm{H_2O}} = 11.6$								

Table 3.4: Prescribed inlet conditions for all cases considered: gas velocity $U_{g,in}$, temperature $T_{g,in}$, particle number density $N_{p,in}$, and gas composition in terms of mole fraction.

periodicity is imposed in the two spanwise directions y and z. Particles are injected from the inlet into the domain with a hot gas stream. This configuration is appropriate to study ignition in regions of a typical industrial burner, where the mixing time is faster than the particle heating time. At the inlet, the prescribed quantities are: the particle number density $N_{p,in}$, the gas temperature $T_{g,in}$, the injection velocity $U_{g,in}$, and the gas composition, which in the present study is: 68.4% CO_2, 20% O_2, and 11.6% H_2O in terms of mole fraction. Particles are injected randomly in time and space with the same velocity of the gas phase, such that the average particle number density is imposed at the inlet. Therefore, the rate of the particle injection is proportional to the prescribed $N_{p,in}$ and $U_{g,in}$ at the inlet. The investigated values were selected from simulations of the dispersed region of the lab-scale coal combustion chamber by Knappstein et al. [127]. Figure 3.21 represents the computed number density by [127] within the quarl region.

Several cases are considered varying the particle number density $N_{p,in}$, the carrier gas temperature $T_{g,in}$, and the gas velocity $U_{g,in}$ at the inlet. These cases are defined in Tab. 3.4, and named with a letter followed by a number. The letter A, B, and C refers to the case category with a certain combination of $T_{g,in}$ and $U_{g,in}$, while the numbers refer to different $N_{p,in}$s in each category. Case A1 is computed with a particle stream characterized by a distribution of particle diameters from 55 to 125 μm, where the average particle diameter is 90 μm. Very similar ignition delay time to the A1 case with a uniform particle size of 90 μm was observed. Therefore, the parametric study was performed by keeping the particle size constant, while varying the particle number density, gas temperature, and velocity. The simulation is initialized with only the gas phase in the entire domain at the thermodynamic condition imposed at the inlet. At time zero, particles start to be injected from the inlet. In all cases, the initial particle temperature is 300 K.

3.4.2 Statistical analysis

Depending on the particle injection rate, the number of particles in the channel increases until time t_p, when the first injected particles leave the channel through the outlet. At $t > t_p$, the system quickly reaches a statistically steady state. Steady state is reached when the time and volume average of all quantities remain constant. A statistical analysis is performed within an interval of 30 ms after the steady state has been reached. 31 snapshots separated by 1 ms were collected and volume averaged quantities denoted as $\tilde{\bullet}$ on the $y-z$ plane at each x location for each time were computed. In addition, the time and volume averaged quantities denoted as $\langle\tilde{\bullet}\rangle$ at each x location were also computed.

As an example, Fig. 3.22 shows the gas temperature distribution for case A1 at five different times in the statistically steady state. Here, Δt is defined as $\Delta t = t - t_s$, where $t_s = 40$ ms and refers to the time at which the system

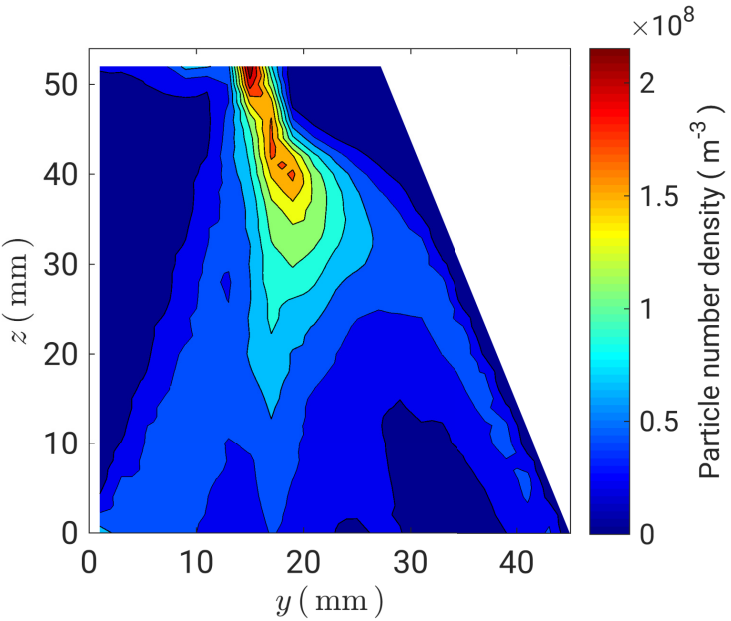

Figure 3.21: Particle number density distribution in the quarl region of a lab-scale coal combustion chamber studied by Knappstein et al. [127].

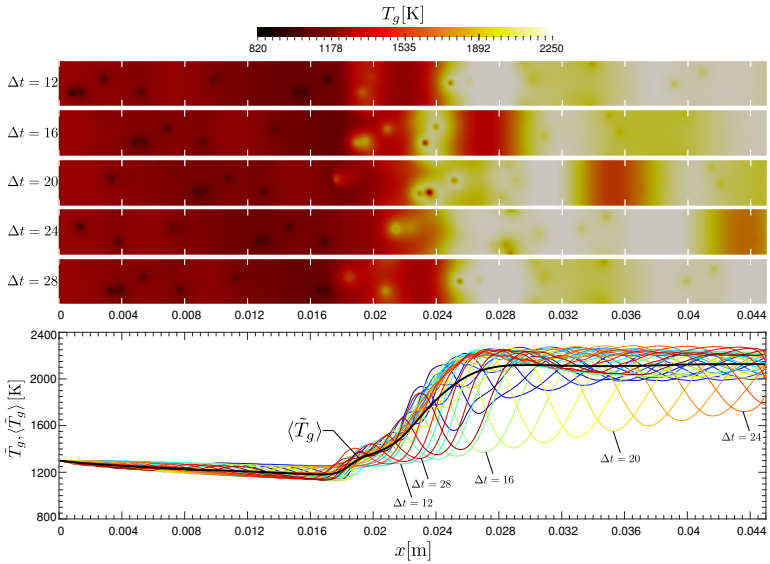

Figure 3.22: Instantaneous distribution of the gas temperature T_g for case A1 defined in Table 3.4 at five different times. The instantaneous volume averaged gas temperature $\tilde{T}_g$ is also presented along the x axis from $t = 40 - 70$ ms for every 1 ms, together with the volume and time averaged gas temperature $\langle \tilde{T}_g \rangle$ shown by a thicker black line.

reached the statistically steady state. For the A1 case, the inlet velocity is 1 m/s and the distance from inlet to outlet is 44 mm. Assuming a constant velocity through the channel with the same value as the inlet velocity, the required time for one flow through the channel is 44 ms. The upper part of Fig. 3.22 shows the 2D distribution of the gas temperature on the $x - y$ plane at $\Delta t = 12$, 16, 20, 24, and 28 ms. Figure 3.22 also includes the volume averaged temperature $\tilde{T}_g$ along the x axis for every 1 ms from $t_s = 40$ to $t = 70$ ms together with the time and volume averaged temperature $\langle \tilde{T}_g \rangle$. The 2D distribution of temperature represents different zones; particle heating (T_g decreases with small fluctuation), ignition (T_g begins to increase), and post-ignition (T_g increases with large fluctuation). It is worth noting, that in spite of the fluctuations, ignition happens at approximately the same location for different times indicating that a statistically steady state has been achieved.

3.4.3 Results and discussions

3.4.3.1 Ignition at various particle number densities

To study the effect of particle number density on ignition, first the cases A1-A3 defined in Table 3.4 were considered. From case A1 to A3, $N_{p,in}$ increases while the inlet gas temperature and velocity are identical. For cases A1 and A3, Fig. 3.23 shows the instantaneous 2D distribution of the gas temperature T_g, the heat release Q_g, and the mass fraction Y of O_2 and C_2H_2 on the $x-y$ plane. The plot with the Q_g distribution includes a projection of all computational cells containing particles in the whole domain.

Figure 3.23 shows that shortly after injection from the inlet, T_g drops in the vicinity of particles. The combined effect of multiple particles results in a significant drop of the average temperature along the streamwise direction before the ignition location is reached. Gas temperature decreases due to the energy required for particle heating. Figure 3.23 further indicates a more significant T_g-drop in the case A3 compared to A1. The larger number of particles in A3 requires a higher amount of energy for particle heating and consequently shows a more significant temperature drop in the gas phase.

As particles move forward, their temperature gradually increases by energy transfer from the gas phase. Approaching a certain temperature, particles undergo thermal decomposition and begin to release volatile gases. Figure 3.23 shows the distribution of $Y_{C_2H_2}$ as a representative of the released volatiles from coal particles. For the current high volatile bituminous coal, devolatilization begins with the release of a small amount of light gases, which then accelerates at higher temperatures when the release of tar starts. Moving further downstream, at a certain distance from the inlet for each case, volatile ignition happens where the gas temperature T_g begins to increase. At the ignition point, Q_g substantially increases and enhances T_g as well, while $Y_{C_2H_2}$ and Y_{O_2} are consumed and their values decrease.

Depending on the particle number density, the volatile flame is formed differently. In case A3 with higher number of particles, a continuous flame region was observed instead of the spherical flame around particles as in the A1 case. Due to the lower number density in the A1 case, volatiles mainly burn in diffusion flames formed around each single particle similarly to the single particle behavior observed by Farazi et al [5]. Consequently, the flame region becomes wider and more dispersed in case A1 compared to A3.

Figure 3.24(a) shows the evolution of the average gas temperature $\langle \tilde{T}_g \rangle$ for the

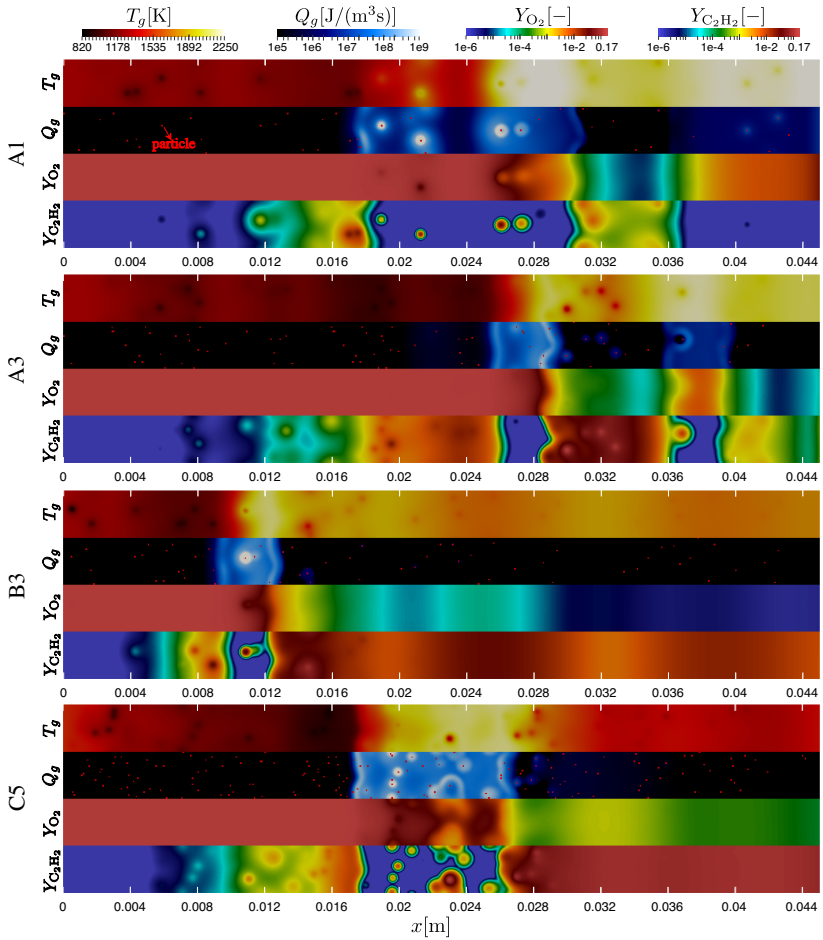

Figure 3.23: 2D distribution of gas temperature T_g, heat release Q_g, and the mass fraction Y of O_2 and C_2H_2 on the x-y plane for A1, A3, B3, C5 cases defined in Table 3.4. The plot with the Q_g distribution includes a projection of all computational cells containing particles in the whole domain.

three A cases. The ignition location is defined at the point where $\langle \tilde{T}_g \rangle$ begins to increase and marked with the vertical lines in Fig. 3.24. The ignition point is located at 16.78 mm for case A1, 20.48 mm in case A2, and 23.81 mm

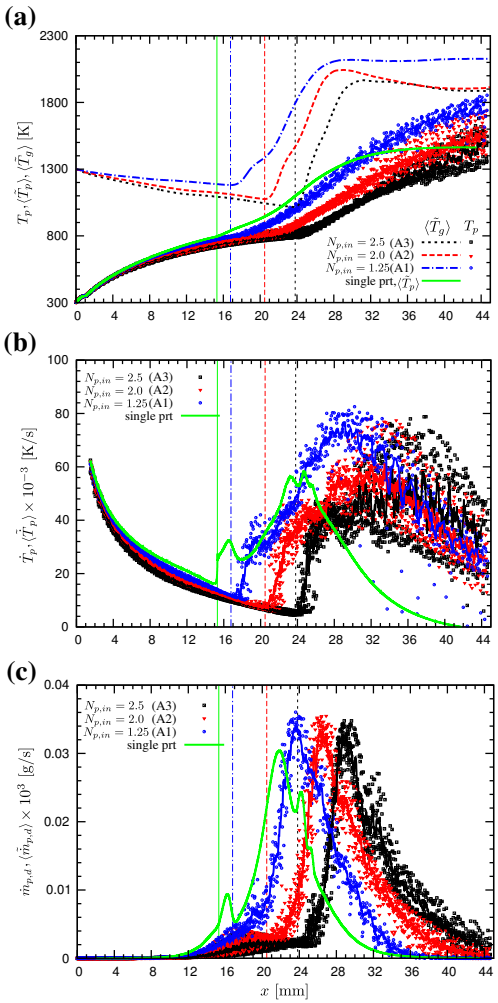

Figure 3.24: Distribution of $\langle\tilde{T}_g\rangle$, average particle temperature $\langle\tilde{T}_p\rangle$ (a), heating rate $\langle\tilde{\dot{T}}_p\rangle$ (b), and devolatilization rate $\langle\tilde{\dot{m}}_{p,d}\rangle$ (c) of A1, A2, and A3 streams. T_p, $\dot{T}_p$, and $\dot{m}_{p,d}$ of each particle in stream cases together with the single particle case are shown in (a), (b), and (c), respectively. For each case, ignition location point is marked with a vertical line.

in case A3. Figure 3.24 also shows the ignition location of a case with a single particle, which was extensively studied in our previous work [5]. In comparison with the single particle case, the ignition location in the multiple particle cases is shifted further downstream. In the denser stream, the delay of the ignition becomes even more pronounced.

Figures 3.24(a) and (b) include the evolution of the particle temperature T_p and the particle heating rate $\dot{T}_p$ for each particle, together with the time and volume averaged particle quantities shown by solid lines. As particles are injected into the channel, the particle temperature T_p gradually increases while the gas temperature $\langle \tilde{T}_g \rangle$ decreases due to the required energy for particle heating. The energy for particle heating is much higher than the heat required for the evaporation and devolatilization processes; therefore, they do not play a significant role. The denser stream has lower $\langle \tilde{T}_g \rangle$, which is caused by the higher energy demand for heating more particles. As particles are moving forward, T_p increases more slowly and $\dot{T}_g$ keeps decreasing until the ignition location. In both the single and multiple particle cases, the particle heating rate $\dot{T}_p$ decreases because the temperature difference between particles and the gas phase reduces. However, in the multiple particle cases, in particular for the denser case, particle heating becomes slower than the one observed in the single particle case. The lower $\dot{T}_p$ in the denser stream is related to the overall lower gas temperature, which is a consequence of particle-particle interaction.

After reaching a certain temperature, particles release a significant amount of volatiles into the gas phase. The released volatiles burn and heat up the gas phase. In each case, ignition happens when the heat released from the volatile flame can compensate the required energy for heating both the particles and the gas phase. It can be observed from Fig. 3.24(a) that, for each case, ignition occurs where the particle temperature T_p is around 800 K. After ignition happens, $\langle \tilde{T}_g \rangle$ begins to increase. As a result, the particle heating rate $\dot{T}_p$ significantly increases due to the higher temperature of the surrounding gas. Consequently, particle heating accelerates and particle temperature increases with a steeper slope. The peak value of $\dot{T}_p$ in case A1 exceeds the maximum $\dot{T}_p$ value of the single particle case due to the higher gas temperature surrounding the particles. Consequently, at a certain location in the A1 stream, particle temperature also exceeds the temperature of the single particle case. Further downstream, after reaching its maximum, the particle heating rate $\dot{T}_p$ decreases due to the fall in the temperature difference between the particles and the gas phase.

Figure 3.24(c) includes the evolution of the particle delolatilization rate, $\dot{m}_{p,d}$ for each stream and the single particle case. At a certain location, $\dot{m}_{p,d}$ rapidly increases as particles reach a certain temperature to release volatiles. In section 3.3.1.2, the presence of a double peak in the devolatilization rate profile of single particles was discussed, which is mostly due to the dynamics of tar as described by the CPD model. It was observed that ignition of a single particle can occur during the first volatile release or at the onset of the second, depending on the particle size and gas temperature. The double peak is still present in the cases with particle streams. However, the sharp first peak in $\dot{m}_{p,d}$ in the single particle case becomes smaller by increasing particle number density in the multiple particle cases. For denser streams, the peak value decreases and the first peak is stretched over a wider length. In addition, the denser stream shows more distance between the first and the second peak. In the A2 and A3 stream, ignition happens after the first peak is observed, while in the A1 stream, similar to the single particle case at the same thermodynamic conditions, ignition happens at the onset of the first peak. The evolution of $\dot{m}_{p,d}$ in the denser stream is similar to that observed in the corresponding single particle case which has a lower $T_{g,in}$. The first peak in $\dot{m}_{p,d}$ leads to a more pronounced surge in the $\langle \tilde{T}_g \rangle$ profile in case A1 in comparison to the A2 and A3 cases. This also affects the particle heating rate in case A1 and $\dot{T}_p$ increases with a two peak profile similar to the single particle case. In the particle stream cases, the value of $\langle \tilde{\dot{m}}_{p,d} \rangle$ at the second peak is slightly higher than the corresponding peak in the single particle case.

Figure. 3.25 shows the distribution of the average heat release rate $\langle \tilde{Q}_g \rangle$ and mass fraction $\langle \tilde{Y}_{O_2} \rangle$, and $\langle \tilde{Y}_{C_2H_2} \rangle$ in the gas phase. In each stream, $\langle \tilde{Q}_g \rangle$ and $\langle \tilde{Y}_{C_2H_2} \rangle$ show a double peak profile which is due to the double peak in the devolatilization rate. Similar to the single particle case, the ignition points are located in the vicinity of the first peak in the $\langle \tilde{Q}_g \rangle$ and $\langle \tilde{Y}_{C_2H_2} \rangle$ profiles. At the ignition location, the denser stream has a higher value of $\langle \tilde{Y}_{C_2H_2} \rangle$. The higher $\langle \tilde{Y}_{C_2H_2} \rangle$ in the denser stream forms a fuel rich mixture in the gas phase. Ignition of a richer fuel mixture rapidly reduces $\langle \tilde{Y}_{O_2} \rangle$ and sharply increases $\langle \tilde{Q}_g \rangle$. As a result, the denser stream shows higher first peak values in the $\langle \tilde{Q}_g \rangle$ profile. In the A3 stream, the first peak of $\langle \tilde{Q}_g \rangle$ becomes even higher than the second peak. This explains the presence of a more continuous flame in the A3 stream as shown in Fig. 3.23. Consequently, the denser stream undergoes a steeper increase in the gas temperature profile during ignition as shown in Fig. 3.24. After the first stage of devolatilization in the A3 case, oxygen is totally consumed and consequently the devolatilization products (C_2H_2) start to accumulate.

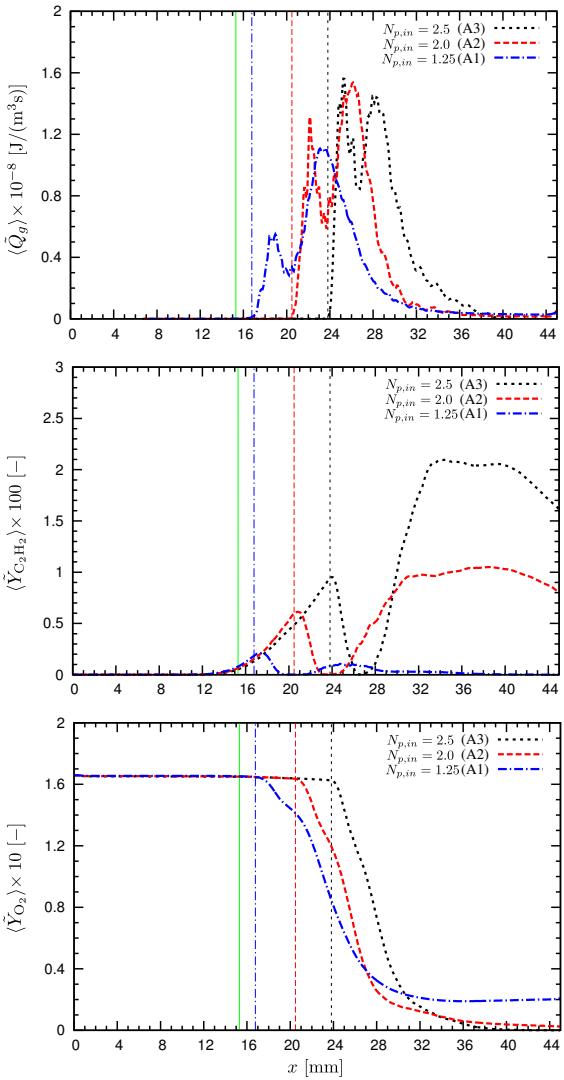

Figure 3.25: Distribution of $\langle \tilde{Q}_g \rangle$, $\langle \tilde{Y}_{C_2H_2} \rangle$, and $\langle \tilde{Y}_{O_2} \rangle$ of A1, A2, and A3 streams. The vertical green line marks the ignition location of the single particle configuration.

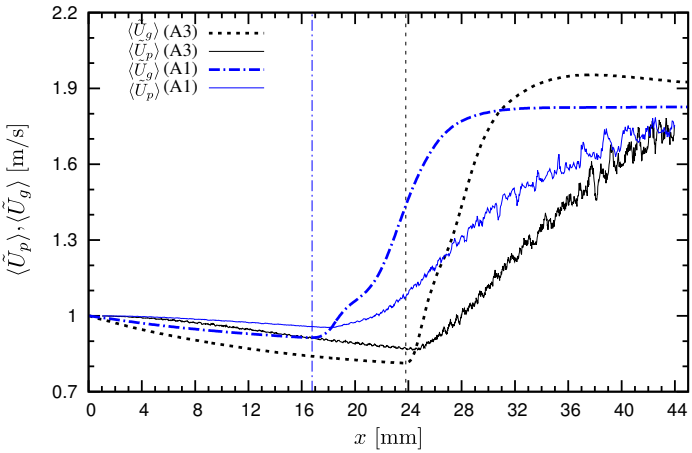

Figure 3.26: Distribution of the time and volume averaged velocity of particle and gas phase, $\langle\tilde{U}_p\rangle$ and $\langle\tilde{U}_g\rangle$ for A1 and A3 cases. For each case, ignition location is marked with a vertical line.

3.4.3.2 Velocity distribution of the particle stream

In each stream, the decrease of the gas temperature due to particle heating alters the distribution of the flow field velocity. Figure 3.26 illustrates the time and volume averaged velocity of particle and gas phase, $\langle\tilde{U}_g\rangle$ and $\langle\tilde{U}_p\rangle$, for the A1 and A3 cases. In both cases, the velocity profile shows a similar trend to that observed for $\langle\tilde{T}_g\rangle$. In each case, $\langle\tilde{U}_g\rangle$ and $\langle\tilde{U}_p\rangle$ decrease moving from the inlet towards the ignition location due to the decrease of gas-phase temperature caused by particle heating. Subsequently, due to the release of heat and temperature increase, $\langle\tilde{U}_g\rangle$ and $\langle\tilde{U}_p\rangle$ begin to increase at the location where ignition occurs. In comparison to A1, the variation in $\langle\tilde{U}_g\rangle$ and $\langle\tilde{U}_p\rangle$ shows a steeper slope in the A3 case.

Variations in the gas velocity $\langle\tilde{U}_g\rangle$ induce changes of the drag force on particles. Consequently, the particle velocity $\langle\tilde{U}_p\rangle$ changes as well. In all cases, particles decelerate/accelerate at a smaller rate than the gas phase. Before ignition, when the flow field decelerates, $\langle\tilde{U}_p\rangle$ has higher values than $\langle\tilde{U}_g\rangle$. After ignition, as the flow field accelerates, $\langle\tilde{U}_p\rangle$ becomes lower than $\langle\tilde{U}_g\rangle$. Among the A cases, the denser stream shows higher mean slip velocity, which is more than 50% of the prescribed velocity at the inlet. Non homogenous gas and particle velocity affect the distribution of the particle number density. In each

stream, in the regions with $\frac{\partial\langle\tilde{U}_p\rangle}{\partial x} < 0$, the particle number density increases, while in the regions with $\frac{\partial\langle\tilde{U}_p\rangle}{\partial x} > 0$, the particle distribution becomes more dispersed and the particle number density decreases.

3.4.3.3 Ignition delay time of the particle stream

To relate the ignition location to an ignition delay time, a Lagrangian time at the location x is computed as

$$t_{Lag}(x) = \int_0^x \frac{1}{\langle\tilde{U}_g(\xi)\rangle} d\xi. \tag{3.22}$$

For example, among the A cases, the same location corresponds to later times in denser streams due to the different evolution of the gas-phase velocity in the different cases.

The ignition delay time τ_{ign} is computed for all cases using Eq. (3.22) as

$$\tau_{ign} = t_{Lag}(x_{ign}) = \int_0^{x_{ign}} \frac{1}{\langle\tilde{U}_g(\xi)\rangle} d\xi, \tag{3.23}$$

where x_{ign} is the ignition location point. In addition, the ignition delay time similar to the approach typically used by experimentalists (Liu et al [47]) was also computed, assuming a constant velocity in mapping the measured ignition location to the ignition time. Assuming a constant velocity everywhere, an ignition delay time τ'_{ign} is also calculated as

$$\tau'_{ign} = \frac{x_{ign}}{U_{g,in}}. \tag{3.24}$$

The computed ignition delay time using both Eqs. (3.23) and (3.24) is shown in Fig. 3.27 as a function of the particle number density prescribed at the inlet. Comparing the multiple particle cases to the single particle case shows that increasing particle number density increases ignition delay time. In the A cases, increasing the inlet particle number density up to 3×10^8 increases ignition delay time by a factor of two compared to that observed in the single particle ignition. In each stream, the constant velocity assumption (Eq. (3.24)) causes an underestimation of the ignition delay time in comparison to the ignition delay time computed from the Lagrangian time.

Fig. 3.27 also shows the ignition delay time for the C cases with inlet gas

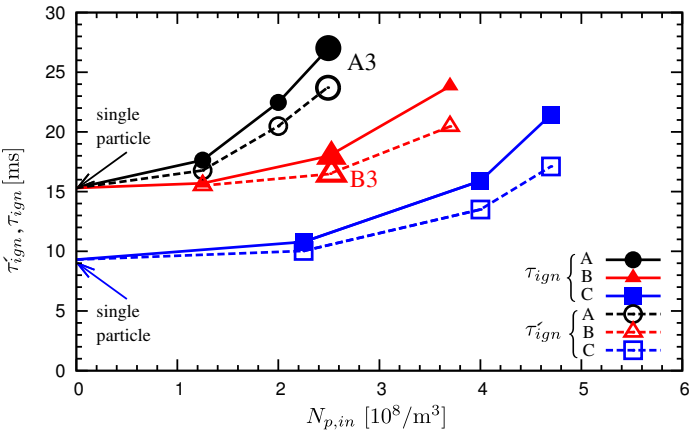

Figure 3.27: Ignition delay time versus particle number density $N_{p,in}$ at the inlet for all cases defined in Tab. 3.4.

temperature of 1500 K, which is 200 K higher than that of the A cases. Increasing particle number density in the C streams delays ignition less than for the A cases. The ignition location in C5 is similar to the A1 case, however the volatile flame is very different. As shown in Fig. 3.23, the volatile flame in C5 consists of both spherical flame around particles and a clear continuous flame.

Fig. 3.27 also shows the ignition delay time for the B cases with a different injection velocity than that of the A cases. In comparison to the A cases, increasing particle number density increases ignition delay time less in the B cases. In spite of having the same prescribed gas temperature and particle number density, it is worth noting that the ignition delay time for the B cases is significantly lower than the one observed in the A cases. In the A3 and B3 cases, ignition happens earlier in B3. A further detailed analysis on the effect of the inlet velocity on stream ignition is provided in the following section.

3.4.3.4 Ignition at various inlet velocities

To perform a detailed comparison between the A and B cases, simulations B3 and A3 are considered, marked with bigger symbols in Fig. 3.27. The prescribed inlet velocity in the B3 case is half of the one of the A3 case, while the particle number density and the gas temperature at the inlet are the same

for both cases. Due to the lower velocity in the B3 case, ignition happens at a location closer to the inlet in comparison to the A3 case. Assuming a negligible effect of the slip velocity between the flow and the particles, one would have expected an ignition location in B3 at half the distance of that observed in the A3 case, and consequently the same ignition delay time as the one in A3. However, it was observed that ignition happens earlier than expected. Besides having a faster ignition, the B3 stream shows also a different shape of the volatile flame in comparison to A3. Figure. 3.23 illustrates that the B3 stream shows the presence of spherical flames around particles, which are not very evident in the A3 case.

For both the B3 and A3 cases, average quantities are plotted versus t_{Lag} in Fig. 3.28. During the particle heating phase, before the onset of ignition in B3, the drop of $\langle \tilde{T}_g \rangle$ and rise of $\langle \tilde{T}_p \rangle$ for both cases are very similar. In addition, Fig. 3.28 also shows that before ignition, the devolatilization rate and mass fraction of CO in the B3 case evolve very similarly to the A3 case. Figure 3.28 includes insets with log-scale plots and the variance of each quantity for a short time interval before ignition. In comparison to the B3 stream, each quantity evolves with larger variance in the A3 stream. The larger variance leads to locally higher maximum and lower minimum values in the gas temperature. It is worth noting that at lower temperatures, the ignition process is extremely sensitive to variations in the gas temperature as shown in our previous work [5].

To understand the difference between the variances in the B3 and A3 cases, selected fields were analyzed in the $y-z$ plane corresponding to the Lagrangian time $t_{Lag} = 16$, 17, and 18 ms. These Lagrangian times are marked in Fig 3.28 by vertical lines. Figure 3.29 shows a scatter plot of CO and gas temperature T_g on the $y - z$ plane corresponding to $t_{Lag} = 16$, 17, and 18 ms. The upper part of each plot belongs to the A3 case, while the lower part represents the B3 case. To facilitate the comparison, the Y_{CO} axis is reversed for the B3 case. The color of the symbols indicates the heat release rate Q_g. Additionally, T_g and Y_{CO} are interpolated at the particle location and are included in Fig. 3.29 by cross symbols for the particles located within a distance less than two particle diameters from the evaluated plane. The color of the cross indicates the value of the slip velocity between the particle and the gas-phase at the particle location.

At $t_{Lag} = 16$ ms, particles are located at points with the highest amount of fuel and lowest temperature. The rest of the points shown in the figure belongs to the film around the particles. In the film, the released volatiles from particles

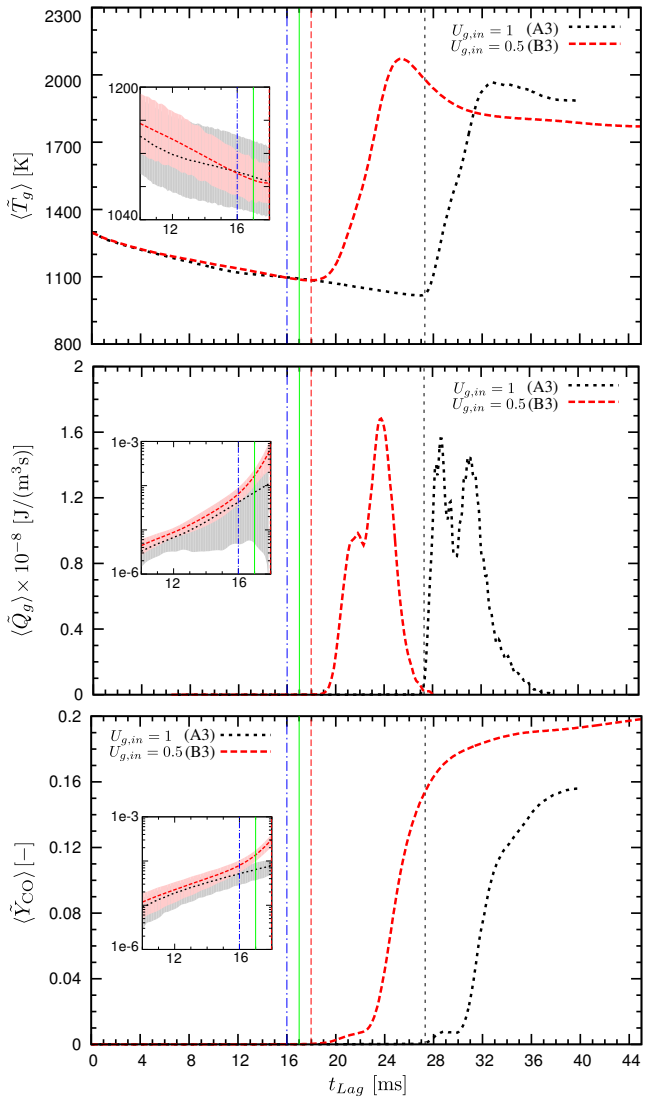

Figure 3.28: Evolution of the time and volume averaged quantities in A3 and B3 cases defined in Tab. 3.4 including inset plots to represent variance of each quantity.

diffuse into the surroundings and increase Y_{CO}, while the energy sink due to particle heating decreases T_g. The points farther away from the particles have higher temperature and lower fuel concentration. At the particle locations, the heat release Q_g is very low due to the low temperature ($T_g < 1000$ K). On the other hand, heat release shows higher values at points with a gas temperature higher than 1000 K, which are located in the surrounding of the particles. It is interesting to observe that the A3 case, which overall ignites later that B3, is characterized by larger local values of heat release compared to the B3 case for the Lagrangian time $t_{Lag} = 16$ ms. However, it is found that at subsequent Lagrangian times (or equivalently, downstream locations) the heat release in the B3 cases overcomes that in the A3 case and ignition occurs for the B3 case. This is due to the larger scatter, i.e., larger variance, of the former. In the A3 case, there is a significant number of points with low temperature, where the heat released (observed at 16 ms) tends to diffuse, eventually preventing ignition.

The increased variance and scatter in the A3 case compared to B3 are related to the larger slip velocity observed for the former case. From the analysis of the slip velocity values shown in Fig. 3.29, it is evident that the lowest values of temperature and CO mass fraction at the particle locations in case A3 correlate with high values of the slip velocity.

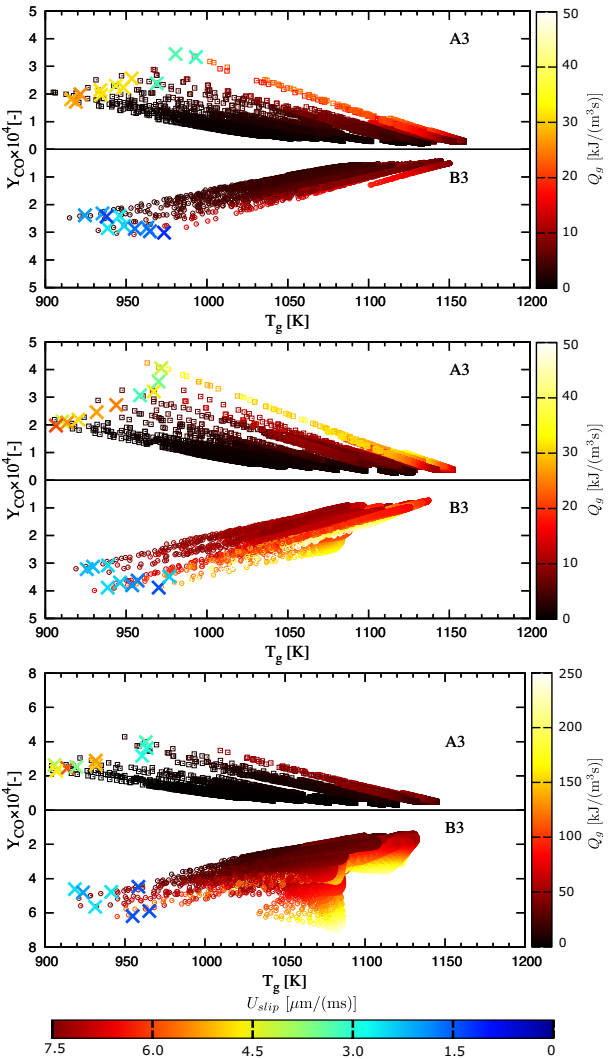

Figure 3.29: Scatter plot of the T_g and Y_{CO} for every 1 ms in the $y-z$ plane corresponding to the Lagrangian time of $t_{Lag} = 16$(top), 17(middle), 18(bottom) ms in A3 and B3 streams. The color of the symbols indicates the heat release rate Q_g. The cross symbols belong to the interpolated gas quantities at the particle location. The color of the cross symbols indicates the slip velocity U_{slip}.

4 Conclusions

In the current study, ignition and combustion of coal particles are numerically studied in different conditions and configurations. Numerical results are analyzed to understand the interactions between different phenomena and to explain different ignition and combustion of coal particles under conventional and oxy-fuel atmospheres. Detailed simulations and discussions for char burnout and devolatilization phases are provided in the second and third chapters, respectively.

In the second chapter, combustion of single char particles in a laminar flow field is investigated with spatially and chemically resolved simulations. The mass and energy exchanges between the solid particle and the gas phase during combustion under oxy-atmosphere are studied and compared with the corresponding cases in air. The lower carbon consumption rate in oxy-atmosphere was found to result from a higher activity of the reaction $O_2 + H \rightarrow OH + O$, which consumes O_2 in the gas phase faster leading to a shortage of oxygen for the surface oxidation reaction. The lower heat release from homogeneous reactions in oxy-atmosphere was explained by the lower carbon consumption rate. Furthermore, the reduction of CO_2 with hydrogen radicals leads to a substantial formation of CO in the gas phase close to the particle surface. It was shown that the combination of a lower heat release and higher specific heat yield lower temperatures in oxy- compared to the air atmosphere. Furthermore, it was shown that for the baseline cases studied, convective and diffusive Damköhler numbers are always greater than one, which emphasizes the important role of transport in the current study. The interactions between transport and chemistry were studied based on a set of simulations with varying the particle Reynolds number. It was observed that varying the particle Reynolds number by particle size yields very different results than by relative velocity, which is because of the simultaneous change in convective and diffusive Damköhler numbers. Further studies varying the particle Reynolds number by velocity were carried out to study cases with a substantial decrease in the convective Damköhler number. It was found that the fuel consumption rate increases due to the higher Reynolds numbers and better oxygen supply to the particle up to the point where the Damköhler number becomes so small that the resulting temperature decrease leads to a

substantial attenuation of the fuel consumption rate.

In addition, the impact of the surface reactions on the gas flow around a char particle is investigated at various gas compositions and Reynolds numbers. The surface reactions yield a Stefan flow velocity, from the particle surface towards the gas phase, which modifies the flow pattern around the particle. In order to quantify the impact of surface reactions, a dimensionless Stefan velocity is considered by dividing the surface-averaged Stefan velocity to the inlet velocity. The dimensionless Stefan velocity has the highest value at the gas flow with the lowest relative Reynolds number and the highest oxygen content. The drag coefficient, is computed for each reactive particle and the corresponding non-reactive case. The presence of reactions reduces the value of the drag coefficient. The drag reduction due to combustion is more pronounced at higher oxygen concentrations and lower Reynolds numbers. The ratio of the drag coefficient of reactive particle to non-reactive, reveals an inverse relation with the value of the dimensionless Stefan velocity. In an attempt to fit the data, an empirical relation between the drag reduction and the dimensionless Stefan velocity is extracted. This correlation can be used in large scale oxy-coal combustion simulations with the point particle assumption to account for the Stefan convection and modify the acting drag force on the particles.

In the third chapter, particle ignition is investigated using the CPD method coupled with detailed chemistry within an Euler-Lagrange framework. A large set of numerical simulations based on detailed sub-models for the description of coal particle ignition in a hot gas atmosphere has been performed. The numerical results were validated against a series of experiments in a laminar entrained flow reactor. The evolution of the volatile flame, resulting from the ignition of the volatile gas released by the particle, is described. A double peek profile in the time evolution of tar release rate is observed and the effect on the gas-phase combustion is assessed. It is found that ignition can be strongly influenced by the presence of the two distinct peaks. In particular, it is observed that ignition occurs with the appearance of the first peak of the devolatilization rate for high gas temperature and large particles, while it is delayed until the second peak for low values of the gas temperature and small particles. If ignition occurs during the first devolatilization peak, two distinct peaks are also observed in the evolution of the maximum gas-phase temperature and species concentration. Coal ignition in mixtures with significant amounts of CO_2 diluent is slower compared to the case in standard air environment. It is found that this difference is more significant approaching

lower initial gas temperature and that the primary effect of CO_2 on ignition originates from its tendency to suppress radical formation.

In addition to the single particle, the ignition process of particle streams in oxy-atmosphere has also been simulated. The ignition delay time has been determined for different cases of varying particle number density, gas temperature, and injection velocity. While many fundamental experiments study ignition of coal particles in a cold carrier gas injected into a hot coflow, the current configuration seeds coal particles directly into a hot oxidizer stream. Therefore, this configuration is appropriate to study ignition in regions of the burner with fast mixing time in comparison to the particle heating time. Eliminating the coflow stream in the current configuration, we observed differences with respect to some fundamental experiments using hot coflow, where ignition delay time first decreases until it reaches a minimum and then increases by increasing particle number density. In the present configuration, we observed that increasing particle number density shifts the ignition location downstream and increases ignition delay time. This is mainly caused by the lower gas temperature due to the higher energy required for particle heating. Increasing the particle number density affects the volatile flame shape, devolatilization rate, velocity profile, and particle distribution. The generated data can be used to empirically model the influence of the particle-particle interactions on the ignition delay time. Finally, we found that at the same gas temperature and particle number density, faster streams show longer ignition delay times, which originates from larger variances in the gas temperature and composition. Larger variances are caused by higher particle slip velocity in the faster stream. Higher particle slip velocities lead to a locally low volatile concentration and low temperature, and consequently increase ignition delay time.

Bibliography

[1] D.D. Toporov, Combustion of Pulverised Coal in a Mixture of Oxygen and Recycled Flue Gas, Elsevier, 1 edition, 2014.

[2] L. Chen, S.Z. Yong, A.F. Ghoniem, Oxy-fuel combustion of pulverized coal: Characterization, fundamentals, stabilization and CFD modeling, Progress in Energy and Combustion Science 38 (2012) 156–214.

[3] S. Farazi, M. Sadr, S. Kang, M. Schiemann, N. Vorobiev, V. Scherer, H. Pitsch, Resolved simulations of single char particle combustion in a laminar flow field, Fuel 201 (2017) 15 – 28.

[4] S. Farazi, T. Sayadi, H. Pitsch, Numerical analysis of the drag force acting on the reactive char particle under oxy-fuel condition, Proceedings of the China National Symposium on Combustion (2016).

[5] S. Farazi, A. Attili, S. Kang, H. Pitsch, Numerical study of coal particle ignition in air and oxy-atmosphere, Proceedings of the Combustion Institute (In Press).

[6] S. Farazi, J. Hinrichs, M. Davidovic, T. Falkenstein, M. Bode, S. Kang, A. Attili, H. Pitsch, Numerical investigation of coal particle stream ignition in oxy-atmosphere, Fuel (In Press).

[7] T. Maffei, R. Khatami, S. Pierucci, T. Faravelli, E. Ranzi, Y.A. Levendis, Experimental and modeling study of single coal particle combustion in O_2/N_2 and Oxy-fuel (O_2/CO_2) atmospheres, Combustion and Flame 160 (2013) 2559–2572.

[8] E.S. Hecht, C.R. Shaddix, A. Molina, B.S. Haynes, Effect of CO_2 gasification reaction on oxy-combustion of pulverized coal char, Proceedings of the Combustion Institute 33 (2011) 1699–1706.

[9] E.S. Hecht, C.R. Shaddix, M. Geier, A. Molina, B.S. Haynes, Effect of CO_2 and steam gasification reactions on the oxy-combustion of pulverized coal char, Combustion and Flame 159 (2012) 3437–3447.

[10] C.R. Shaddix, F. Holzleithner, M. Geier, B.S. Haynes, Numerical assessment of Tognotti determination of CO_2/CO production ratio during char oxidation, Combustion and Flame 160 (2013) 1827–1834.

[11] L. Tognotti, J.P. Longwell, A.F. Sarofim, The products of the high temperature oxidation of a single char particle in an electrodynamic balance, Symposium (International) on Combustion 23 (1991) 1207–1213.

[12] E.S. Hecht, C.R. Shaddix, J.S. Lighty, Analysis of the errors associated with typical pulverized coal char combustion modeling assumptions for oxy-fuel combustion, Combustion and Flame 160 (2013) 1499–1509.

[13] W. Nusselt, Zeitschrift des Vereins Deutscher Ingenieure 68 (1924) 124–128.

[14] S. Burke, T. Schumann, Kinetics of a Type of Heterogeneous Reactions The Mechanism of Combustion of Pulverized Fuel, Industrial & Engineering Chemistry 23 (1931) 406–413.

[15] M. Kestel, P. Nikrityuk, O. Hennig, C. Hasse, Numerical study of the partial oxidation of a coal particle in steam and dry air atmospheres, IMA Journal of Applied Mathematics 77 (2012) 32–46.

[16] A. Richter, P.A. Nikrityuk, M. Kestel, Numerical investigation of a chemically reacting carbon particle moving in a hot O_2/CO_2 atmosphere, Industrial & Engineering Chemistry Research 52 (2013) 5815–5824.

[17] P.A. Bejarano, Y.A. Levendis, Single-coal-particle combustion in O_2/N_2 and O_2/CO_2 environments, Combustion and Flame 153 (2008) 270–287.

[18] S.Y. Cho, R.A. Yetter, F.L. Dryer, A Computer Model for One-Dimensional Mass and Energy Transport in and around Chemically Reacting Particles, Including Complex Gas-Phase Chemistry, Multicomponent Molecular Diffusion, Surface Evaporation, and Heterogeneous Reaction, Journal of Computational Physics 102 (1992) 160–179.

[19] J.C. Lee, R.A. Yetter, F.L. Dryer, Numerical Simulation of Laser Ignition of an Isolated Carbon Particle in Quiescent Environment, Combustion and Flame 105 (1996) 591–599.

[20] J.C. Lee, R.A. Yetter, F.L. Dryer, Transient Numerical Modeling of Carbon Particle Ignition and Oxidation, Combustion and Flame 101 (1995) 387–398.

[21] J.C. Lee, A. Tomboulides, S. Orszag, R.A. Yetter, F.L. Dryer, A transient two-dimensional chemically reactive flow model: Fuel particle combustion in a nonquiescent environment, Symposium (International) on Combustion 26 (1996) 3959–3065.

[22] J.J. Murphy, C.R. Shaddix, Combustion kinetics of coal chars in oxygen-enriched environments, Combustion and Flame 144 (2006) 710–729.

[23] M. Schiemann, N. Vorobiev, V. Scherer, Stereoscopic pyrometer for char combustion characterization, Applied Optics 54 (2015) 1097–1108.

[24] N. Vorobiev, M. Geier, M. Schiemann, V. Scherer, Experimentation for char combustion kinetics measurements: Bias from char preparation, Fuel Processing Technology 151 (2016) 155–165.

[25] A. Zolin, A. Jensen, L.S. Pedersen, K. Dam-Johansen, P. Tørslev, A comparison of coal char reactivity determined from thermogravimetric and laminar flow reactor experiments, Energy & fuels 12 (1998) 268–276.

[26] Y. Chen, C. Sheng, Modeling of a single char particle burning in oxygen-enriched O_2/N_2 and O_2/CO_2 environment with single film model, Fuel 184 (2016) 905–914.

[27] J. Yu, K. Zhou, W. Ou, Effects of Stefan flow and CO oxidation on char particle combustion in O_2/CO_2 atmosphere, Fuel 106 (2013) 576–585.

[28] H. Tolvanen, R. Raiko, An experimental study and numerical modeling of combusting two coal chars in a drop-tube reactor: a comparison between N_2/O_2, CO_2/O_2, and $N_2/CO_2/O_2$ atmospheres, Fuel 124 (2014) 190–201.

[29] Y. Niu, C.R. Shaddix, A sophisticated model to predict ash inhibition during combustion of pulverized char particles, Proceedings of the Combustion Institute 35 (2015) 561–569.

[30] M. Schiemann, M. Geier, C.R. Shaddix, N. Vorobiev, V. Scherer, Determination of char combustion kinetics parameters: Comparison of point detector and imaging-based particle-sizing pyrometry, Review of Scientific Instruments 85 (2014).

[31] D. Kim, S. Choi, C.R. Shaddix, M. Geier, Effect of CO_2 gasification reaction on char particle combustion in oxy-fuel conditions, Fuel 120 (2014) 130–140.

[32] H. Düdder, A. Wütscher, N. Vorobiev, M. Schiemann, V. Scherer, M. Muhler, Oxidation characteristics of a cellulose-derived hydrochar in thermogravimetric and laminar flow burner experiments, Fuel Processing Technology 148 (2016) 85–90.

[33] M. Geier, C.R. Shaddix, K.A. Davis, H.S. Shim, On the use of single-film models to describe the oxy-fuel combustion of pulverized coal char, Applied Energy 93 (2012) 675–679.

[34] P. Graeser, M. Schiemann, Char particle emissivity of two coal chars in oxy-fuel atmospheres, Fuel 183 (2016) 405–413.

[35] J. Köser, L.G. Becker, N. Vorobiev, M. Schiemann, V. Scherer, B. Böhm, A. Dreizler, Characterization of single coal particle combustion within oxygen-enriched environments using high-speed OH-PLIF, Applied Physics B 121 (2015) 459–464.

[36] M. Schiemann, S. Haarmann, N. Vorobiev, Char burning kinetics from imaging pyrometry: Particle shape effects, Fuel 134 (2014) 53–62.

[37] W. Prationo, L. Zhang, Influence of steam on ignition of Victorian brown coal particle stream in oxy-fuel combustion: In-situ diagnosis and transient ignition modelling, Fuel 181 (2015) 1203–1213.

[38] M. Schiemann, V. Scherer, S. Wirtz, Optical coal particle temperature measurement under oxy-fuel conditions: Measurement methodology and initial results, Chemical Engineering and Technology 32 (2009) 2000–2004.

[39] A.P. Bejarano, A.L. Yiannis, Combustion of Coal Chars in Oxygen-Enriched Atmospheres, Combust. Sci. Technol. 179 (2007) 1569–1587.

[40] J. Riaza, R. Khatami, Y.A. Levendis, L. Álvarez, M.V. Gil, C. Pevida, F. Rubiera, J.J. Pis, Combustion of single biomass particles in air and in oxy-fuel conditions, Biomass and Bioenergy 64 (2014) 162–174.

[41] J. Riaza, R. Khatami, Y.A. Levendis, L. Álvarez, M.V. Gil, C. Pevida, F. Rubiera, J.J. Pis, Single particle ignition and combustion of anthracite, semi-anthracite and bituminous coals in air and simulated oxy-fuel conditions, Combustion and Flame 161 (2014) 1096–1108.

[42] T. Joutsenoja, J. Stenberg, R. Hernberg, M. Aho, Pyrometric measurement of the temperature and size of individual combusting fuel particles., Applied optics 36 (1997) 1525–1535.

[43] T. Joutsenoja, J. Saastamoinen, M. Aho, R. Hernberg, Effects of pressure and oxygen concentration on the combustion of different coals, Energy & fuels 13 (1999) 130–145.

[44] M. Schiemann, N. Vorobiev, Stereoscopic Camera-Based Investigation of Pulverized Solid Fuel Combustion - particle temperature, shape and burning rates, European Combustion Meeting (2015) 1–6.

[45] N. Vorobiev, M. Schiemann, Determination of char combustion kinetics of torrefied biomass by use of stereoscopic pyrometry, The 40th International Technical Conference on Clean Coal & Fuel Systems (2015) 550–561.

[46] D.M. Grant, R.J. Pugmire, T.H. Fletcher, A.R. Kerstein, Chemical model of coal devolatilization using percolation lattice statistics, Energy and Fuels 3 (1989) 175–186.

[47] Y. Liu, M. Geier, A. Molina, C.R. Shaddix, Pulverized coal stream ignition delay under conventional and oxy-fuel combustion conditions, International Journal of Greenhouse Gas Control 5 (2011) S36–S46.

[48] H. Yang, S. Li, T.H. Fletcher, M. Dong, W. Zhou, Simulation of the Evolution of Pressure in a Lignite Particle during Pyrolysis, Energy and Fuels 28 (2014) 3511–3518.

[49] K. Luo, J. Xing, Y. Bai, J. Fan, Universal Devolatilization Process Model for Numerical Simulations of Coal Combustion, Energy and Fuels 31 (2017) 6525–6540.

[50] Y. Chen, S. Mori, W.P. Pan, Studying the mechanisms of ignition of coal particles by TG-DTA, Thermochimica Acta 275 (1996) 149–158.

[51] H. Song, G. Liu, J. Wu, Pyrolysis characteristics and kinetics of low rank coals by distributed activation energy model, Energy Conversion and Management 126 (2016) 1037–1046.

[52] D. Magalhães, F. Kazanç, A. Ferreira, M. Rabaçal, M. Costa, Ignition behavior of Turkish biomass and lignite fuels at low and high heating rates, Fuel 207 (2017) 154 –164.

[53] A. Molina, C.R. Shaddix, Ignition and devolatilization of pulverized bituminous coal particles during oxygen/carbon dioxide coal combustion, Proceedings of the Combustion Institute 31 (2007) 1905–1912.

[54] C.R. Shaddix, A. Molina, Particle imaging of ignition and devolatilization of pulverized coal during oxy-fuel combustion, Proceedings of the Combustion Institute 32 (2009) 2091–2098.

[55] R. Khatami, C. Stivers, Y.A. Levendis, Ignition characteristics of single coal particles from three different ranks in O_2/N_2 and O_2/CO_2 atmospheres, Combustion and Flame 159 (2012) 3554–3568.

[56] J. Köser, L.G. Becker, A.K. Goßmann, B. Böhm, A. Dreizler, Investigation of ignition and volatile combustion of single coal particles within oxygen-enriched atmospheres using high-speed OH-PLIF, Proceedings of the Combustion Institute 36 (2017) 2103–2111.

[57] B. Goshayeshi, J. Sutherland, A comparison of various models in predicting ignition delay in single-particle coal combustion, Combustion and Flame 161 (2014).

[58] G. Tufano, O. Stein, A. Kronenburg, A. Frassoldati, T. Faravelli, L. Deng, A. Kempf, M. Vascellari, C. Hasse, Resolved flow simulation of pulverized coal particle devolatilization and ignition in air- and O_2/CO_2-atmospheres, Fuel 186 (2016) 285–292.

[59] M. Muto, K. Yuasa, R. Kurose, Numerical simulation of ignition in pulverized coal combustion with detailed chemical reaction mechanism, Fuel 190 (2017) 136–144.

[60] S. Jimenez, C. Gonzalo-Tirado, Properties and relevance of the volatile flame of an isolated coal particle in conventional and oxy-fuel combustion conditions, Combustion and Flame 176 (2017) 94–103.

[61] J. Zhang, K.E. Kelly, E.G. Eddings, J.O.L. Wendt, Ignition in 40 kW co-axial turbulent diffusion oxy-coal jet flames, Proceedings of the Combustion Institute 33 (2011) 3375–3382.

[62] Y. Qiao, L. Zhang, E. Binner, M. Xu, C.Z. Li, An investigation of the causes of the difference in coal particle ignition temperature between combustion in air and in O_2/CO_2, Fuel 89 (2010) 3381–3387.

[63] T. Kiga, S. Takano, N. Kimura, K. Omata, M. Okawa, T. Mori, M. Kato, Characteristics of pulverized-coal combustion in the system of oxygen/recycled flue gas combustion, Energy Conversion and Management 38 (1997) S129–S134.

[64] S.P. Khare, T.F. Wall, A.Z. Farida, Y. Liu, B. Moghtaderi, R.P. Gupta, Factors influencing the ignition of flames from air-fired swirl pf burners retrofitted to oxy-fuel, Fuel 87 (2008) 1042–1049.

[65] C. Galletti, E. Giacomazzi, S. Giammartini, G. Coraggio, L. Tognotti, Analysis of coal combustion in oxy-fuel conditions through pulsed feeding experiments in an entrained flow reactor, Energy and Fuels 27 (2013) 2732–2740.

[66] C. Liu, Q. Zhu, Z. Li, Q. Zong, X. Zhang, Z. Chen, Influence of different oil feed rate on bituminous coal ignition in a full-scale tiny-oil ignition burner, Fuel 7 (2013) 406–412.

[67] W. Li, K. Cen, C. Zheng, J. Zhou, X. Cao, Induction-heating ignition of pulverized coal stream, Fuel 83 (2004) 2103–2107.

[68] L. Zhengqi, S. Rui, C. Lizhe, W. Zhixin, W. Shaohua, Q. Yukun, Effect of primary air flow types on particle distributions in the near swirl burner region, Fuel 81 (2002) 829–835.

[69] Y. Yuan, S. Li, G. Li, N. Wu, Q. Yao, The transition of heterogeneous-homogeneous ignitions of dispersed coal particle streams, Combustion and Flame 161 (2014) 2458–2468.

[70] K. Annamalai, S.C. Ramalingam, Group combustion of char/carbon particles, Combustion and Flame 70 (1987) 307–332.

[71] X. Du, C. Gopalakrishnan, K. Annamalai, Ignition and combustion of coal particle streams, Fuel 74 (1995) 487–494.

[72] S. Wang, H. Lu, Y. Zhao, R. Mostofi, H. Young Kim, L. Yin, Numerical study of coal particle cluster combustion under quiescent conditions, Chemical Engineering Science 62 (2007) 4336–4347.

[73] Y. Zhao, H.Y. Kim, S.S. Yoon, Transient group combustion of the pulverized coal particles in spherical cloud, Fuel 86 (2007) 1102–1111.

[74] L. Qiao, Transient flame propagation process and flame-speed oscillation phenomenon in a carbon dust cloud, Combustion and Flame 159 (2012) 673–685.

[75] G.L. Tufano, O.T. Stein, B. Wang, A. Kronenburg, M. Rieth, A.M. Kempf, Coal particle volatile combustion and flame interaction. Part I : Characterization of transient and group effects, Fuel 229 (2018) 262–269.

[76] A. Silaen, T. Wang, Effect of turbulence and devolatilization models on coal gasification simulation in an entrained-flow gasifier, International Journal of Heat and Mass Transfer 53 (2010) 2074–2091.

[77] R. Jovanovic, A. Milewska, B. Swiatkowski, A. Goanta, H. Spliethoff, Numerical investigation of influence of homogeneous/heterogeneous ignition/combustion mechanisms on ignition point position during pulverized coal combustion in oxygen enriched and recycled flue gases atmosphere, International Journal of Heat and Mass Transfer 54 (2011) 921–931.

[78] Y.S. Shen, B.Y. Guo, A.B. Yu, P. Zulli, A three-dimensional numerical study of the combustion of coal blends in blast furnace, Fuel 88 (2009) 255–263.

[79] M. Vascellari, H. Xu, C. Hasse, Flamelet modeling of coal particle ignition, Proceedings of the Combustion Institute 34 (2013) 2445–2452.

[80] M. Rieth, F. Proch, M. Rabaçal, B.M. Franchetti, F. Cavallo Marincola, A.M. Kempf, Flamelet LES of a semi-industrial pulverized coal furnace, Combustion and Flame 173 (2016) 39–56.

[81] M. Rieth, A.G. Clements, M. Rabaçal, F. Proch, O.T. Stein, A.M. Kempf, Flamelet LES modeling of coal combustion with detailed devolatilization by directly coupled CPD, Proceedings of the Combustion Institute 36 (2017) 2181–2189.

[82] M. Rieth, A.M. Kempf, A. Kronenburg, O.T. Stein, Carrier-phase DNS of pulverized coal particle ignition and volatile burning in a turbulent mixing layer, Fuel 212 (2018) 364–374.

[83] N. Hashimoto, R. Kurose, S.M. Hwang, H. Tsuji, H. Shirai, A numerical simulation of pulverized coal combustion employing a tabulated-devolatilization-process model (TDP model), Combustion and Flame 159 (2012) 353–366.

[84] J. Watanabe, T. Okazaki, K. Yamamoto, K. Kuramashi, A. Baba, Large-eddy simulation of pulverized coal combustion using flamelet model, Proceedings of the Combustion Institute 36 (2017) 2155–2163.

[85] J. Watanabe, K. Yamamoto, Flamelet model for pulverized coal combustion, Proceedings of the Combustion Institute 35 (2015) 2315–2322.

[86] X. Wen, Y. Luo, K. Luo, H. Jin, J. Fan, LES of pulverized coal combustion with a multi-regime flamelet model, Fuel 188 (2017) 661–671.

[87] Y. Bai, K. Luo, K. Qiu, J. Fan, Numerical investigation of two-phase flame structures in a simplified coal jet flame, Fuel 182 (2016) 944–957.

[88] M. Ruiz, K. Annamalai, T. Dahdah, An experimental study on group ignition of coal particle streams, Heat and Mass Transfer in Fires and Combustion Systems 148 (1990) 19–26.

[89] T. Poinsot, D. Veynante, Theoretical and Numerical Combustion, R. T. Edwards, Inc., 2 edition, 2005.

[90] G. Blanquart, P. Pepiot-Desjardins, H. Pitsch, Chemical mechanism for high temperature combustion of engine relevant fuels with emphasis on soot precursors, Combustion and Flame 156 (2009) 588–607.

[91] L. Cai, H. Pitsch, Optimized chemical mechanism for combustion of gasoline surrogate fuels, Combustion and Flame 162 (2015) 1623–1637.

[92] A. Zolin, A. Jensen, K. Dam-Johansen, Coupling thermal deactivation with oxidation for predicting the combustion of a solid fuel, Combustion and Flame 125 (2001) 1341–1360.

[93] D.J. Maloney, E.R. Monazam, K.H. Casleton, C.R. Shaddix, Evaluation of char combustion models: Measurement and analysis of variability in char particle size and density, Proceedings of the Combustion Institute 30 II (2005) 2197–2204.

[94] X. Zhang, E. Bar-Ziv, A Novel Approach to Determine Thermal Conductivity of Micron-Sized Fuel Particles, Combustion Science and Technology 130 (1997) 79–95.

[95] D. Bradley, G. Dixon-Lewis, S.E.din Habik, E. Mushi, The oxidation of graphite powder in flame reaction zones, Twenty-Sixth Symposium (International) on Combustion 20 (1985) 931–940.

[96] R.F. Johnson, H.K. Chelliah, Numerical simulation of two-dimensional flow over a heated carbon surface with coupled heterogeneous and homogeneous reactions, Combustion Theory and Modelling 7830 (2016) 1–21.

[97] D.J. Tritton, Experiments on the flow past a circular cylinder at low Reynolds numbers, Journal of Fluid Mechanics 6 (1959) 547–567.

[98] O. Desjardins, G. Blanquart, G. Balarac, H. Pitsch, High order conservative finite difference scheme for variable density low Mach number turbulent flows, Journal of Computational Physics 227 (2008) 7125 – 7159.

[99] G. Strang, On the Construction and Comparison of Difference Schemes, SIAM Journal on Numerical Analysis 5 (1968) 506–517.

[100] P.N. Brown, G.D. Bryne, A.C. Hindmarsh, VODE, A Variable Coefficient ODE Solver, SIAM J. Sci. Stat. Comput. 10 (1989) 1038–1051.

[101] X.D. Liu, S. Osher, T. Chan, Weighted Essentially Non-oscillatory Schemes, Journal of Computational Physics 115 (1994) 200–212.

[102] R.D. Falgout, U.M. Yang, Hypre: a library of high performance preconditioners, 2002.

[103] R. Knappstein, G. Kuenne, A. Ketelheun, J. Köser, L. Becker, S. Heuer, M. Schiemann, V. Scherer, A. Dreizler, A. Sadiki, et al., Devolatilization and volatiles reaction of individual coal particles in the context of FGM tabulated chemistry, Combustion and Flame 169 (2016) 72–84.

[104] J. Hees, D. Zabrodiec, A. Massmeyer, S. Pielsticker, B. Gövert, M. Habermehl, et al., Detailed analyzes of pulverized coal swirl flames in oxy-fuel atmospheres, Combustion and Flame 172 (2016) 289–301.

[105] B. Franchetti, F. Cavallo Marincola, S. Navarro-Martinez, A. Kempf, Large Eddy Simulation of a 100kWth swirling oxy-coal furnace, Fuel 181 (2016) 491–502.

[106] R.E. Mitchell, L. Ma, B. Kim, On the burning behavior of pulverized coal chars, Combustion and Flame 151 (2007) 426–436.

[107] N. Vorobiev, M. Schiemann, S. Wirtz, V. Scherer, Pyrometrische Bestimmung von Koksabbrandkinetiken unter Oxyfuel-Bedingungen, 27th Deutscher Flammentag (2015).

[108] T. Sayadi, S. Farazi, S. Kang, H. Pitsch, Transient multiple particle simulations of char particle combustion, Fuel 199 (2017) 289 – 298.

[109] M. Renksizbulut, M.C. Yuen, Numerical Study of Droplet Evaporation in a High-Temperature Stream, Journal of Heat Transfer 105 (1983) 389–397.

[110] A. Attili, F. Bisetti, M.E. Mueller, H. Pitsch, Effects of non-unity Lewis number of gas-phase species in turbulent nonpremixed sooting flames, Combustion and Flame 166 (2016) 192–202.

[111] W.A. Sirignano, Fluid Dynamics and Transport of Droplets and Sprays, volume 1, second edition, 2010.

[112] T. Poinsot, D. Veynante, Theoretical and numerical combustion, 2005.

[113] A. Tomboulides, J. Lee, S. Orszag, Numerical simulation of low Mach number reactive flows, Journal of Scientific Computing 12 (1997) 139–167.

[114] G.P. Smith et al., GRI 3.0, available at http://www.gaseq.co.uk/, accessed May 2017.

[115] R.S. Miller, J. Bellan, Direct numerical simulation of a confined three-dimensional gas mixing layer with one evaporating hydrocarbon-droplet-laden stream, Journal of Fluid Mechanics 384 (1999) 293–338.

[116] K.A. Cliffe, D.A. Lever, Isothermal flow past a blowing sphere, International Journal for Numerical Methods in Fluids 5 (1985) 709–725.

[117] W.E. Ranz, W. Marshall, Evaporation from Drops: I, Chemical Engineering Progress 48 (1952) 141–146.

[118] W.E. Ranz, W. Marshall, Evaporation from Drops: II, Chemical Engineering Progress 48 (1952) 173–180.

[119] CPD user's manual, available at https://www.et.byu.edu/tom/cpd/.

[120] A.R. Fletcher, Thomas H. and Kerstein, D.M. Pugmire, Ronald J. and Grant, A Chemical Percolation Model for Devolatilization: Summary, Journal of Chemical Information and Modeling 53 (2013) 1689–1699.

[121] R.S. Jupudi, V. Zamansky, T.H. Fletcher, Prediction of light gas composition in coal devolatilization, Energy and Fuels 23 (2009) 3063–3067.

[122] D. Genetti, T.H. Fletcher, R.J. Pugmire, Development and Application of a Correlation of 13C NMR Chemical Structural Analyses of Coal Based on Elemental Composition and Volatile Matter Content, Energy & Fuels 13 (1999) 60–68.

[123] D.B. Genetti, An advanced model of coal devolatilization based on chemical structure (1999).

[124] S.V. Apte, K. Mahesh, T. Lundgren, Accounting for finite-size effects in simulations of disperse particle-laden flows, International Journal of Multiphase Flow 34 (2008) 260–271.

[125] A.C. Hindmarsh, P.N. Brown, K.E. Grant, S.L. Lee, R. Serban, D.E. Shumaker, C.S. Woodward, SUNDIALS: Suite of Nonlinear and Differential/Algebraic Equation Solvers, ACM Trans. Math. Softw. 31 (2005) 363–396.

[126] J. Kim, P. Moin, Application of a fractional-step method to incompressible Navier-Stokes equations, Journal of Computational Physics 59 (1985) 308–323.

[127] R. Knappstein, G. Kuenne, L.G. Becker, F.di Mare, A. Sadiki, A. Dreizler, J. Janicka, Large Eddy Simulation of a Novel Gas-Assisted Coal Combustion Chamber, Flow, Turbulence and Combustion (2018).